WHOI-89-28

Woods Hole Oceanographic Institution
Massachusetts Institute of Technology

Joint Program
in Oceanography
and
Oceanographic Engineering

DOCTORAL DISSERTATION

Acoustic Diffraction from a Semi-Infinite Elastic Plate Under Arbitrary Fluid Loading with Application to Scattering from Arctic Ice Leads

by

Peter Hans Dahl

August 1989

WHOI-89-28

Acoustic Diffraction from a Semi-Infinite Elastic Plate under Arbitrary Fluid Loading with Application to Scattering from Arctic Ice Leads

by

Peter Hans Dahl

Woods Hole Oceanographic Institution
Woods Hole, Massachusetts 02543

and

The Massachusetts Institute of Technology
Cambridge, Massachusetts 02139

August 1989

Doctoral Dissertation

Funding was provided by the Office of Naval Research
under contract Number N00014-87-K-0017.

Reproduction in whole or in part is permitted for any purpose of the
United States Government. This thesis should be cited as:
Peter Hans Dahl, 1989. Acoustic Diffraction from a Semi-Infinite Elastic Plate
under Arbitrary Fluid Loading with Application to Scattering from Arctic Ice Leads.
Ph.D. Thesis. MIT/WHOI, WHOI-89-28.

Approved for publication; distribution unlimited.

Approved for Distribution:

Albert J Williams 3rd

Albert J. Williams 3rd, Chairman
Department of Applied Ocean Physics and Engineering

Craig E. Dorman
Acting Dean of Graduate Studies

ACOUSTIC DIFFRACTION FROM A SEMI-INFINITE ELASTIC PLATE UNDER ARBITRARY FLUID LOADING WITH APPLICATION TO SCATTERING FROM ARCTIC ICE LEADS

by
Peter Hans Dahl
B. S. University of Washington, 1976
M. S. University of Washington, 1982

SUBMITTED IN PARTIAL FULFILLMENT OF
THE REQUIREMENTS FOR THE DEGREE OF

DOCTOR OF PHILOSOPHY

at the
MASSACHUSETTS INSTITUTE OF TECHNOLOGY
and the
WOODS HOLE OCEANOGRAPHIC INSTITUTION
May 1989

Signature of Author Peter H Dahl

Department of Ocean Engineering, MIT
MIT/WHOI Joint Program in Oceanographic Engineering
May 15, 1989

Certified by George V. Frisk

George V. Frisk
Thesis Supervisor

Accepted by W K Melville

W. Kendall Melville
Chairman, Joint Committee for Oceanographic Engineering,
Massachusetts Institute of Technology-Woods Hole Oceanographic Institution

Acoustic Diffraction
from a
Semi-Infinite Elastic Plate Under Arbitrary Fluid Loading With Application to Scattering from Arctic Ice Leads

by

Peter Hans Dahl

Submitted in partial fulfillment of the requirements for the degree of Doctor of Philosophy
at the
Massachusetts Institute of Technology
and the
Woods Hole Oceanographic Institution

Abstract

The problem of a low-frequency acoustic plane wave incident upon a free surface coupled to a semi-infinite elastic plate surface, is solved using an analytic approach based on the Wiener-Hopf method. By low-frequency it is meant that the elastic properties of the plate are adequately described by the thin plate equation $(kH \lesssim 1)$. The diffraction problem relates to issues in long range sound propagation through partially ice-covered Arctic waters, where open leads or polynya on the surface represent features from which acoustic energy can be diffracted or scattered. This work focusses on ice as the material for the elastic plate surface, and, though the solution methods presented here have applicability to general edge diffraction problems, the results and conclusions are directed toward the ice lead diffraction process.

The work begins with the derivation of an exact solution to a canonical problem: a plane wave incident upon a free surface (Dirichlet boundary condition) coupled to a perfectly rigid surface (Neumann boundary condition). Important features of the general edge diffraction problem are included here, with the solution serving as a guideline to the more complicated solutions presented later involving material properties of the boundary. The ice material properties are first addressed using the locally reacting approximation for the input impedance of an ice plate, wherein the effects of elasticity are ignored. This is followed by use of the thin plate equation to describe the input impedance, which incorporates elements of elastic wave propagation.

An important issue in working with the thin plate equation is the fluid loading pertaining to sea ice and low-frequency acoustics, which cannot be characterized by simplifying heavy or light fluid loading limits. An approximation to the exact kernel of the Wiener-Hopf functional equation is used here, which is valid in this mid-range fluid loading regime. Use of this approximate kernel allows one to proceed to a complete and readily interpretable solution for the far field diffracted pressure, which includes a subsonic flexural wave in the ice plate. By using Green's theorem, in conjunction with the behavior of the diffracted field along the two-part planar boundary, the functional dependence of Π_D (total diffracted power) in terms of k (wavenumber), H (ice thickness), α (grazing angle) and the combined elastic properties of the ice sheet and ambient medium, is determined.

A means to convert Π_D into an estimate of dB loss per bounce is developed using ray theoretical methods, in order to demonstrate a mechanism for acoustic propagation loss attributed directly to ice lead diffraction effects. Data from the 1984 MIZEX (Marginal Ice Zone Experiments) narrow-band acoustic transmission experiments are presented and discussed in this context.

Thesis Supervisor:	George V. Frisk
Title:	Assoc. Scientist, Woods Hole Oceanographic Institution

undrer mig paa
hvad jeg faar at se
over de høie fjelde

Acknowledgements

I offer my sincere thanks to my thesis supervisor, George Frisk, whose key advice as well as encouragement, were intrumental in keeping me on course. To my thesis committee members Uno Ingard, Henrik Schmidt and Ralph Stephen, I extend my gratitude for their many insightful suggestions which helped shape this dissertation. I also thank Tim Stanton for serving as the chairman of my thesis defense and for the helpful suggestions during the course of this work.

I thank Art Baggeroer and Ira Dyer for the many useful discussions over the years, and greatly appreciate their permission to use data from the MIZEX84 experiments and the "Arctic" computer system. I also thank Peter Mikhalevsky for use of MIZEX84 data and for advice in the early stages of this work.

I have been enriched through endless discussions with my office mates at MIT, and would like to express my appreciation to Chi-Fang Chen, Dan DiPerna, Rob Fricke, Ram Gopalkrishnan, Kevin LePage, and Jea Soo Kim, for the many lively conversations covering almost any topic. I extend special note of thanks to Mike Bruno, Andrew Langley, Nick Makris, John Polcari and D.J. Tang, all who helped me navigate through some occasionally rough seas encountered in this work.

I wish to thank Mary Athanis and Marilyn Staruch, for their administrative assistance *and* sense of humor. I also thank Arthur Newhall and Eddie Scheer for their technical assistance, and the help of other members of the MIT and WHOI Departments of Ocean Engineering is greatly appreciated.

It has been privilege to participate in the MIT/WHOI Joint Program, and I very much appreciate the efforts by members of the WHOI Education Office. I also gratefully acknowledge financial support provided by the WHOI Education Office and the Office of Naval Research.

Contents

List of Figures

List of Tables

Chapter 1

Introduction

In the study of range dependent problems in ocean acoustics, one often works with solution techniques which assume slowly-varying changes in the acoustic boundaries or the ambient medium, such as the parabolic equation method [39] or methods based on the adiabatic approximation [33]. Many problems exist for which acoustic environmental changes can occur abruptly, as in geological features on the ocean floor, or an open lead in the Arctic ice canopy. Here the diffraction process is a primary result of the range dependent feature, and solutions dependent upon these features being slowly-varying usually fall short in describing diffractive effects. For these problems a more numerically intensive approach is often used, for example, a finite difference solution for the discretized wave equation in heterogeneous media, which can model various seafloor diffractors in two-dimensional geometry [24].

This thesis studies in detail, and presents an analytical solution to the problem of an acoustic plane wave interacting with a free surface coupled to a semi-infinite elastic surface. The essential physics of the acoustic diffraction process such as mode coupling and edge diffractive effects due to the abrupt boundary change, are included in the solution. The problem relates directly to long range sound propagation in Arctic waters, where there is a mixture of open water and ice as in the marginal ice zone. Here, the upward refracting sound channel causes repeated interaction with the discontinuous ice canopy surface, and open leads or polynyas on this surface represent features from which acoustic energy can be diffracted or scattered [52] and thereby lost from the acoustic channel. We therefore focus on ice as the material for the elastic surface or plate, and, though our methods have

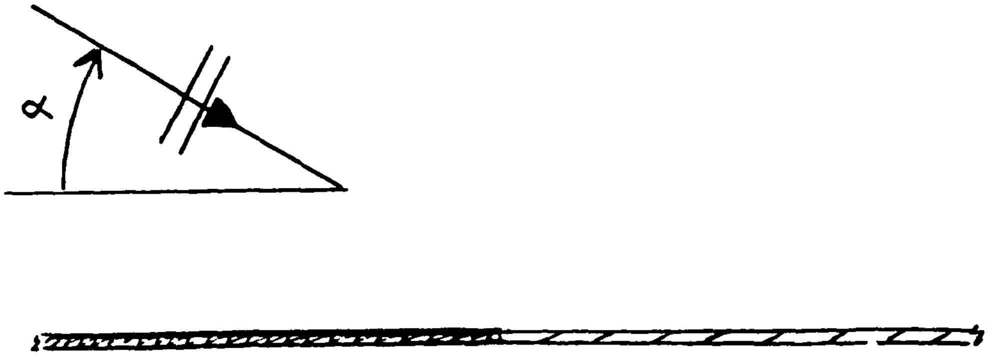

Figure 1.1: Diffraction from two semi-infinite half-planes each characterized by a different boundary condition; the incident field is a plane wave with grazing angle α.

applicability to general edge diffraction problems, our results and conclusions are directed towards the ice lead diffraction process.

The semi-infinite plate model for the ice lead diffraction process belongs to a class of two-dimensional diffraction problems known as half-plane problems. Probably the most well-known solution in this class is Sommerfeld's solution of the scattering of a plane wave from an infinitely hard half-plane [58], or the "knife edge" problem. Closely related to problems associated with a single semi-infinite half-plane are those involving two coupled half-planes (Fig. 1.1), where different boundary conditions are prescribed on each semi-infinite half-plane. Diffraction problems of this type can be shown, by using a Green's theorem approach, to reduce to a particular boundary integral equation amenable to analytic or closed form solutions using the Wiener-Hopf method [59]. In this thesis we employ the Wiener-Hopf method to examine the ice lead diffraction process. A key attribute of such an approach is that it is not fundamentally numerical in nature and allows additional insight into the mathematical and physical structure of the acoustic field due to range discontinuities.

Single and coupled half-plane diffraction problems have been extensively studied in electromagnetics and acoustics using techniques based on the Wiener-Hopf method. Senior

(1952)[64] presents the solution of the diffracted field due to a electromagnetic plane wave field incident upon a semi-infinite metallic sheet. Heins and Feshbach (1947) [35] present a solution of an acoustic plane wave incident upon two coupled half-planes where each surface is characterized by a different complex admittance parameter. Bazar and Karp (1957) [5] have examined a similar two-part problem involving electromagnetic wave propagation over land and sea, known as the "land/sea" problem. Lamb (1958) [46] studied the problem of plane wave diffraction from a semi-infinite elastic plate under conditions of light fluid loading. More recently Cannell (1975,1976) [12,11] and Crighton and Innes (1983) [21] have examined similar plane wave scattering problems for both the heavy and light fluid loading limits.

1.1 Overview of Thesis

We begin in Chapter 2 with the solution of a canonical problem: a plane wave incident upon a surface where the boundary condition changes from Dirichlet (free surface) to Neumann (perfectly rigid surface). The boundary conditions addressed in this problem are highly idealized with respect to the ice lead diffraction process. Nevertheless, important features of the general diffraction process are produced here, with this solution forming the baseline structure for the solution of more complicated problems to follow. Since the solution is expressed in terms of the Fourier transform of the diffracted field, it will also lay out in a straight forward way a pathway for inversion which is utilized in the rest of the thesis.

Chapter 3 begins with a discussion of the input impedance of ice, in the context of locally and non-locally reacting surfaces. Next the solution of a plane wave incident upon a finite impedance, locally reacting surface is presented following the pathway developed in Chapter 2. An advantage of our method over those previously mentioned involving Wiener-Hopf methods, is that we have approximated a step in the Wiener-Hopf solution procedure known as the kernel decomposition. In all but the simplest Wiener-Hopf type equations the exact decomposition, available in principle, leads to a degree of complexity in the solution that hinders practical implementation of the results. The approximate kernel and decompostion used here is very accurate and allows us to proceed to interpretable results. Finally, a power balance for a plane wave incident upon a free surface joined to a locally reacting surface is demonstrated.

In Chapter 4 we solve the problem of a plane wave incident upon a semi-infinite elastic plate capable of supporting a subsonic flexural wave. A key issue here is the fluid loading pertaining to the elastic sea ice and low frequency acoustics, which cannot be characterized by the simplifying heavy or light fluid loading limits. A new approximate kernel decomposition introduced here allows us to complete the solution in this neither light nor heavy fluid loading regime.

In Chapter 5 we shall demonstrate one of several potential means to implement results from our solution in the analysis of acoustic propagation data. Data from the 1984 MIZEX (Marginal Ice Zone Experiments) narrow-band acoustic transmission experiments (25-200 Hz) are presented here. These data, which are a result of acoustic propagation via a partially ice-covered path, are compared to estimates of transmission loss based on ray theoretical methods which include an additional loss due to diffraction effects from a surface with open leads.

Chapter 2

Canonical diffraction problem

This chapter presents the exact solution of a canonical two-dimensional diffraction problem: a monochromatic acoustic plane wave incident upon a surface where the boundary condition changes from Dirichlet (free surface) to Neumann (perfectly rigid surface). The problem, though highly idealized, nevertheless shares some similarities to the free surface to ice canopy surface boundary change. Furthermore, it allows us to lay out, without unnecessary complications the notation and problem geometry used in this thesis and important details and results of the Wiener-Hopf procedure from which later results in this thesis will be based upon.

2.1 Solution of canonical diffraction problem

Consider a plane wave with grazing angle α incident upon a planar surface (Fig. 2.1) with the following mixed boundary conditions

$$\phi_T(x,0) = 0 \quad x < 0 \tag{2.1}$$

and

$$\frac{\partial \phi_T}{\partial y}(x,0) = 0 \quad x > 0, \tag{2.2}$$

where ϕ_T is the total acoustic velocity potential, and ϕ_I is the incident potential with an assumed harmonic time dependence $e^{-i\omega t}$.

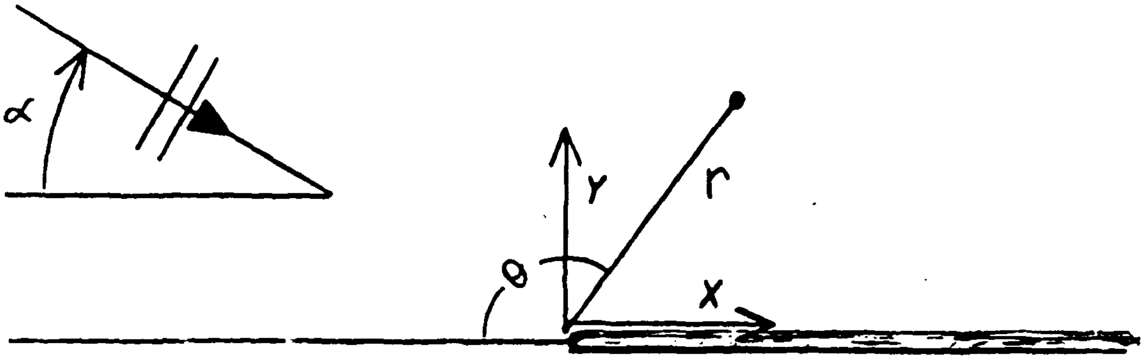

Figure 2.1: Canoncial diffraction problem and field coordinate system used in this thesis. Note that the ambient medium is above the planar boundary with vacuum below. The field is assumed to be independent of the z-coordinate which points out of the page. The incident field is a plane wave with grazing angle α.

The total potential can be expressed as the coherent sum of ϕ_I, the reflected potential ϕ_R, and the diffracted potential ϕ_D

$$\phi_T = \phi_I + \phi_R + \phi_D \tag{2.3}$$

with

$$\phi_I(x,y) = e^{ikx\cos\alpha - iky\sin\alpha} \tag{2.4}$$

and

$$\phi_R(x,y) = e^{ikx\cos\alpha + iky\sin\alpha}. \tag{2.5}$$

The free-space wavenumber is

$$k = \frac{\omega}{c} = k_1 + ik_2 \quad k_1, k_2 > 0 \tag{2.6}$$

with c the sound speed in the ambient acoustic medium which is in general complex with negative imaginary part, and $\omega = 2\pi f$. The small imaginary part in k allows for dissipation in the ambient medium and is useful, but not necessary, to more clearly define the regions of analyticity in the Wiener-Hopf procedure. In this thesis all final results reported will be with $k_2 = 0$. The reflected field is the one corresponding to an perfectly rigid or 'hard' surface but which we apply to the entire boundary. Whether we set up the problem with a free surface reflected field or hard surface reflected field makes no difference, since the final result compensates for this. In this problem the reflection coefficient moduli for each half of the boundary are unity but the phases differ by π, resulting in a discontinuity in the coherent sum of ϕ_I and ϕ_R, located along the line dividing specular reflection from the two different surfaces. This line is a radial line extending from $\theta = \pi - \alpha$ (Fig.(2.1)); to the left of this line the reflected field originates from the free surface boundary, and to the right the reflected field originates from the hard surface boundary. Thus a diffracted field is generated in order to restore continuity of the field and maintain the mixed boundary conditions.

If we incorporate the hard boundary reflected field, which together with ϕ_I satisfies only part of a two-part boundary value problem, the properties of ϕ_D on the boundary must therefore necessarily be

$$\phi_D(x,0) = -2e^{ikx\cos\alpha} \qquad x < 0 \tag{2.7}$$

and

$$\frac{\partial\phi_D(x,0)}{\partial y} = 0 \qquad x > 0 \tag{2.8}$$

in order to maintain the boundary conditions.

We assume ϕ_D takes the following form which satisfies the homogeneous Helmholtz equation

$$\phi_D(x,y) = \int_{-\infty}^{\infty} G(q)e^{iqx}e^{-y\sqrt{q^2-k^2}}\frac{dq}{2\pi} \tag{2.9}$$

where $G(q)$ is an unknown spectral function and is the Fourier transform of ϕ_D(x,0). The variable q is the complex horizontal wavenumber, where the horizontal spatial coordinate x and q are conjugate Fourier transform variables.

Note the difference between the scattering from a periodic surface [71] and this case. For the periodic surface the scattered field consists of discrete angles, or scattering orders, which are both real and complex. The increment between each angle is inversely proportional to the spatial period of the surface. For the two coupled half-planes, the spatial period is infinite and the discrete angles have formed a continuum as expressed by $G(q)$. Each

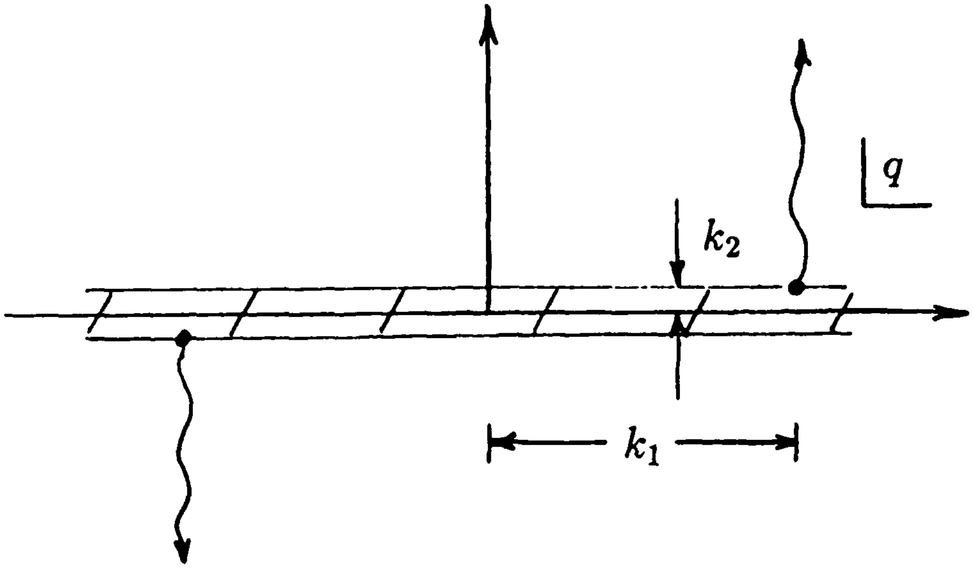

Figure 2.2: The branch cuts for the square root of $q^2 - k^2$ defining strip between $\pm k_2$ in the complex q plane.

scattering order in the periodic case is weighted by a plane wave reflection coefficient; here $G(q)$ serves as the weighting function for a continuous distribution of plane waves.

In order for the integral in Eq.(2.9) to be convergent we specify the branch cuts of $\sqrt{q^2 - k^2}$ such that

$$Real(\sqrt{q^2 - k^2}) > 0. \tag{2.10}$$

This will occur for any inversion contour within the strip between $\pm k_2$ in Fig. 2.2. In the case $k_2 \rightarrow 0$ the inversion contour approaches the real-q axis and the inversion contour is indented around any poles or branch points which lie on the real axis.

The Fourier transform definitions used in this thesis will be such that,

$$G(q) = \int_{-\infty}^{0} \phi_D(x,0)e^{-iqx}dx + \int_{0}^{\infty} \phi_D(x,0)e^{-iqx}dx = G_+(q) + G_-(q). \tag{2.11}$$

The + or − subscripts in Eq.(2.11) denote the region of analyticity, either the upper or lower mathematical half-planes, of a function in the complex q plane. For example, $G_+(q)$ can exist only for $Im(q) > 0$; otherwise the exponential term in the Fourier transform is unbounded at $x = -\infty$. We can also write formally that

$$G(q) = \int_{-\infty}^{\infty} \phi_D(x,0)e^{-iqx}dx \tag{2.12}$$

and

$$-\sqrt{q^2 - k^2}G(q) = \int_{-\infty}^{\infty} \frac{\partial \phi_D(x,0)}{\partial y} e^{-iqx} dx. \tag{2.13}$$

Thus, applying the semi-infinite transform definition to what is known about ϕ_D(x,0) [Eq.(2.7)] gives,

$$-2\int_{-\infty}^{0} e^{ikx\cos\alpha - iqx} dx + G_-(q) = \frac{-2i}{(q - k\cos\alpha)} + G_-(q). \tag{2.14}$$

The first term in Eq.(2.14) is by definition a '+' function. That is, its existence requires $Im(q) > k_2 \cos\alpha$, and thus the region of analyticity is delineated by a line parallel to the real-q axis but passing just above the pole at $q = k\cos\alpha$. Similarly, applying what is known about $\frac{\partial \phi_D(x,0)}{\partial y}$ [Eq.(2.8)] leads to,

$$-\sqrt{q^2 - k^2}G(q) = L_+(q) + \int_{0}^{\infty} \frac{\partial \phi_D(x,0)}{\partial y} e^{-iqx} dx = L_+(q). \tag{2.15}$$

The functions $G_-(q)$ and $L_+(q)$ are unknown, with the latter representing the semi-infinite ($x < 0$) transform of the normal derivative of $\phi_D(x,0)$. Eliminating $G(q)$ from Eqs. (2.14) and (2.15) gives

$$-L_+(q) = \frac{2i}{(q - k\cos\alpha)}\sqrt{q^2 - k^2} + G_-(q)\sqrt{q^2 - k^2}. \tag{2.16}$$

The above is the Wiener-Hopf functional equation where

$$K(q) = \sqrt{q^2 - k^2} \tag{2.17}$$

is the kernel of the equation. The Wiener-Hopf functional equation can be reached by several different pathways. For example, a Green's function approach together with the convolution theorem [59], would have required the Fourier transform of the Hankel function along the boundary which is the same form as our kernel. We have used Jones's Method [42] to arrive at this equation which works directly from the Fourier transform of the boundary conditions that govern the problem.

The essence of the Wiener-Hopf procedure is to factorize or decompose this kernel into two factors, one analytic in an upper half-plane and the other analytic in a lower half-plane of the complex q plane. A successful decomposition will, as we shall see, allow us to recover $G(q)$ and thus the Fourier transform of $\phi_D(x,y)$. In this case the decomposition is immediate: because the branch line for $\sqrt{q-k}$ extends from the point $q = k_1 + ik_2$ into an upper half of the q plane, this function is only free of singularities, or analytic, in some lower half of the q plane. The region of analyticity is thus defined as $Im(q) < k_2$ and is delineated by a line running parallel to the real-q axis but passing just below $Im(q) = k_2$. Thus $\sqrt{q-k}$ is a '−' function and in a similar manner $\sqrt{q+k}$ a '+' function and analytic for $Im(q) > k_2$ Upon decomposing the kernel we have

$$\frac{L_+(q)}{\sqrt{q+k}} + \sqrt{q-k}G_-(q) = \frac{-2i}{(q - k\cos\alpha)}\sqrt{q-k}. \tag{2.18}$$

The term on the right side of Eq.(2.18) is neither a '+' nor '−' function, so it is split into two terms

$$R(q) = R_-(q) + R_+(q) \tag{2.19}$$

where

$$R_-(q) = \frac{-2i}{(q - k\cos\alpha)}[\sqrt{q-k} - \sqrt{k\cos\alpha - k}] \tag{2.20}$$

and

$$R_+(q) = \frac{-2i\sqrt{k\cos\alpha - k}}{(q - k\cos\alpha)}. \tag{2.21}$$

This is known as additive decompostion [14]. In $R_-(q)$ the effect of the pole at $q = k\cos\alpha$ is cancelled and $R_-(q)$ remains analytic in a lower half-plane as defined by $Im(q) < k_2$; $R_+(q)$ is analytic in an upper half-plane as defined by $Im(q) > k_2\cos\alpha$.

The functions $L_+(q)$ and $G_-(q)$ are unknown but their regions of analyticity can be inferred. For example, consider

$$\phi_D(x,0) \sim e^{i(k_1+ik_2x)} \quad x \to \infty. \tag{2.22}$$

Then, in order for the semi-infinite Fourier transform to exist, $G_-(q)$ can be analytic *only* for $Im(q) < k_2$, this fact being independent of any algebraic dependence of $\phi_D(x,0)$. In a similar manner $L_+(q)$ can be analytic only for $Im(q) > -k_2$. When k_2 shrinks to zero these domains of analyticity occur just below and just above the real-q axis. Upon using the additive decompostion we have

$$\frac{L_+(q)}{\sqrt{q+k}} - R_+(q) = R_-(q) - \sqrt{q-k}\ \ G_-(q) = E(q). \tag{2.23}$$

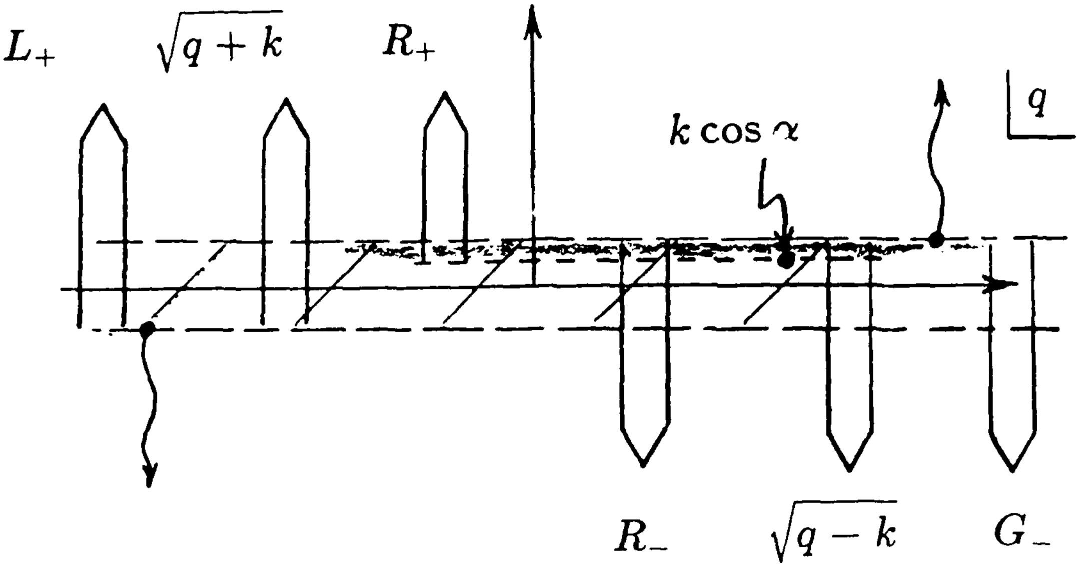

Figure 2.3: The common region of analyticity (shaded) in the complex q plane. Arrows with open ends mean that a half-plane is delineated here but the analytic region does not include the actual line.

In Eq.(2.23) everything on the left side is analytic in an upper half-plane while everything on the right side is analytic in a lower half-plane of the q plane. A common region of analyticity exists, i.e., the strip in Fig. 2.3, and by analytic continuation $E(q)$ must be analytic in the entire finite complex q plane; thus, $E(q)$ is an entire function. Determining the nature of $E(q)$ as $|q| \to \infty$ allows us to recover the unknowns in Eq.(2.23).

2.1.1 Edge conditions, Liouville's theorem and recovery of $G(q)$

The nature of $E(q)$ as $|q| \to \infty$ is determined by the behavior of the quantities in Eq.(2.23) as $|q| \to \infty$. Since L_+ and G_- are unknowns, their behavior is ascertained through the behavior of the equivalent transform as $x \to 0$. This is a property of Fourier and Laplace transforms in which global properties in one domain are mapped to local properties in the other domain.

The local properties we require are known as edge conditions. The edge conditions invoke the appropriate physical constraints on the diffracted field near the edge of the boundary discontinuity e.g., the diffracted field can not act as a source and radiate energy on its own account [41]. Thus, for example, let $\phi_D(x,0) \sim x^{\nu}$, $\nu \geq 0$ as $x \to 0^+$ [59], which is a very general requirement of ϕ_D. The corresponding transform behavior of $G_-(q)$ as $|q| \to \infty$, using a result from Abelian asympotics [61] is

$$G_-(q) \sim \int_0^{\infty} x^{\nu} e^{iqx} dx \sim |q|^{-\nu-1}. \tag{2.24}$$

Also, the velocity can have no more than an integrable singularity at the origin [19], which in this case calls for $\frac{\partial \phi_D}{\partial y} \sim x^{\frac{-1}{2}}$ as $x \to 0^+$, and from Abelian asymptotics this gives $L_+(q) \sim |q|^{\frac{-1}{2}}$ as $|q| \to \infty$.

The nature of $E(q)$ as $|q| \to \infty$ is now determined by application of Liouville's theorem. Let $F_-(q)$ and $F_+(q)$ represent the combinations of '$-$' and '$+$' functions in Eq.(2.23). Liouville's theorem states that if

$$|F_-(q)| < |q|^r, \quad q \to \infty \tag{2.25}$$

and

$$|F_+(q)| < |q|^s, \quad q \to \infty \tag{2.26}$$

where it is assumed $q \to \infty$ in the appropriate half-plane, then $E(q)$ is a polynomial of degree less than or equal to the integer part of $\min(r,s)$. If either r or s is negative, then $E(q)$ must vanish at infinity and $E(q)$ is identically zero. Liouville's theorem has many stated versions, the one used here is the most explicit and is a paraphrase of Noble [59].

Having determined the behavior to L_+ and G_- as $|q| \to \infty$, one sees that both sides of Eq.(2.23) vanish as $q \to \infty$, for example, the '$-$' side behaves at most as $\sim |q|^{\frac{-1}{2}}$ as $|q| \to \infty$. This means the entire function $E(q)$ vanishes at infinity and is therefore identically zero, giving the result

$$G_-(q) = \frac{R_-(q)}{\sqrt{q-k}} \qquad L_+(q) = \frac{R_+(q)}{\sqrt{q+k}}. \tag{2.27}$$

Finally, using Eq. (2.14) we have

$$G(q) = \frac{-2i}{\sqrt{q-k}(q - k\cos\alpha)} \sqrt{k\cos\alpha - k}. \tag{2.28}$$

Note that constants like $\sqrt{k\cos\alpha - k}$ in the above will often appear in this thesis, which are evaluated as $-i\sqrt{k - k\cos\alpha}$ to conform with our branch cut structure.

An exact solution of $\phi_D(x,y)$ in terms of its Fourier transform integral is now available. This integral, in the form of Eq.(2.9), consists of a continuous plane wave spectrum. The diffracted field thus contains all the spatial Fourier components necessary to accommodate the step function-like discontinuity at the boundary.

2.2 Inversion of the diffracted field plane wave spectrum

Inversion to $\phi_D(x,y)$ is readily carried out using the following transformations:

$$x = -r\cos\theta \qquad y = r\sin\theta \qquad q = -k\cos\beta \tag{2.29}$$

where r and θ are polar coordinates, giving

$$\phi_D(r,\theta) = i\frac{\sqrt{1-\cos\alpha}}{\sqrt{2}\pi}\int_\Gamma P(\beta)e^{ikr\cos(\beta-\theta)}d\beta \tag{2.30}$$

with

$$P(\beta) = \frac{\sin\beta}{(\cos\alpha + \cos\beta)\cos\frac{\beta}{2}}. \tag{2.31}$$

The transformation $q = -k\cos\beta$ is multivalued and we will use the strip in the complex-β plane defined by $0 < Real(\beta) < \pi$, with the new integration contour Γ defined in Fig 2.4. The transformed plane wave spectrum, $P(\beta)$, will be called the angular spectrum [16] to distinguish it from the former.

Equation (2.30) is evaluated asymptotically by method of steepest descents [17] with the saddle point at $\beta = \theta$. The asymptotic analysis requires deformation of the Γ contour into the steepest descent path (SDP) contour $\Gamma(\theta)$. Any singularities which are crossed while deforming the contour, such as the pole in the angular spectrum at $\beta = \pi - \alpha$, must be accounted for in the evaluation. The residue of the pole at $\beta = \pi - \alpha$ comprises a necessary geometric field, but in the vicinity of this pole the asymptotic method breaks down because the SDP contour crosses the real-β axis near $\beta = \pi - \alpha$ and the integrand is no longer slowly varying. One way to get around this problem is to partition the angular spectrum [16],

$$P(\beta) = P_1(\beta) + P_2(\beta) \tag{2.32}$$

such that $P_1(\beta)$ is analytic for $0 < Real(\beta) < \pi$ and $P_2(\beta)$ retains the pole at $\beta = \pi - \alpha$.

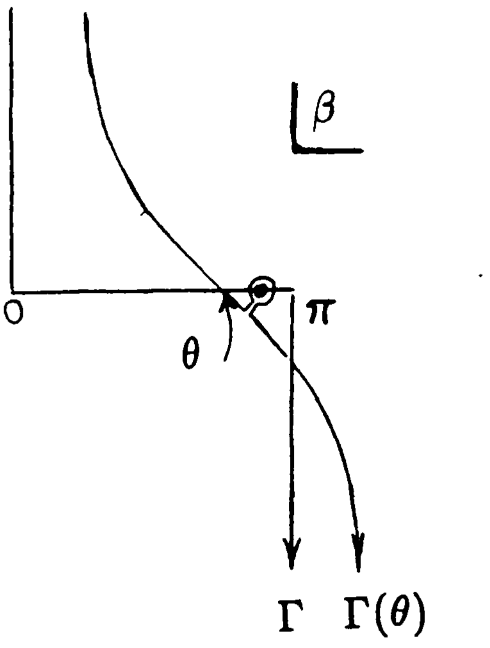

Figure 2.4: Inversion contour is Γ, and deformed SDP contour $\Gamma(\theta)$. The pole at $\beta = \pi - \alpha$ is captured for $\theta < \pi - \alpha$

The diffracted potential now takes the form

$$\phi_D = i\frac{\sqrt{1-\cos\alpha}}{\sqrt{2}\pi}\int_\Gamma (P_1 + P_2)e^{ikr\cos(\beta-\theta)}d\beta = \phi_{D1} + \phi_{D2} \tag{2.33}$$

where

$$P_1(\beta) = \frac{\sin\beta\sin\frac{\alpha}{2} - \cos\frac{\beta}{2}\cos\frac{\beta-\alpha}{2}}{2\cos\frac{\beta}{2}\sin\frac{\alpha}{2}\cos\frac{\beta+\alpha}{2}\cos\frac{\beta-\alpha}{2}} \tag{2.34}$$

and

$$P_2(\beta) = \frac{1}{2\sin\frac{\alpha}{2}\cos\frac{\beta+\alpha}{2}}. \tag{2.35}$$

With the partitioning, Eq.(2.33) can be evaluated asymptotically for the first term ($P_1(\beta)$) using the SDP contour Γ_θ which passes through the saddle point on the real-β axis (Fig. 2.4). The result for $kr \gg 1$ is,

$$\phi_{D1}(r,\theta) = \frac{(1+i)}{\sqrt{2}\pi}\sqrt{1-\cos\alpha}\;\; P_1(\theta)\frac{e^{ikr}}{\sqrt{kr}} + O(\frac{1}{(kr)^{\frac{3}{2}}}). \tag{2.36}$$

This is an asymptotic series with the dominant behavior being a cylindrical waveform emanating from the origin (point of discontinuity) and a far field radiation pattern defined by $P_1(\theta)$.

Many integrals of the type

$$I(r,\theta) \equiv \int_{\Gamma} Q(\beta) e^{ikr\cos(\beta-\theta)} d\beta \tag{2.37}$$

where $Q(\beta)$ is analytic for $0 < Real(\beta) < \pi$, will be used in this thesis. An asymptotic evaluation of such integrals valid for $kr \gg 1$ is

$$I(r,\theta) = (1-i)\sqrt{\pi} Q(\theta) \frac{e^{ikr}}{\sqrt{kr}} + O(\frac{1}{(kr)^{\frac{3}{2}}}). \tag{2.38}$$

This will be called the SDP evaluation, and a derivation of this expression is presented in Appendix A.

The other portion of the diffracted field remains in integral form

$$\phi_{D2}(r,\theta) = i\frac{\sqrt{1-\cos\alpha}}{\sqrt{2}\pi} \int_{\Gamma} \frac{1}{2\sin\frac{\alpha}{2}\cos\frac{\beta+\alpha}{2}} e^{ikr\cos(\beta-\theta)} d\beta. \tag{2.39}$$

We could proceed with a SDP evaluation provided the saddle point is not too close to $\pi - \alpha$, and in the process of deforming the contour we would capture the pole at $\beta = \pi - \alpha$ provided $\theta < \pi - \alpha$ (Fig. 2.5). The pole capture is 'clockwise' or $-2\pi i$ and the resulting geometric field is

$$\phi_{geo}(r,\theta) = -2e^{-ikr\cos(\alpha+\theta)}, \tag{2.40}$$

which, together with the hard surface reflected field, satisfies the Dirichlet boundary condition for $x < 0$. Assuming the residue $\phi_{D2}(r,\theta)$ has been accounted for, the remaining integral is recast into the form known as the Fresnel integral which accounts for the behavior of Eq.(2.39) near the vicinity of the pole. This is done in two steps [4]. Using $\beta' = \beta - \theta$ with Γ' the corresponding contour in the β' plane, we have

$$\phi_{D2}(r,\theta) = \frac{i}{2\pi} \int_{\Gamma'} \frac{e^{ikr\cos\beta'}}{\cos(\frac{\beta'+\theta+\alpha}{2})} d\beta'. \tag{2.41}$$

The Γ' contour is now deformed into a new one that passes through $Real(\beta') = 0$, which results in

$$\phi_{D2}(r,\theta) = \frac{i\cos(\frac{\theta+\alpha}{2})}{\pi} \int_{\Gamma(0)'} \frac{\cos\frac{\beta'}{2}}{\cos\beta' + \cos(\theta+\alpha)} e^{ikr\cos\beta'} d\beta', \tag{2.42}$$

and upon using $\cos\beta' = 1 + i\tau^2$, Eq.(2.41) becomes

$$\phi_{D2}(r,\theta) = \frac{(1-i)}{\sqrt{2}\pi} b e^{ikr} \int_{-\infty}^{\infty} \frac{e^{-kr\tau^2}}{\tau^2 - ib^2} d\tau \tag{2.43}$$

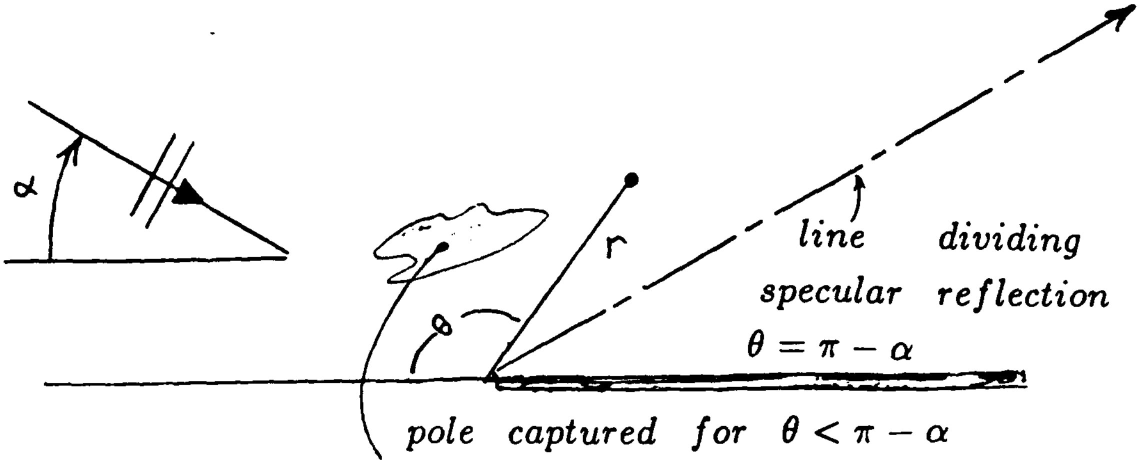

Figure 2.5: The x, y field plane expressed in terms of r, θ. The pole corresponding to a geometric field is captured for $\theta < \pi - \alpha$, for $\theta > \pi - \alpha$ the boundary condition is already satisfied by $\phi_I + \phi_R$ and no pole is captured in this region.

where

$$b = \sqrt{2}\cos(\frac{\theta + \alpha}{2}). \tag{2.44}$$

The integral in Eq. (2.43) is of the Fresnel type which we will evaluate exactly using an IMSL subroutine [1], with the entire expression in Eq.(2.43) henceforth defined as the function $\mathcal{F}(r, \theta; \alpha)$.

2.3 Properties of the Fresnel integral

It will be useful to record here the asymptotic form of $\mathcal{F}(r, \theta; \alpha) = \mathcal{F}_A(r, \theta; \alpha)$ by applying the SDP evaluation formula Eq.(2.38) to Eq.(2.39) which gives,

$$\mathcal{F}_A(r, \theta; \alpha) = \frac{1 + i}{\sqrt{2\pi} b} \frac{e^{ikr}}{\sqrt{kr}} + O(\frac{1}{(kr)^{\frac{3}{2}}}). \tag{2.45}$$

The asymptotic form of $\mathcal{F}(r, \theta; \alpha)$ is not valid in the vicinity of $\theta = \pi - \alpha$, for the same reason the asymptotic analysis failed earlier. Specifically, one way to evaluate the integral in Eq.(2.43) for $kr \gg 1$ is to expand the part of the integrand equal to $(r^2 + ib^2)^{-1}$ into a Taylor series and integrate term by term. The Taylor series has a radius of convergence equal to $O(b)$; when b vanishes near $\theta = \pi - \alpha$ the analysis leading to $\mathcal{F}_A(r, \theta; \alpha)$ is not valid no matter how large kr is. A more complete asymptotic analysis using integration by parts shows that the validity of the asymptotic form of $\mathcal{F}(r, \theta; \alpha)$ depends on the value of kr [38], and with

$$\sqrt{2kr}|\cos(\frac{\theta + \alpha}{2})| \gtrsim 3.55 \tag{2.46}$$

the asymptotic form $\mathcal{F}_A(r, \theta; \alpha)$ is valid.

The area where $\mathcal{F}_A(r, \theta; \alpha)$ is not valid is the transition region between the two geometrically reflected fields. The behavior of the diffracted field here is complex and requires the exact Fresnel integral for a complete description of the field across this region. We can get an idea of the diffracted field behavior within the transition region by examining $\mathcal{F}(r, \theta, \alpha)$ immediately on either side of the line dividing specular reflection. Putting Eq. (2.43) into a form suitable for evaluation by IMSL gives

$$\begin{aligned} \mathcal{F}(r, \theta; \alpha) &= e^{ikr} W(arg) \quad \theta < \pi - \alpha \\ \mathcal{F}(r, \theta; \alpha) &= -e^{ikr} W(arg) \quad \theta > \pi - \alpha \end{aligned} \tag{2.47}$$

In the above, W is the complex error function $(C(z) + iS(z)$ as defined in Abramowitz and Stegun [3], p. 301); this is the function evaluted by IMSL with $arg = e^{i\frac{\pi}{4}}\sqrt{kr}|b|$. In the limit of θ approaching $\pi - \alpha$, then $b \rightarrow 0$ and one can observe that $W \rightarrow 1$, giving

$$\lim_{\delta \rightarrow 0} \mathcal{F}(r, \pi - \alpha \pm \delta) = \mp e^{ikr}. \tag{2.48}$$

Thus, within the transition region the diffracted field approaches the same order of magnitude (i.e., plane wave behavior) as the incident and reflected fields. Having the same magnitude, the diffracted field is able to interfere with the incident and reflected fields and provide a means to smooth the transition between the two different specularly reflected fields. Outside the transition region, or the shadow region, the diffracted field decays with characteristic cylindrical wave dependence as exhibited by the asymptotic form of $\mathcal{F}_A(r, \theta, \alpha)$. We return to the concepts of transition and shadow regions in Chapter 3, in the discussion of conservation of power.

Also recorded here for future use is the radial derivative $\frac{\partial}{\partial r}$ of $\mathcal{F}(r,\theta,\alpha)$. We start by taking the radial derivative of Eq.(2.39) which is

$$\frac{-k}{2\pi}\int_{\Gamma}\frac{\cos(\beta-\theta)}{\cos(\frac{\beta+\theta}{2})}e^{ikr\cos(\beta-\theta)}d\beta.$$

Then, duplicating the steps which lead to the Fresnel integral, we have for this case

$$\frac{\partial\mathcal{F}(r,\theta;\alpha)}{\partial r} = ik\mathcal{F}(r,\theta;\alpha) - k\frac{b}{\pi}e^{i(kr-\frac{\pi}{4})}\int_{-\infty}^{\infty}\tau^2\frac{e^{-kr\tau^2}}{\tau^2-ib^2}d\tau. \tag{2.49}$$

We now focus on the integral in the above equation

$$I = 2\int_{0}^{\infty}\tau^2\frac{e^{-kr\tau^2}}{\tau^2-ib^2}d\tau \tag{2.50}$$

and

$$I_1 = \int_{0}^{\infty}\tau^2\frac{e^{-kr(\tau^2-ib^2)}}{\tau^2-ib^2}d\tau = e^{ikrb^2}\quad I. \tag{2.51}$$

Taking the derivative with respect to kr of I_1 and integrating the result gives

$$\frac{dI_1}{dkr} = -e^{ikrb^2}\frac{\sqrt{\pi}}{(kr)^{\frac{3}{2}}}, \tag{2.52}$$

and thus

$$I_1 = \sqrt{\pi}\int_{kr}^{\infty}\frac{e^{i\Omega b^2}}{\Omega^{\frac{3}{2}}}d\Omega. \tag{2.53}$$

Upon using the substitution $\Omega b^2 = \mu^2$, we have that

$$I_1 = 2\sqrt{\pi}b\int_{\sqrt{kr}b}^{\infty}\frac{e^{i\mu^2}}{\mu^2}d\mu \tag{2.54}$$

or

$$I = 2\sqrt{\pi}be^{-ikrb^2}\int_{\sqrt{kr}b}^{\infty}\frac{e^{i\mu^2}}{\mu^2}d\mu. \tag{2.55}$$

Equation(2.55) is recast using integration by parts with,

$$\int_{\sqrt{kr}b}^{\infty}\frac{e^{i\mu^2}}{\mu^2}d\mu = 2i\int_{\sqrt{kr}b}^{\infty}e^{i\mu^2}d\mu + \frac{e^{ikrb^2}}{\sqrt{kr}b} \tag{2.56}$$

such that

$$I = 4\sqrt{\pi}ibe^{-ikrb^2}\int_{\sqrt{kr}b}^{\infty}e^{i\mu^2}d\mu + \frac{2\sqrt{\pi}}{\sqrt{kr}}. \tag{2.57}$$

An alternative expression for the Fresnel integral, equivalent to Eq.(2.43) is [4]

$$\mathcal{F}(r,\theta;\alpha) = \sqrt{\frac{2}{\pi}}(1-i)e^{ikr(1-b^2)}\int_{\sqrt{kr}b}^{\infty}e^{i\mu^2}d\mu. \tag{2.58}$$

Using this expression, along with Eq.(2.49) and Eq.(2.57) gives us

$$\frac{\partial \mathcal{F}(r,\theta;\alpha)}{\partial r} = ik\mathcal{F}(r,\theta;\alpha)(1-2b^2) - kb\sqrt{\frac{2}{\pi}}(1-i)\frac{e^{ikr}}{\sqrt{kr}}. \tag{2.59}$$

This result shows how the Fresnel integral accounts for the continuous variation of radial particle velocity across the transition region. Far away from the transition region $\mathcal{F}(r,\theta;\alpha) \simeq \mathcal{F}_A(r,\theta;\alpha)$ and therefore

$$\frac{\partial \mathcal{F}(r,\theta;\alpha)}{\partial r} \simeq \frac{ik(1+i)}{\sqrt{2\pi}b}\frac{e^{ikr}}{\sqrt{kr}} \tag{2.60}$$

which is the usual cylindrical wave dependence for radial particle velocity. Well into the transition region b approaches zero and $\mathcal{F}(r,\theta;\alpha)$ approaches the plane wave behavior of Eq.(2.48) and therefore

$$\frac{\partial \mathcal{F}(r,\theta;\alpha)}{\partial r} \simeq \pm ike^{ikr}. \tag{2.61}$$

2.4 The diffracted field and check of the boundary conditions

Contours of equal amplitude level for ϕ_{D1} and ϕ_{D2}, are shown in Figs. 2.6 and 2.7. The incident field is a monochromatic plane wave of 50 Hz and $\alpha = 15^o$, with the dB levels referenced to a unit amplitude incident wave field. The geometric plane wave field arising from a residue contribution from $\phi_D(r,\theta)$ is removed and shown here are only the SDP and Fresnel integral contributions to $\phi_D(r,\theta)$. The same fields are shown in Figs. 2.8 and 2.9 for $\alpha = 135^o$, which is equivalent to the plane wave incident from the other side.

The boundary condition to be satisfied by $\phi_D(x,0)$, minus its residue contribution, is now the same as Eqs.(2.1) and (2.2). By themselves, the component fields ϕ_{D1} and ϕ_{D2} do not satisfy these mixed boundary conditions, but when summed coherently as in Figs. 2.10 and 2.11 the mixed boundary conditions are satisfied. Note that a good approximation to the total diffracted fields in Figs. 2.10 and 2.11, valid outside the transition zone, is available by SDP evaluation of Eq.(2.30) directly without the partitioning into the component fields. The details of the transition region are lost, but outside the transition region the diffracted

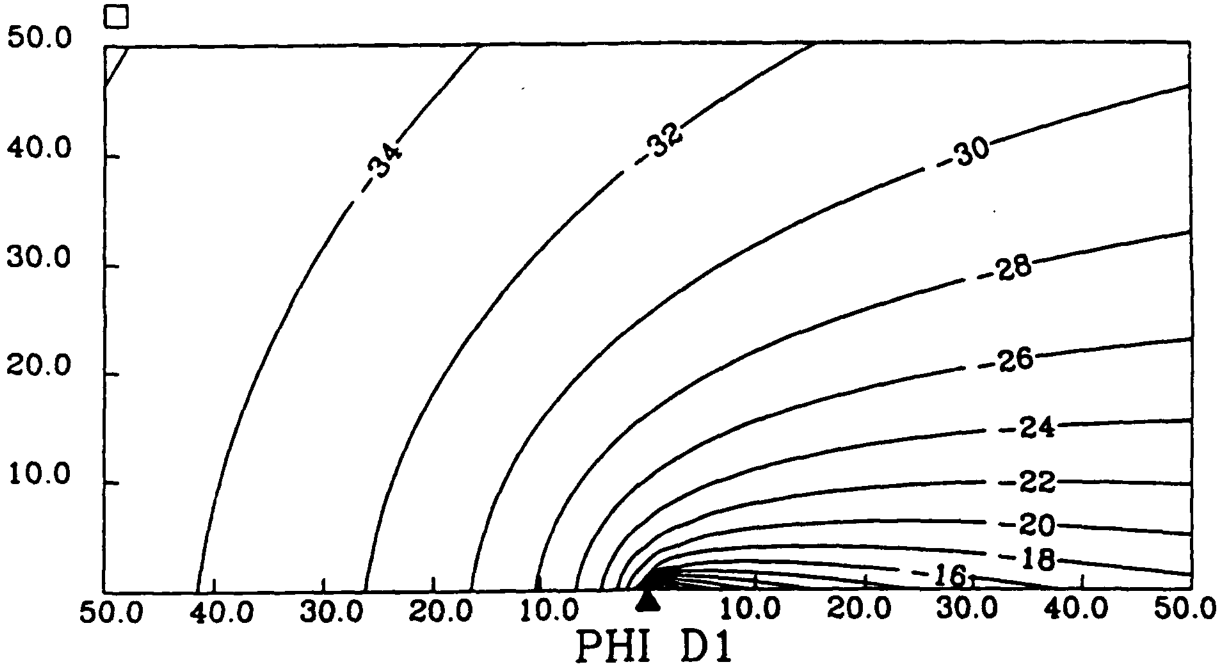

Figure 2.6: Contours of equal amplitude of $\phi_{D1}(r,\theta)$ for $\alpha = 15^o$. The boundary discontinuity at the origin is marked by the triangle, with the free surface boundary on the left side and perfectly rigid surface on the right side. The distance from the origin is in units of $10 \cdot kr$. The contour levels are in dB referenced to a unit amplitude incident wave field.

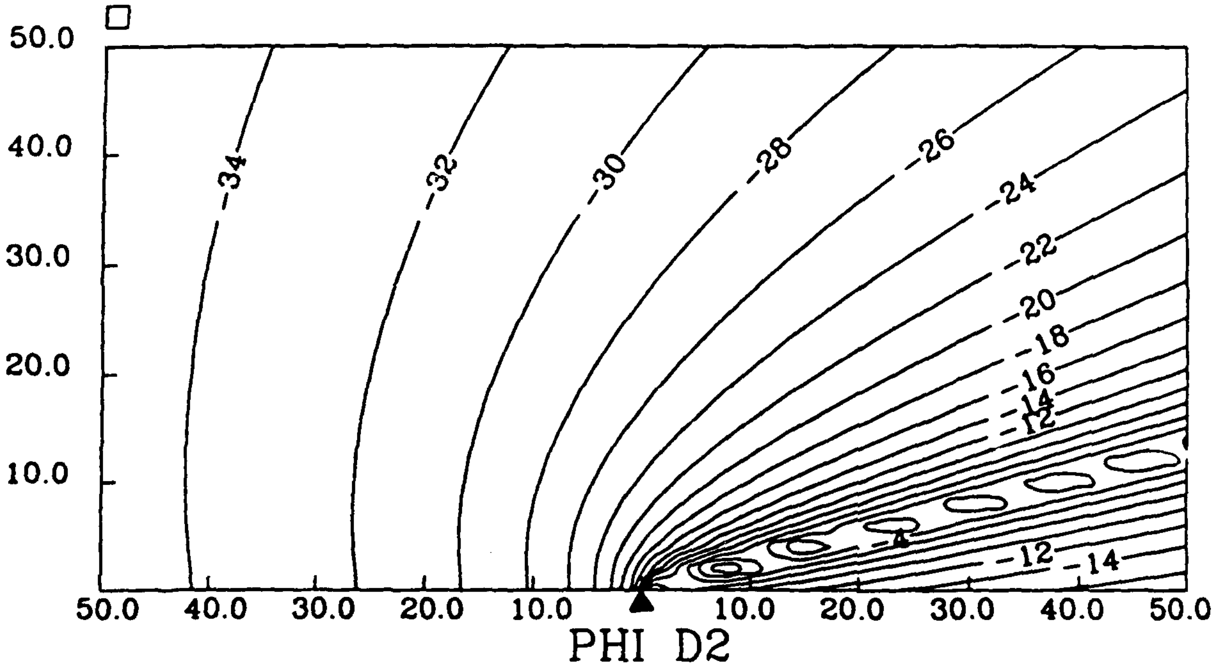

Figure 2.7: Contours of equal amplitude of $\phi_{D2}(r,\theta)$ for $\alpha = 15^o$. The boundary discontinuity at the origin is marked by the triangle, with the free surface boundary on the left side and perfectly rigid surface on the right side. The distance from the origin is in units of $10 \cdot kr$. The contour levels are in dB referenced to a unit amplitude incident wave field.

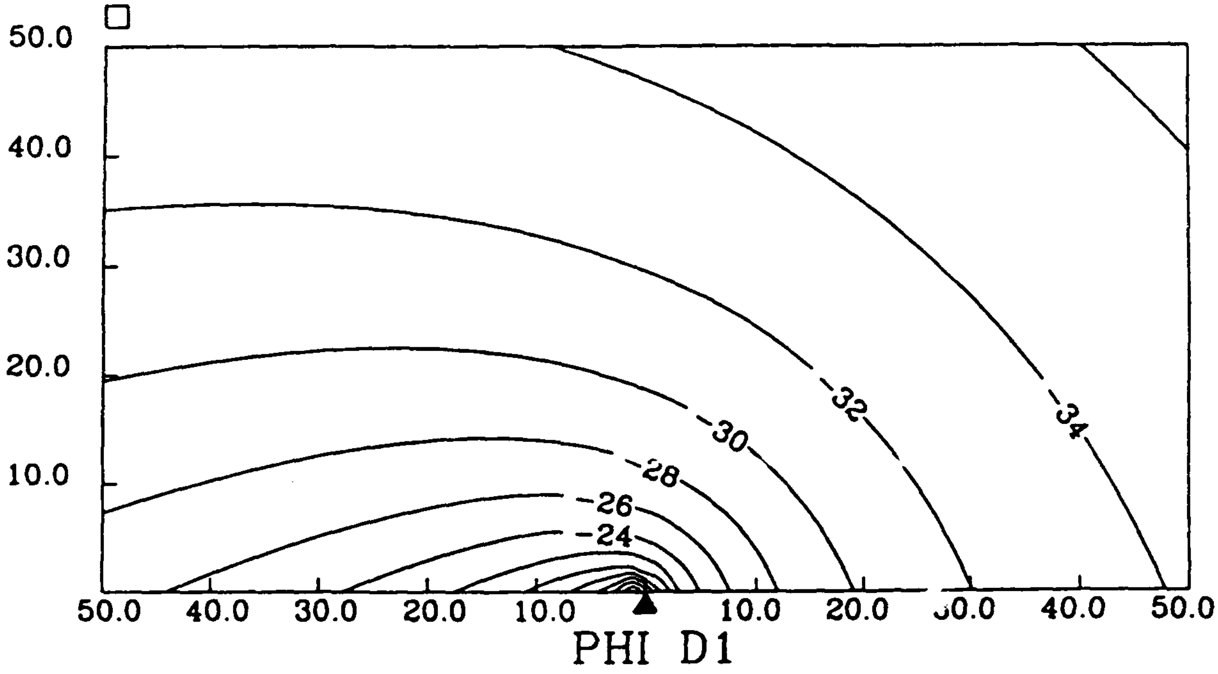

Figure 2.8: Contours of equal amplitude of $\phi_{D1}(r,\theta)$ for $\alpha = 135^o$. The boundary discontinuity at the origin is marked by the triangle, with the free surface boundary on the left side and perfectly rigid surface on the right side. The distance from the origin is in units of $10 \cdot kr$. The contour levels are in dB referenced to a unit amplitude incident wave field.

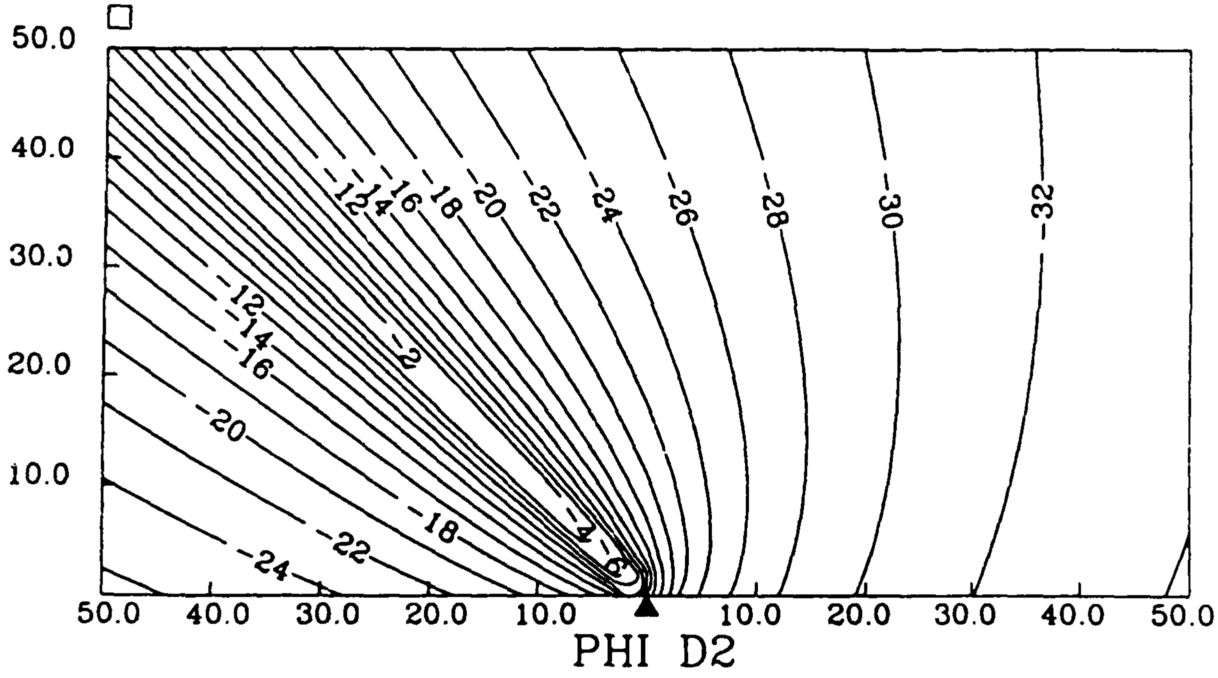

Figure 2.9: Contours of equal amplitude of $\phi_{D2}(r,\theta)$ for $\alpha = 135^o$ The boundary discontinuity at the origin is marked by the triangle, with the free surface boundary on the left side and perfectly rigid surface on the right side. The distance from the origin is in units of $10 \cdot kr$. The contour levels are in dB referenced to a unit amplitude incident wave field.

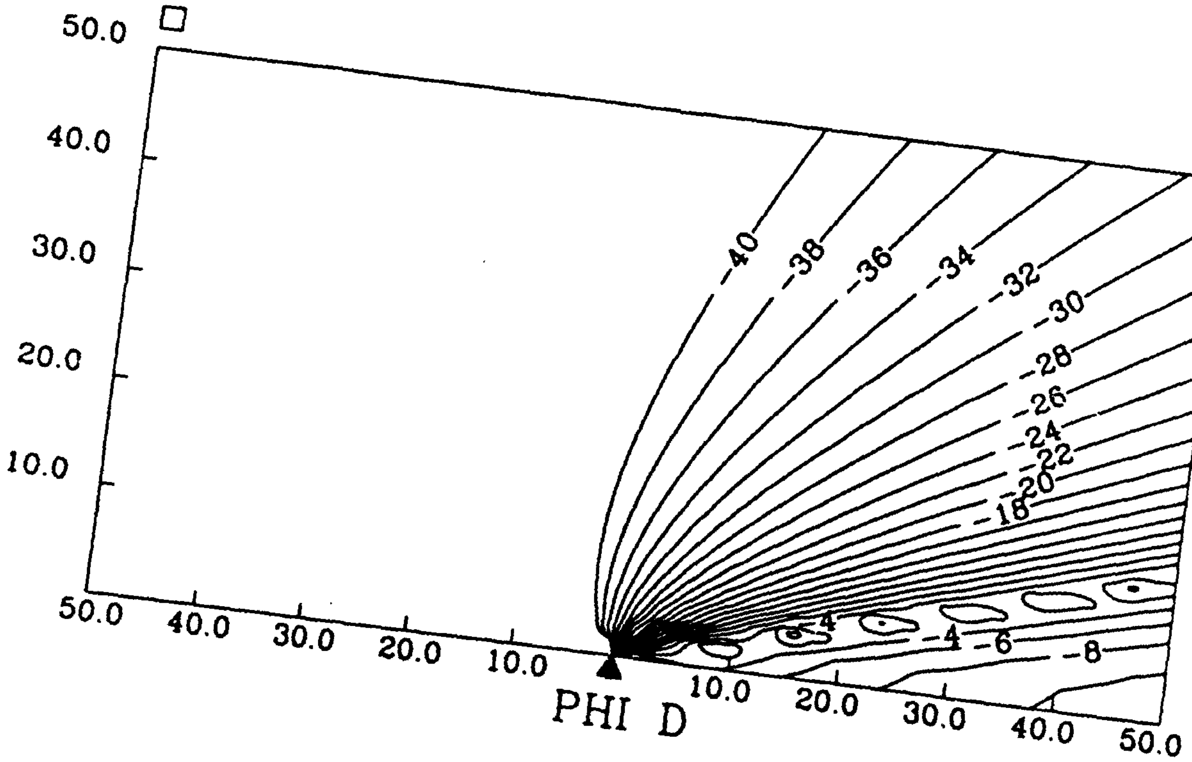

Figure 2.10: Contours of equal amplitude of $\phi_D(r,\theta)$ for $\alpha = 15^o$. The boundary discontinuity at the origin is marked by the triangle, with the free surface boundary on the left side and perfectly rigid surface on the right side. The distance from the origin is in units of $10 \cdot kr$. The contour levels are in dB referenced to a unit amplitude incident wave field.

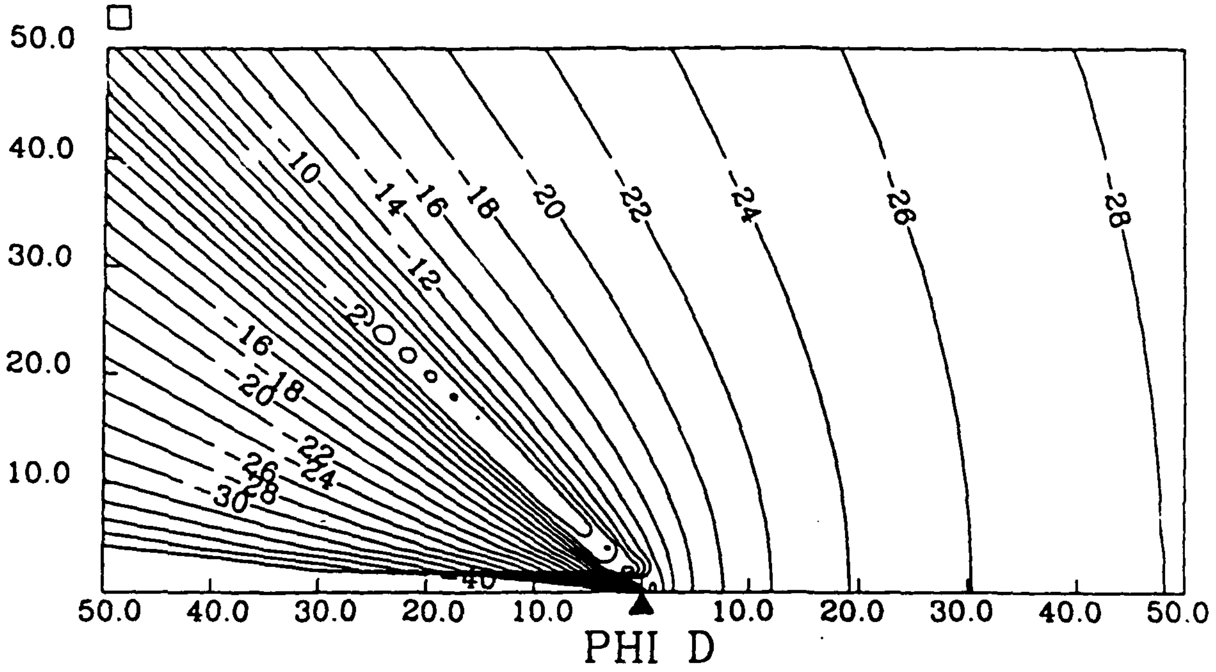

Figure 2.11: Contours of equal amplitude of $\phi_D(r,\theta)$ for $\alpha = 135°$. The boundary discontinuity at the origin is marked by the triangle, with the free surface boundary on the left side and perfectly rigid surface on the right side. The distance from the origin is in units of $10 \cdot kr$. The contour levels are in dB referenced to a unit amplitude incident wave field.

field behaves like

$$\phi_D(r,\theta) \sim P(\theta)\frac{e^{ikr}}{\sqrt{kr}}. \tag{2.62}$$

which is equivalent to the far field of a line source located at the point of discontinuity in the boundary. The far field radiation pattern here is equal to $P(\theta)$, which is Eq.(2.31) evaluated at the saddle point.

Returning to the analysis using the partitioned fields, for $x < 0, y = 0$ the residue of ϕ_{D2} provides the necessary geometric or plane wave field to combine with ϕ_I and ϕ_R such that the boundary condition Eq.(2.1) is satisfied by the plane waves. We will refer to plane wave fields as $O(1)$ fields because of their non-decaying radial dependence, and the mixed boundary conditions must always be satisfied separately by the $O(1)$ fields. The cylindrical spreading fields of ϕ_{D1} and ϕ_{D2} are $O(\epsilon)$ with $\epsilon = 1/\sqrt{kr}$. (We note that ϕ_{D2} is a cylindrical spreading field as described by $\mathcal{F}_A$, except within the transition region.) These fields are in exact anti-phase to $O(\epsilon)$ along the $x < 0$ boundary, with the exception of the vicinity of origin where the asymptotic representations are not valid, and thus satisfy the boundary condition to $O(\epsilon)$. This is easily seen by evaluating Eq.(2.36) and Eq.(2.45) at $\theta = 0$. The asymptotic form of $\phi_{D2} = \mathcal{F}_A$ is entirely adequate here because we are well out of the transition region.

Rather than examining higher order terms of the asymptotic series, a better way to ascertain the exactness of the solution is to examine the original integral representation

$$\phi_D(x,0) = -2i\sqrt{k\cos\alpha - k}\int_{-\infty}^{\infty}\frac{e^{iqx}}{\sqrt{q-k}(q - k\cos\alpha)}\frac{dq}{2\pi}. \tag{2.63}$$

For $x < 0$ we capture the necessary pole contribution but this is the only contribution to the integral as can be seen by extending the contour into a semi-circle in the lower half-plane and applying Jordan's lemma [36]. Checking the boundary condition for $x > 0$ in the same manner we have

$$\frac{\partial}{\partial y}\phi_D(x,0) = 2i\sqrt{k\cos\alpha - k}\int_{-\infty}^{\infty}\frac{\sqrt{q+k}}{(q - k\cos\alpha)}e^{iqx}\frac{dq}{2\pi}. \tag{2.64}$$

Here there is only a branch line beginning at $q = -k$ and extending into the lower half-plane. For $x > 0$ we evaluate the integral by extending the contour into a semi-circle in the upper half-plane and apply Jordan's lemma. The pole at $q = k\cos\alpha$ will not be captured

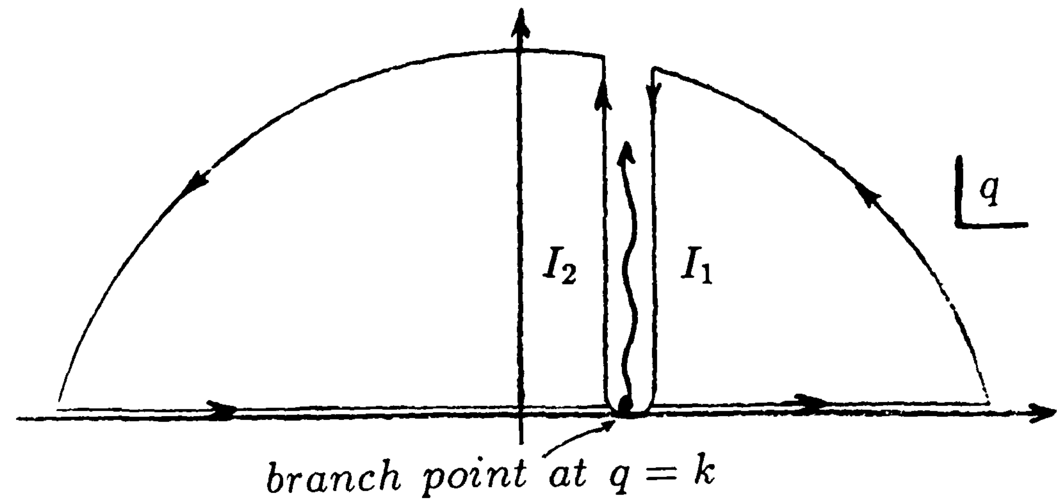

Figure 2.12: Branch line integral for evaluating $\phi_D(x,0)$ and $x > 0$.

because it lies just below the real-q axis. The integral is zero and the boundary condition [Eq.(2.2)] is satisfied exactly. In the remainder of this thesis it will be sufficient to report the inverted field solution to $O(\epsilon)$, which is all that is required to extract far field diffraction intensity information. This solution satisfies the mixed boundary condition to $O(\epsilon)$ with an error of $O(\epsilon^3)$.

It is interesting to note the behavior of $\phi_D(x,0)$ for $x > 0$. This is best done by working directly with the integral representation and evaluating the necessary branch line integral due to the $\sqrt{q-k}$ factor in $G(q)$ (Fig. 2.12).

The two branch line integrals are

$$I_1 = e^{ikx - i\frac{\pi}{2}} \int_0^\infty \frac{e^{-\rho x}}{(k\cos\alpha - k - \rho e^{i\frac{\pi}{2}})\sqrt{\rho e^{i\frac{\pi}{2}}}} d\rho \tag{2.65}$$

and

$$I_2 = e^{ikx - i\frac{3\pi}{2}} \int_0^\infty \frac{e^{-\rho x}}{(k\cos\alpha - k - \rho e^{-i\frac{3\pi}{2}})\sqrt{\rho e^{-i\frac{3\pi}{2}}}} d\rho \tag{2.66}$$

with $q = \rho e^{i\frac{\pi}{2}} + k$ on I_1 and $q = \rho e^{-i\frac{3\pi}{2}} + k$ on I_2 and ρ the integration variable. Expanding the denominators of the integrands in a Taylor series about small ρ and integrating gives

$$\phi_D(x,0) = -(1+i)\sqrt{\frac{2}{\pi}}\frac{1}{\sqrt{1-\cos\alpha}}\frac{e^{ikx}}{\sqrt{kx}} + O(\frac{1}{(kx)^{\frac{3}{2}}}) \tag{2.67}$$

as the net lowest order result. For now let us simply note that ϕ_D is characterized by $O(\epsilon)$ behavior along the perfectly rigid or ***infinite*** impedance part of the two-part planar surface. In the next chapter we contrast this behavior with the behavior of ϕ_D along a *finite* impedance surface.

2.5 Summary

In this chapter the exact solution to a canonical diffraction problem was determined using the Wiener-Hopf method. The solution was expressed in terms of a continuous plane wave spectrum $G(q)$, or the equivalent angular spectrum $P(\beta)$. The spectrum corresponds to the diffracted field which results from a monochromatic plane wave incident upon two coupled half-planes, one surface characterized by the Dirichlet boundary condition the other surface characterized by the Neumann boundary condition.

The spectrum was partitioned into a term which is free of singularities, $P_1(\beta)$, and $P_2(\beta)$ which retained the pole at $\beta = \pi - \alpha$ that corresponds to the angle of specular reflection. This gave way to two components of the diffracted field ϕ_{D1} and ϕ_{D2}. The first was expressed as an asymptotic series valid for $kr \gg 1$, while the second was expressed by the Fresnel integral defined functionally as $\mathcal{F}(r,\theta;\alpha)$ and evaluated exactly. Fundamental properties of $\mathcal{F}(r,\theta;\alpha)$ and its asymptotic form $\mathcal{F}_A(r,\theta;\alpha)$ were derived, including the radial derivative $\frac{\partial\mathcal{F}(r,\theta;\alpha)}{\partial r}$ which will be used later in diffraction field intensity calculations.

The canonical problem is a highly idealized rendition of what happens when a plane wave is incident upon a water-to-ice canopy surface. Nevertheless, some essential features of the diffraction process are reproduced in the solution. These include a diffracted field containing a residue contribution which restores field continuity along the line dividing the regions of specular reflection, and a cylindrical wave contribution which maintains the mixed boundary conditions. This solution will serve as a guideline to the more realistic boundary conditions to be addressed in the next two chapters.

Chapter 3

Diffraction problem with locally reacting boundary condition

This chapter presents the solution to the problem of a monochromatic plane acoustic wave incident upon a surface in which the boundary surface impedance changes abruptly from a free surface, or zero impedance, to a locally reacting finite impedance. The difference between this problem and the one presented in Chapter 2, is that here a finite impedance has replaced the infinite impedance or Neumann boundary condition. We will show subsequently that this problem is a useful model for the free surface-to-ice surface boundary change, and ultimately the ice lead diffraction process.

3.1 The locally reacting boundary condition for ice at low frequency

A locally reacting surface is one for which the input (surface) impedance Z_{in}, defined as the ratio of acoustic pressure to normal particle velocity evaluated at the surface, is independent of horizontal wavenumber. Let us assume for the moment that the boundary surface consists of a single thin (with respect to any wavelength scale) layer or plate, and this surface is a locally reacting one. From Newton's second law

$$m \ \frac{\partial V_p}{\partial t} = P \tag{3.1}$$

where m is the mass per unit area of the plate, V_p is the velocity of a point on the surface of the plate into the medium, in response to P the acoustic pressure on the plate-medium boundary [62] Taking the ratio of pressure to normal velocity, assuming $e^{-i\omega t}$ time dependence, the input impedance of the plate is

$$Z_{in} = -i\omega m. \tag{3.2}$$

This is a locally reacting, finite impedance; it is locally reacting because there is no dependence upon horizontal wavenumber and finite because it no longer has the perfectly rigid property. Here, the plate impedance is due only its mass. Real plate material of course can be elastic, and this formulation does not take into account the elasticity of the plate.

It is instructive to examine the input impedance of a floating ice sheet or plate from this point of view. If the plate material consists of a single homogeneous layer of total thickness H, the full set of equations from linear elasticity theory is no longer necessary to derive the input impedance. Here, a simpler formulation, often referred to as the Rayleigh-Lamb equations [32], is sufficient to determine the plate input impedance. With kH values below cut-off for higher order mode propagation in the plate, only the two fundamental modes from the Rayleigh-Lamb equations are necessary for a complete description of the plate input impedance. These are known as the longitudinal mode (symmetric Lamb mode) and the flexural mode (anti-symmetric Lamb mode). The wave impedances of the longitudinal mode Z_{-} and the flexural mode $Z_{\sim}$ add in parallel to form the total input impedance for the plate. These impedances are given by [49]

$$Z_{-}(q) = \frac{-i\omega\rho_1}{\gamma_l k_t^4} \cdot [(\gamma_t^2 + q^2)^2 \coth\gamma_l \frac{H}{2} - 4\gamma_l\gamma_t q^2 \coth\gamma_t \frac{H}{2}] \tag{3.3}$$

and

$$Z_{\sim}(q) = \frac{-i\omega\rho_1}{\gamma_l k_t^4} \cdot [(\gamma_t^2 + q^2)^2 \tanh\gamma_l \frac{H}{2} - 4\gamma_l\gamma_t q^2 \tanh\gamma_t \frac{H}{2}]. \tag{3.4}$$

Here, $\gamma_t = \sqrt{q^2 - k_t^2}$ and $\gamma_l = \sqrt{q^2 - k_l^2}$, are the shear and compressional vertical wave numbers in the ice, with $k_t = \frac{\omega}{c_t}$ and $k_l = \frac{\omega}{c_l}$, where c_t is the shear wave speed and c_l is the compressional wave speed in the ice and ρ_1 is the ice density. The ambient water sound speed and density will be referred to as c and ρ, respectively. Typical values of sea ice parameters which will be used in this thesis are:

- $c_l = 3500$ m/s
- $c_t = 1800$ m/s
- $\rho_1 = 920$ kg/m^3

We will use the nominal values of 1450 m/s and 1000 kg/m^3 for the ambient water sound speed and density, and ignore the small energy dissipation within the ice which would be represented by a small negative imaginary part in the ice wave speeds.

Examining Eqs.(3.3) and (3.4) for small values of kH (e.g., $kH \lesssim 1$) shows that $|Z_-| \gg |Z_\sim|$, and since the two wave impedances add in parallel we have $Z_{in} \approx Z_\sim$. The flexural wave impedance can be expanded in terms of $\gamma_t H$ and $\gamma_l H$ when the arguments of the hyperbolic functions are small and these functions are replaced by their Taylor expansions, with the result to leading order [49]

$$Z_\sim = -i\omega\rho_1 H + O(\gamma_t \frac{H}{2}, \gamma_l \frac{H}{2})^3 \tag{3.5}$$

which gives us our original mass loading formulation with $m = \rho_1 H$. With this approximation, elastic resistance to deformation is neglected and inertial effects, or mass loading, is dominant. The neglect of Z_- in favor of $Z_\sim$ in the parallel additions is consistent with our use in Chapter 4 of the Euler-Bernoulli or thin plate equation [58] to account for the elastic effects of ice.

This marks a convenient point to skip ahead and briefly discuss the thin plate equation in the context of the input impedance of ice, and the locally reacting boundary condition. Specifically, let us reach the same conclusion of Eq.(3.5) more directly via the thin plate equation. For small values of kH it is customary to work with the thin plate equation rather than the Rayleigh-Lamb formulation. (Various guidelines exist for determining when the thin plate equation can be used e.g., [43,27]. These all more or less satisfy the criterion $kH \lesssim 1$, which we discuss in more detail in Chapter 4.) Then, the vertical plate deflection $U = U(x)$ of a thin plate is governed by

$$B\frac{\partial^4}{\partial x^4}U - \rho_1 H\omega^2 U = P(x;t) \tag{3.6}$$

which includes the usual two-dimensional assumption that $\frac{\partial U}{\partial y} = 0$ and harmonic time dependence of $e^{-i\omega t}$. The first term on the left characterizes elastic effects, or the springlike resistance of the plate to bending, and the second term characterizes inertial effects. The forcing term, $P(x;t)$, in our case will be the pressure due to a plane acoustic wave incident upon the ice, or equivalently, it is the loading of the ambient fluid medium.

The bending stiffness B is defined

$$B = \frac{EH^3}{12\ (1-\sigma^2)} \tag{3.7}$$

where E is Young's modulus and σ is Poisson's ratio, with

$$E = 2\mu(1+\sigma). \tag{3.8}$$

For an isotropic elastic medium [70] Poisson's ratio and the Lamé constants λ, μ are related as follows

$$\sigma = \frac{.5\lambda}{\lambda+\mu} \leq .5 \qquad c_t = \sqrt{\frac{\mu}{\rho_1}} \qquad c_l = \sqrt{\frac{\lambda+2\mu}{\rho_1}}. \tag{3.9}$$

For comparative purposes $\sigma \simeq .32$ and $E \simeq 8 \cdot 10^9$ Pascals are typical values for sea ice.

When its elastic properties are described by the thin plate equation, the input impedance of ice can be expressed as [43]

$$Z_{in} = -i\omega\rho_1 H(1 - \frac{q^4}{k_f^4}) \tag{3.10}$$

where q is the variable for horizontal wavenumber as used in Chapter 2. The wavenumber *in vacuo*, k_f, is a solution to the characteristic equation corresponding to Eq.(3.6) with the forcing term set to zero,

$$k_f^4 = \frac{\rho_1 H\omega^2}{B}. \tag{3.11}$$

We will find for meters-thick ice and frequencies in the range of 50 Hz or less, that $\rho_1 H\omega^2 \gg q^4 B$ is always satisfied by homogeneous values of q $(q/k < 1)$. Thus a leading order approximation for Z_{in} equivalent to the one in Eq.(3.5) is available simply by inspection of Eq.(3.10).

We have argued here the merits of a locally reacting approximation for the input impedance of an ice plate. The approximation being, at low kH values and in the homogeneous region of the horizontal wave number spectrum, the ice surface impedance is purely reactive and characterized by mass loading.

The locally reacting approximation allows us to replace continuity of pressure and particle velocity at an interface with a single impedance boundary condition [58]

$$\frac{\partial \phi_T}{\partial y} = \frac{-i\omega\rho}{Z_{in}}\phi_T \tag{3.12}$$

evaluated on the boundary, and where Z_{in} is a constant. To simplify notation for later use, we define an admittance parameter

$$\eta = \frac{-i\omega\rho}{Z_{in}}, \tag{3.13}$$

which becomes $\frac{\rho}{\rho_1 H}$ in the locally reacting approximation. Figure 3.1 is a plot of the modulus of $\eta(q)$ for sea ice with $H = 1$ m and a frequency of 30 Hz, computed (1) exactly using the full elastic equations and the Thomson-Haskell matrix representation of layered constant elastic material [72,29], and (2) using the analytical expression [Eq.(3.4)] for $Z_{\sim}$. The small perturbation near .5 is due to the effect of the longitudinal wave as computed in the exact calculation. Both functions become singular near 3.6, indicating a solution of $Z_{in} = 0$ or the flexural wave *in vacuo*. In the homogeneous region ($q/k < 1$) of the wavenumber spectrum, $\eta(q)$ is nearly exactly described by the simple constant $\frac{\rho}{\rho_1 H}$ which confirms the locally reacting nature of the input impedance.

3.2 Solution of the finite impedance, locally reacting diffraction problem

In this section we solve the problem of a monochromatic plane wave with grazing angle α, incident upon a planar surface with the following mixed boundary conditions

$$\phi_T(x,0) = 0 \quad x < 0 \tag{3.14}$$

$$\frac{\partial \phi_T(x,0)}{\partial y} = \eta\phi_T(x,0) \quad x > 0 \tag{3.15}$$

with the problem geometry and coordinate system the same as in Chapter 2. It will be convenient later in this thesis to assume that ϕ_R is the reflected field corresponding to a free surface but which is applied to the entire surface. Then, using this combination of ϕ_I

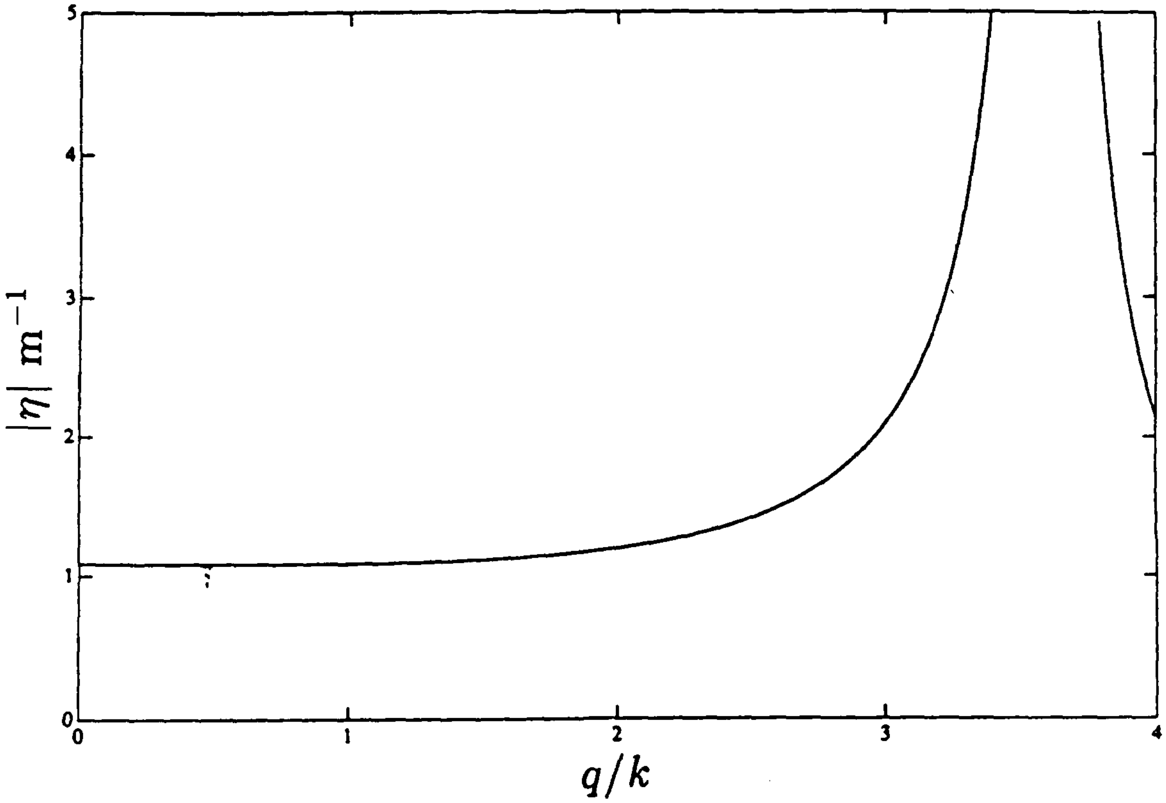

Figure 3.1: Plot of the modulus of $\eta(q)$ corresponding to sea ice with $H = 1$ m and a frequency of 30 Hz. Normalized wavenumber (q/k) is used with $q/k < 1$ representing the homogeneous wavenumber spectrum. The solid line is the calculation based on $Z_{\sim}(q)$; the dashed line is exact calculation.

and ϕ_R, the properties of ϕ_D along the boundary must necessarily be

$$\phi_D(x,0) = 0 \quad x < 0 \tag{3.16}$$

$$\frac{\partial \phi_D(x,0)}{\partial y} = \eta \phi_D(x,0) + 2ik \sin \alpha e^{ikx\cos\alpha} \quad x > 0 \tag{3.17}$$

in order to maintain the boundary conditions.

As in Chapter 2, we start with an integral form of $\phi_D(x,y)$ [Eq.(2.9)] representing a continuous superposition of plane waves. Applying the semi-infinite transform definition to what is known about $\phi_D(x,0)$ [Eq.(3.16)] gives,

$$G(q) = G_-(q) \tag{3.18}$$

and applying what is known about $\frac{\partial \phi_D(x,0)}{\partial y}$ [Eq.(3.17)] gives,

$$\sqrt{q^2 - k^2} G(q) = -L_+(q) - \eta G_-(q) + \frac{-2k \sin \alpha}{(q - k \cos \alpha)}. \tag{3.19}$$

Again $G_-(q)$ and $L_+(q)$ are unknown functions, with the last term on the right of Eq.(3.19) now being a '$-$' function since it is a result of a semi-infinite ($x > 0$) Fourier transform of the boundary conditions. Combining the above two equations leads to the Wiener-Hopf functional equation

$$L_+(q) = \frac{-2k \sin \alpha}{(q - k \cos \alpha)} - G_-(q)(\sqrt{q^2 - k^2} + \eta). \tag{3.20}$$

If $\eta \rightarrow 0$ we recover an equivalent equation for an infinitely rigid surface.

To proceed, requires a multiplicative decomposition of the kernel

$$K(q) = \sqrt{q^2 - k^2} + \eta = \frac{K_-(q)}{K_+(q)}. \tag{3.21}$$

The exact decomposition of kernels of this form has been accomplished in earlier applications of the Wiener-Hopf method in electromagnetics [64] and acoustics [35], using Cauchy's second integral theorem. However, the results of the exact decomposition remain in the form of intractable contour integrals, with a resulting complexity that limits useful interpretation of the solution. A way to get around this is to use an asymptotic decomposition for the small parameter $\eta \rightarrow 0$ [22], but this only applies for a perturbation from a pefectly rigid surface, and in our case η is not small. We therefore approximate this kernel by one which can be more easily decomposed. One motivation behind the approximation is the following: if we can find an approximate kernel $\hat{K}(q)$ which duplicates the behavior of $K(q)$ along the inversion contour in the complex-q plane, then the transformed (x domain) solution will be a good approximation to the exact solution [44]. An alternative motivation arises from the observation that the Wiener-Hopf procedure is a convolution process in the x domain. Thus, if a substitute kernel is used which has the same area and effective width in the x domain as does $K(q)$ in the x domain, the result of convolution is expected to be nearly the same [13]. In this problem we match the area plus the first three moments of $K(q)$ which leads to a very accurate approximate kernel $\hat{K}(q)$. Matching the moments of the transformed $K(q)$ effectively translates into matching the behavior of $K(q)$ along the inversion contour in the complex q-plane. In the homogeneous part of the wavenumber spectrum $|q| < k$, the approximate kernel is essentially without error, and there is no loss in far-field accuracy. Details of the approximation procedure and multiplicative decomposition are presented in Appendix B.

Upon using the decomposed approximate kernel

$$\hat{K}(q) = \frac{\hat{K}_-(q)}{\hat{K}_+(q)}, \tag{3.22}$$

Eq.(3.20) becomes,

$$L_+(q)\hat{K}_+(q) = \frac{-2k\sin\alpha}{(q - k\cos\alpha)}\hat{K}_+(q) - G_-(q)\hat{K}_-(q). \tag{3.23}$$

The first term on the right of Eq.(3.23) is decomposed additively in the manner of Chapter 2, with

$$R_-(q) = \frac{-2k\sin\alpha}{(q - k\cos\alpha)}\hat{K}_+(k\cos\alpha) \tag{3.24}$$

and

$$R_+(q) = \frac{2k\sin\alpha}{(q - k\cos\alpha)}\hat{K}_+(k\cos\alpha) - \frac{2k\sin\alpha}{(q - k\cos\alpha)}\hat{K}_+(q) \tag{3.25}$$

and we rewrite Eq.(3.23) as

$$-L_+(q)\hat{K}_+(q) - R_+(q) = G_-(q)\hat{K}_-(q) - R_-(q) = E(q) \tag{3.26}$$

with $E(q)$ being an entire function. The decomposed kernel takes the form

$$\hat{K}_-(q) = \frac{(q - i\sqrt{k^2 + \eta^2})}{\sqrt{q - ikn}} \cdot \frac{(q - kA_1)}{(q - kA_2)} \tag{3.27}$$

$$\hat{K}_+(q) = \frac{\sqrt{q + ikn}}{(q + i\sqrt{k^2 + \eta^2})} \cdot \frac{(q + kA_2)}{(q + kA_1)}$$

with the constants A_1,A_2 and parameter n defined in Appendix B.

Edge conditions are the same as those defined in Chapter 2. Thus, since $|\hat{K}_-(q)| \sim |q|^{\frac{1}{2}}$ as $|q| \to \infty$, the '−' side of Eq.(3.26) behaves at most as $\sim |q|^{\frac{-1}{2}}$ as $|q| \to \infty$. The entire function is therefore identically zero, giving

$$G_-(q) = \frac{-2k\sin\alpha \;\; \hat{K}_+(k\cos\alpha)}{(q - k\cos\alpha)\hat{K}_-(q)}. \tag{3.28}$$

3.3 Inversion of the diffracted field plane wave spectrum

For the inversion $G_-(q)$ back to $\phi_D(r,\theta)$, we follow the pathway laid out in the canonical problem. Though this plane wave spectrum is significantly different from the one determined in the canonical problem, they do share common features. One common feature is the pole at $q = k\cos\alpha$, which adds a necessary correction to the geometric fields. Another is the '−' function $\sqrt{q-k}$ in the canonical spectrum being replaced by $\hat{K}_-(q)$. Thus it will be fruitful to rearrange the algebra here in order to use again some of the functional forms established in the previous chapter for the canonical problem. The inversion integral now takes the form

$$\phi_D(r,\theta) = \chi \int_\Gamma P(\beta) M(\beta) e^{ikr\cos(\beta-\theta)} d\beta, \tag{3.29}$$

where

$$\chi = \frac{-k\sin\alpha}{\pi} \hat{K}_+(k\cos\alpha), \tag{3.30}$$

and

$$M(\beta) = \frac{-\cos\frac{\beta}{2}}{\hat{K}_-(-k\cos\beta)}. \tag{3.31}$$

with the inversion contour Γ shown in Fig. 3.2.

Note that this contour is nearly the same one used in Chapter 2 (Fig. 2.4), but the orientation of the pole at $\beta = \pi - \alpha$ has changed because of our use in this case of a free surface reflected field as ϕ_R.

In Eq.(3.29) the $P(\beta)$ is the same angular spectrum determined from the canonical problem in Chapter 2 and $M(\beta)$ is a new function defined in this thesis as the material

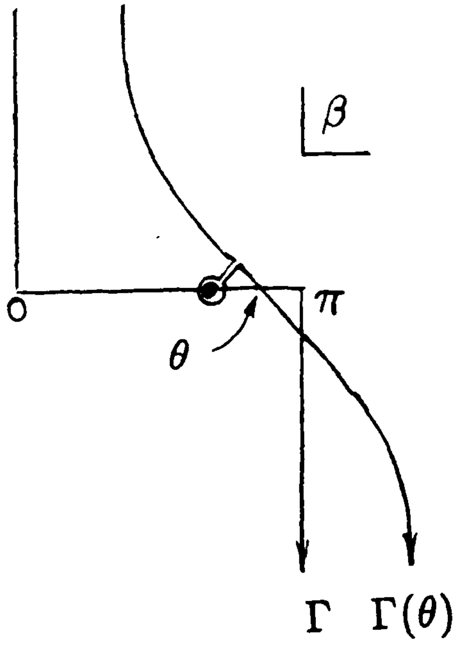

Figure 3.2: Inversion contour Γ and deformed SDP contour $\Gamma(\theta)$. The pole at $\beta = \pi - \alpha$ is captured when $\theta > \pi - \alpha$.

function, dependent upon ρ, ρ_1 and H. In the canonical problem there was no material involved, because the surface was perfectly rigid. Introducing a finite impedance or "material" modifies the canonical angular spectrum. By using a very accurate approximate kernel, we have determined a useable form for $M(\beta)$ which is well-behaved for $0 < Re(\beta) < \pi$. We can also proceed with the steepest descent analysis using the angular spectrum partitioning of Chapter 2, accordingly

$$\phi_D(r,\theta) = \chi \int_\Gamma (P_1(\beta) + P_2(\beta))M(\beta)e^{ikr\cos(\beta-\theta)}d\beta. \tag{3.32}$$

Carrying out the inversion in this manner now gives three fields which are added coherently to comprise $\phi_D(\rho,\theta)$. The first field results from a SDP evaluation and is

$$\phi_{D1}(r,\theta) = (1-i)\sqrt{\pi}\chi P_1(\theta)M(\theta)\frac{e^{ikr}}{\sqrt{k\rho}} + O(\frac{1}{(kr)^{\frac{3}{2}}}) \tag{3.33}$$

with a remaining part

$$I(r,\theta) = \chi \int_\Gamma P_2(\beta))M(\beta)e^{ikr\cos(\beta-\theta)}d\beta. \tag{3.34}$$

We treat the integral in Eq.(3.34) exactly the same way as in Eq. (2.41). The only difference here is that this integral yields a residue field contribution for the angular sector $\theta > \pi - \alpha$, rather than for the sector $\theta < \pi - \alpha$ as before. The resulting geometric field is

$$\phi_{geo}(r,\theta) = -2\pi i\chi \frac{M(\pi-\alpha)}{\sin\frac{\alpha}{2}} e^{-ikr\cos(\alpha+\theta)}. \tag{3.35}$$

Examining the complex amplitude for the above plane wave more closely we see that

$$-2\pi i\chi \frac{M(\pi-\alpha)}{\sin\frac{\alpha}{2}} = -2ik\sin\alpha \frac{\hat{K}_+(k\cos\alpha)}{\hat{K}_-(k\cos\alpha)} = \frac{-2ik\sin\alpha}{\hat{K}(k\cos\alpha)}. \tag{3.36}$$

We can leave the amplitude in this form, or use the fact that the difference between $K(q)$ and $\hat{K}(q)$ in the homogeneous wavenumber region is at most a few percent; thus substituting $K(k\cos\alpha)$ for $\hat{K}(k\cos\alpha)$ we have

$$-2\pi i\chi \frac{M(\pi-\alpha)}{\sin\frac{\alpha}{2}} = \frac{-2ik\sin\alpha}{K(k\cos\alpha)} = 1 + R(\alpha) \tag{3.37}$$

where $R(\alpha)$ is the plane wave reflection coefficient for the locally reacting surface evaluated at grazing angle α. The equality in Eq. (3.37) will be used in the remainder of this thesis. The resulting geometric field has complex amplitude $1 + R(\alpha)$, where the first term cancels the free surface reflection which exists along the entire boundary but which applies only for $x < 0$. The second term combined with the incident field satisfies the boundary condition for $x > 0$.

Continuing with the integral in Eq.(3.34) we rewrite $P_2(\beta)M(\beta)$ as

$$P_2(\beta)M(\beta) = P_2(\beta)M(\pi-\alpha) + P_2(\beta)[M(\beta) - M(\pi-\alpha)]. \tag{3.38}$$

Using this expression in Eq.(3.34) the result from the first term is the Fresnel integral modified by a constant. The integral of the second bracketed term, is now well-behaved for $0 < Real(\beta) < \pi$, since the pole at $\beta = \pi - \alpha$ is cancelled, and is evaluated using the SDP contour. The complete inversion of Eq.(3.34) is then

$$\phi_{D2}(r,\theta) = \frac{1+R(\alpha)}{2}\mathcal{F}(r,\theta;\alpha) \tag{3.39}$$

plus

$$\phi_{D3}(r,\theta) = (1-i)\sqrt{\pi}\chi P_2(\theta)[M(\theta) - M(\pi-\alpha)]\frac{e^{ikr}}{\sqrt{kr}} + O(\frac{1}{(kr)^{\frac{3}{2}}}). \tag{3.40}$$

As in the canonical problem, the diffracted field is expressed in terms of an asymptotic series, and an exact expression for the Fresnel integral field. In this case the Fresnel integral field is modified by a complex amplitude factor $\frac{1+R(\alpha)}{2}$, which is one half the *difference* of the two reflection coeffcients involved. In the canonical problem the two reflection coefficients are -1 (free surface) and $+1$ (perfectly rigid surface); their difference is 2 and the amplitude of $\mathcal{F}(r,\theta;\alpha)$ is unity. The simple constant modifying $\mathcal{F}(r,\theta;\alpha)$ confirms the idea discussed in Chapter 2, that the Fresnel integral field exists to smooth the transition between the two geometrically reflected fields. Note that, except for the complex amplitude factor, $\mathcal{F}(r,\theta;\alpha)$ is exactly the same form for both the canonical and finite impedance problem. However; the introduction of finite impedance has given rise to a second cylindrically spreading component field ϕ_{D3}; this field together with the ϕ_{D1} component field adds coherently with ϕ_{D2} such that the boundary conditions are maintained.

3.4 The diffracted field and check of the boundary conditions

Contours of equal amplitude level for ϕ_{D1}, ϕ_{D2} and ϕ_{D3} are shown in Figs. 3.3, 3.4, and 3.5; the coherent sum of ϕ_{D1} and ϕ_{D3} is shown in Fig. 3.6. The incident field is a monochromatic plane wave of 50 Hz with $\alpha = 15^o$, with dB levels referenced to a unit amplitude incident wave field. The material can be considered that of ice in the locally reacting approximation, with $\rho_1 = .92$ and $H = 2$ m. The coherent sum of component fields which gives the total diffracted field $\phi_D(r,\theta)$ is shown in Fig. (3.7). The boundary condition [Eq.(3.14)] is satisfied to $O(1)$ by the plane wave incident and free surface reflected fields, with no residues in the integral representation of $\phi_D(x,0)$ captured for $x < 0$. The two fields resulting from the SDP evaluation, ϕ_{D1} and ϕ_{D3}, plus the asymptotic form of ϕ_{D2}, are in exact anti-phase to $O(\epsilon)$, $\epsilon = 1/\sqrt{kr}$, along this boundary and thus Eq.(3.14) is satisfied to $O(\epsilon)$.

For $x > 0, y = 0$ we need to take inventory of the geometric fields: the original incident and free surface reflected fields; a field resulting from capture of a pole for $x > 0, y = 0$ in

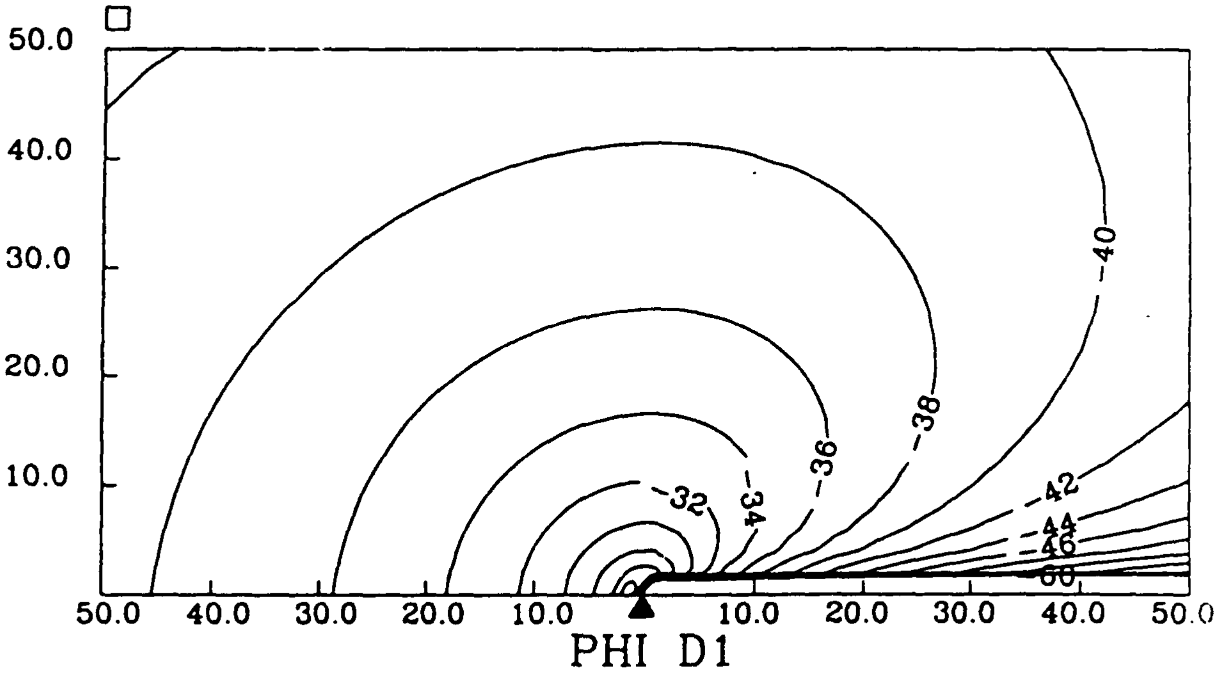

Figure 3.3: Contours of equal amplitude level for $\phi_{D1}(r, \theta)$ with $\alpha = 15^\circ$. The boundary discontinuity at the origin is marked by the triangle, with the free surface boundary on the left side and finite impedance surface on the right side. The distance from the origin is in units of $10 \cdot kr$. The contour levels are in dB referenced to a unit amplitude incident wave field.

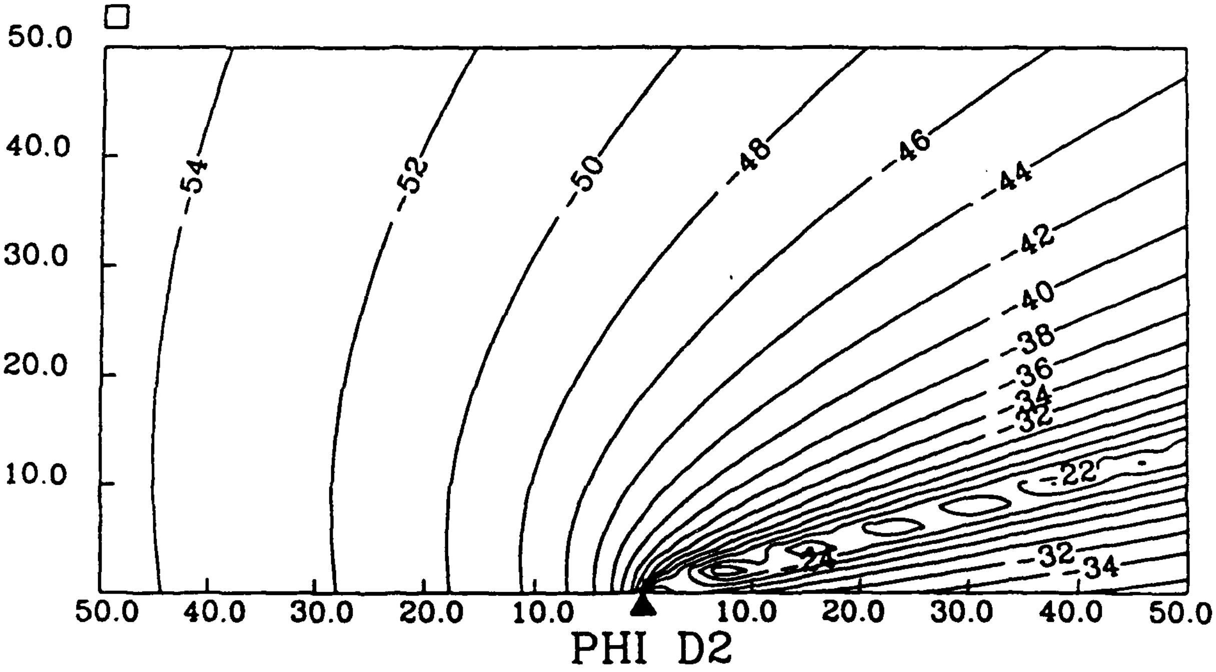

Figure 3.4: Contours of equal amplitude level for $\phi_{D2}(r,\theta)$ with $\alpha = 15^o$. The boundary discontinuity at the origin is marked by the triangle, with the free surface boundary on the left side and finite impedance surface on the right side. The distance from the origin is in units of $10 \cdot kr$. The contour levels are in dB referenced to a unit amplitude incident wave field.

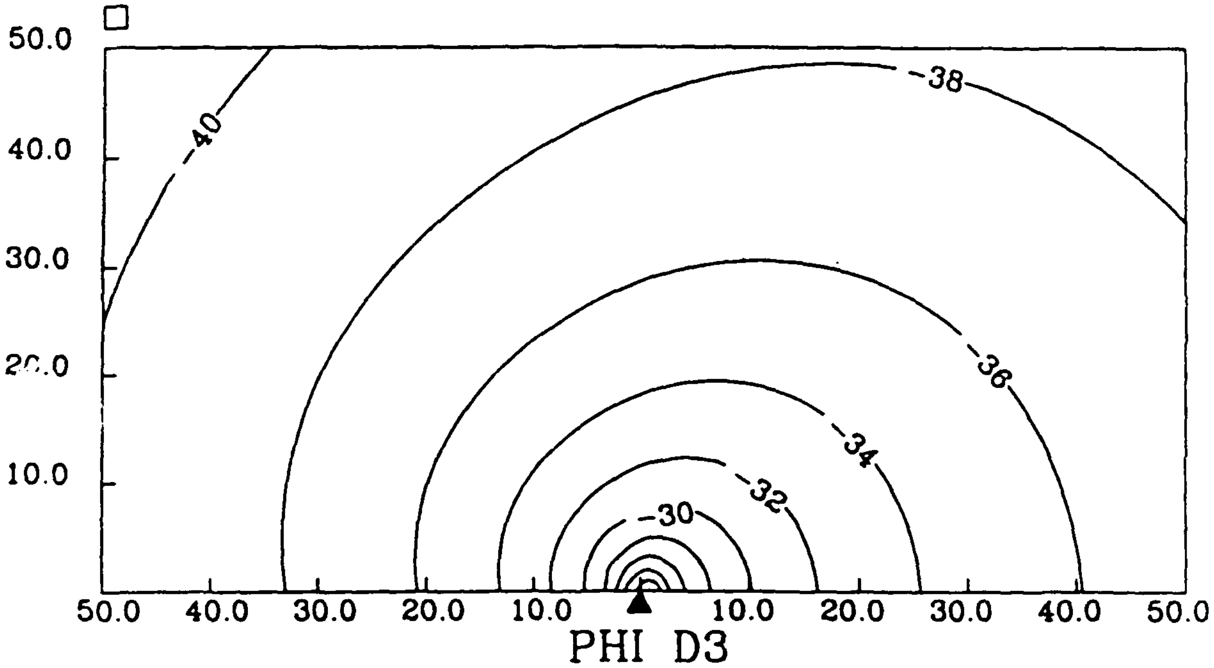

Figure 3.5: Contours of equal amplitude level for $\phi_{D3}(r,\theta)$ with $\alpha = 15^o$. The boundary discontinuity at the origin is marked by the triangle, with the free surface boundary on the left side and finite impedance surface on the right side. The distance from the origin is in units of $10 \cdot kr$. The contour levels are in dB referenced to a unit amplitude incident wave field.

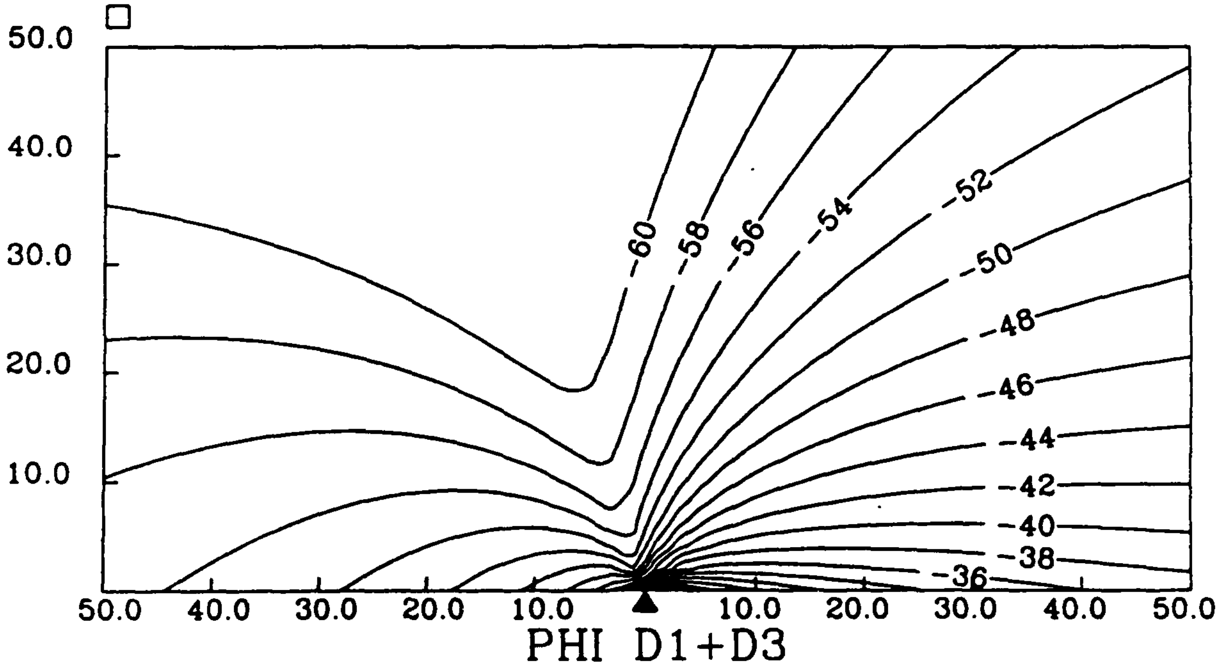

Figure 3.6: Contours of equal amplitude level for the coherent sum of $\phi_{D1}(r,\theta)$ and $\phi_{D3}(r,\theta)$ with $\alpha = 15^o$. The boundary discontinuity at the origin is marked by the triangle, with the free surface boundary on the left side and finite impedance surface on the right side. The distance from the origin is in units of $10 \cdot kr$. The contour levels are in dB referenced to a unit amplitude incident wave field.

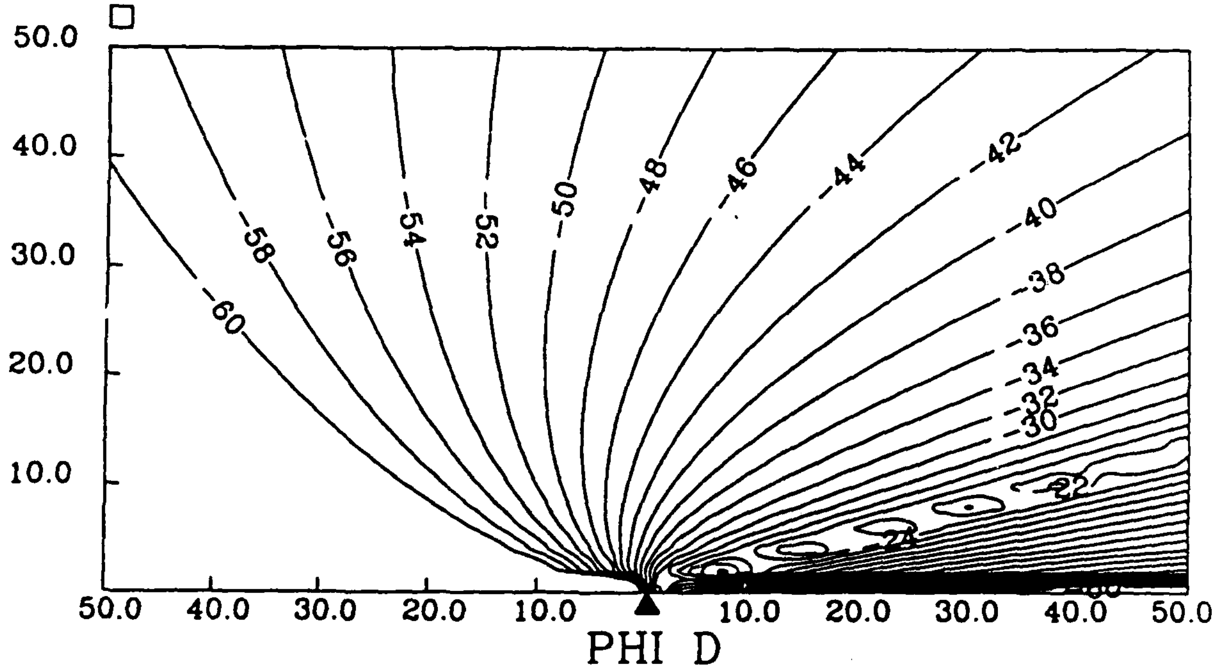

Figure 3.7: Contours of equal amplitude level for $\phi_D(r,\theta)$ with $\alpha = 15^o$. The boundary discontinuity at the origin is marked by the triangle, with the free surface boundary on the left side and finite impedance surface on the right side. The distance from the origin is in units of $10 \cdot kr$. The contour levels are in dB referenced to a unit amplitude incident wave field.

the integral representation of $\eta\phi_D(x,0)$ which is

$$\eta\phi_D(x,0) = \eta(1+R)e^{ikx\cos\alpha} \tag{3.41}$$

and the analogous residue field in the integral representation of $\frac{\partial\phi_D(x,0)}{\partial y}$ which is

$$\frac{\partial\phi_D(x,0)}{\partial y} = ik\sin\alpha(1+R)e^{ik\cdot\,\cos\alpha}. \tag{3.42}$$

Here R is assumed to be a function of α to simplify notation. Since the incident and free surface reflected fields cancel, the effective boundary condition for $\phi_D(x,0), x > 0$ is Eq.(3.17), which is satisfied by the geometric fields in Eqs.(3.41) and (3.42) upon using the identity

$$ik\sin\alpha(R-1) = \eta(R+1). \tag{3.43}$$

Thus, the geometric fields which arise from the residue contributions of ϕ_D balance separately.

Having satisfied Eq.(3.17) the equivalent boundary condition to be satisfied by the SDP fields is

$$\frac{\partial\phi_D(x,0)}{\partial y} = \eta\phi_D(x,0) \quad x > 0. \tag{3.44}$$

For $x > 0$, the coherent sum of $\phi_{D1}(x,0)$ and $\phi_{D3}(x,0)$ gives

$$\frac{(1+R)}{4\sqrt{\pi}}\frac{(1+i)}{\sin\frac{\alpha}{2}}\frac{e^{ikx}}{\sqrt{kx}} + O(\frac{1}{(kx)^{\frac{3}{2}}})$$

which is in exact anti-phase with $\phi_{D2}(x,0)$ as described by

$$\frac{(1+R)}{2}\;\mathcal{F}_A(r,\pi;\alpha).$$

Therefore the $O(\epsilon)$ behavior of ϕ_D vanishes along the $x > 0$ boundary with the leading order behavior being $O(\epsilon^3)$. Recovery of higher order terms in $\phi_D(x,0)$ is possible but not necessary because to strike an asymptotic balance between both sides of Eq.(3.44) merely requires that $\frac{\partial\phi_D(x,0)}{\partial y}$ also vanish to this same order. The normal derivative of the cylindrically radiating diffracted field is available from the integral representation

$$\frac{\partial\phi_D(x,0)}{\partial y} = -\int_{-\infty}^{\infty}\sqrt{q^2-k^2}G(q)e^{iqx}dq \tag{3.45}$$

and with $x > 0$ the integral contour will be a semi-circle in the upper half-plane with the net result coming from the branch line integration around the branch point of $\sqrt{q-k}$. The leading order behavior of this integral using the same contour as in Fig. 2.12 is $O(1/(kx)^{\frac{3}{2}})$ and we thus satisfy Eq.(3.44) to $O(\epsilon)$ with an error of $O(\epsilon^3)$.

We note that the boundary condition of Eq.(3.44) is exactly that which applies to the Karp-Karal lemma [18] from the theory of radiation from surface wave antennas. The Karp-Karal lemma states that the $O(\epsilon)$ behavior of a radiating or space wave field must vanish over a *finite* impedance surface. (One may view this as relating to "Lloyds mirror" effect [6]. We refer to the Karp-Karal lemma because it specifically addresses our impedance boundary condition.) In our diffraction problem the far field of ϕ_D (except within the transition region) is equivalent to a radiating cylindrical wave, and we found that ϕ_D vanished along the finite impedance boundary at the $O(\epsilon)$ level in agreement with the Karp-Karal lemma. This is in contrast with the results of Chapter 2, where the leading order behavior of ϕ_D was found to be $O(\epsilon)$ along the *infinite* impedance boundary. The main point of the Karp-Karal lemma as applied to this diffraction problem is that, for a finite impedance boundary the diffracted intensity decays as $1/(kx)^3$ along the boundary, while for an infinite impedance boundary the diffracted intensity decays as $1/(kx)^2$. This fact will be used later in Chapter 5 when we apply these results to boundaries of some finite characteristic length.

3.5 Analysis of errors originating from use of the approximate kernel

We have used an approximate kernel $\hat{K}(q)$ which sufficiently duplicated the behavior of $K(q)$ and, most importantly, could be decomposed into $\hat{K}_-(q)$ and $\hat{K}_+(q)$. The decomposed factor $\hat{K}_-(q)$ became part of the diffracted field plane wave spectrum. But $\hat{K}_-(q)$ also has three singularities which are due to the approximating procedure. These spurious singularities must be accounted for if they are crossed when deforming the contour in the SDP analysis, and we need to show that their contributions are negligible. Specifically, the factors $(q-i\sqrt{k^2+\eta^2})$ and $(q-kA_1)$ (as defined in Appendix B) yield residue contributions for $x > 0$. Since $i\sqrt{k^2+\eta^2}$ is imaginary and kA_1 is complex with positive imaginary part, the residue fields are exponentially damped in range x. These have been evaluated and, at their maximum value near the origin, are approximately 50 dB less than the other terms in ϕ_D.

The factor $\sqrt{q - kn}$ with n a positive integer (as defined in Appendix B) introduces a spurious branch line integral around the branch point $q = ikn$. This can be evaluated asymptotically with the behavior of the leading order term being $O(e^{-xkn}/(kx)^{\frac{3}{2}})$. Thus, even if had reported terms of $O(1/(kx)^{\frac{3}{2}})$ in $\phi_D(x,0)$, Eq.(3.44) would not balance exactly to this order. Here lies the distinction between the use of the approximate kernel in this solution, and the exact solution of the canonical problem. In the canonical problem solution, satisfying the boundary condition to $O(\epsilon)$ was only a result of the mathematical difficulties in inverting the integral; otherwise the solution is exact. With this solution, higher order terms are in error because of the approximate kernel.

But we can say with confidence that the solution dependent upon the approximate kernel satisfies the field equation exactly, as seen by the original integral representation of $\phi_D(x,y)$ in Eq.(2.9), and satisfies the boundary conditions along the planar boundary $y = 0$ to $O(\epsilon)$, as well as the radiation condition. The field equation is the reduced wave equation or Helmholtz equation. This is an elliptic type partial differential equation (PDE) [36]. One property of an elliptic PDE is that a field solution is a unique one if it satisfies the appropriate specified boundary conditions [37]; furthermore, if the boundary conditions are satsified to $O(\epsilon)$ the field solution is correct to $O(\epsilon)$ [63]. That is, for an elliptic PDE, higher order errors in satisfying the boundary condition will not propagate into the field solution. By satisfying the boundary conditions to a sufficient degree of accuracy, we justify use of the approximate kernel. A field solution correct to $O(\epsilon)$ is discussed in the next section in the context of energy conservation.

3.6 Power balance of incident, reflected and diffracted fields

In this section we demonstrate that the total field, being the coherent sum of incident, reflected and diffracted fields, satisfies a power balance governed by the homogeneous Helmholtz equation. Because the fields are in steady state with harmonic time depen-

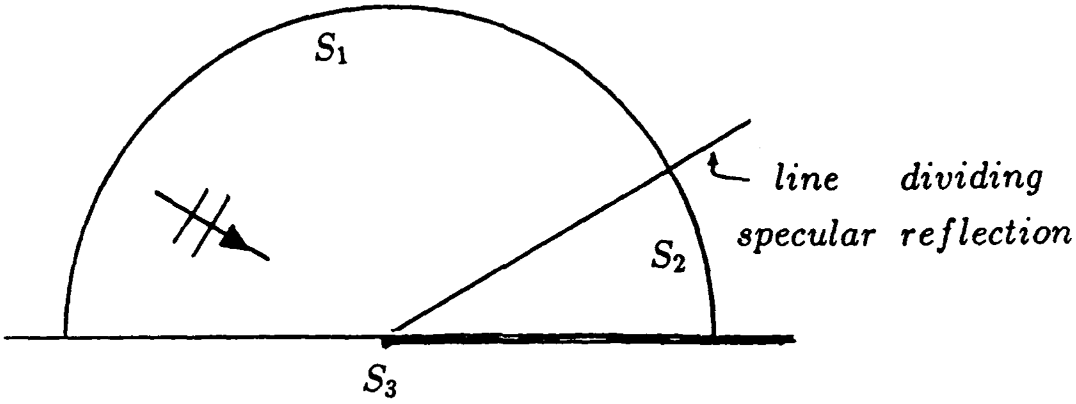

Figure 3.8: Control surface S for determining power balance composed of sections S_1, S_2 and S_3.

dence, the energy flowing through the boundaries of an arbitrary closed surface per unit time must be balanced by the total power supplied by sources within the closed surface. Since there are no sound sources in this problem, we must necessarily have

$$\int_S \langle \vec{I} \rangle \cdot dS = \int_0^\pi \langle \vec{I} \rangle r d\theta = 0. \tag{3.46}$$

Here, $\langle \vec{I} \rangle$ is the intensity or Poynting vector, representing energy per unit area per unit time [37], and S is the closed control surface in Fig. 3.8. The power is derived by integrating $\langle \vec{I} \rangle$ over the area S, and in the context of our two-dimensional geometry which is independent of the z-coordinate, we interpret the result as power per unit length parallel to the z-axis.

In the process of computing the intensity we will encounter different orders of intensity radial dependence such as $O(\epsilon^0)$, $O(\epsilon^1)$ and $O(\epsilon^2)$, with $\epsilon = 1/\sqrt{kr}$. For example, plane wave intensity radial dependence is $O(\epsilon^0)$, and cylindrical wave intensity radial dependence is $O(\epsilon^2)$. Because $dS = rd\theta$ we have the situation where $O(\epsilon^0)$ and $O(\epsilon^1)$ intensity contributions increase without bound when integrated from 0 to π for increasing cylindrical radius. Thus these orders must be appropriately balanced. Furthermore the $O(\epsilon^2)$ intensity contribution gives an integrated value independent of cylindrical radius, and higher orders of intensity radial dependence may be ignored.

The control surface S represents an infinite closed half cylinder (extending in and out of the page). The cylindrical section of the surface is divided into two sectors S_1 and S_2, separated by the line dividing specular reflection; the planar section of the surface is represented by S_3. Within each sector the reflection coefficient is R_i $i = 1, 2$; for example, on the left planar boundary in Fig. 3.8 R_1 equals -1 corresponding to the free surface, and on the right planar boundary R_2 equals the reflection coefficient corresponding to a locally reacting surface evaluated at grazing angle α. For each case $|R_i| = 1$ and ϕ_T satisfies the mixed boundary conditions, thus there is no energy flux through the planar surface S_3, and the problem reduces to determining the flux through the cylindrical surface $S_1 + S_2$.

The total velocity potential field is

$$\phi_T(r,\theta) = e^{ikr\cos(\theta-\alpha)} + R_i e^{-ikr\cos(\theta+\alpha)} + \phi_D(r,\theta) \quad i = 1,2 \tag{3.47}$$

where the residue contribution of ϕ_D is assumed to be included in the reflected fields. The time-averaged complex intensity vector is given by [8]

$$\langle \vec{I} \rangle = \frac{i\omega\rho_0}{4}(\phi_T \nabla \phi_T^* - \phi_T^* \nabla \phi_T) \tag{3.48}$$

where the real part of $\langle \vec{I} \rangle$, or active intensity [62], represents the radiating part of the energy flux which is used for the power computation in Eq.(3.46). The imaginary part of $\langle \vec{I} \rangle$, or reactive intensity, represents non-propagating near-field energy where the acoustic pressure and particle velocity are out of phase, and it has no net effect on the transfer of time-averaged energy through the closed surface S [50] The first step in the computation gives

$$\begin{aligned} \phi_T \nabla \phi_T^* - \phi_T^* \nabla \phi_T &= [2ik(\cos(\theta-\alpha) + \cos(\theta+\alpha))] \\ &- [2\sum_{n=1}^{6} Im(\psi_n)] + [\phi_D \nabla \phi_D^* - \phi_D^* \nabla \phi_D] \end{aligned} \tag{3.49}$$

with

$$\psi_1 = -ik\cos(\theta+\alpha) R_i e^{ikr2\sin\theta\sin\alpha}$$

$$\begin{aligned}
\psi_2 &= -ik\cos(\theta-\alpha)R_i^* e^{-ikr2\sin\theta\sin\alpha} \\
\psi_3 &= \nabla\phi_D e^{ikr\cos(\theta-\alpha)} \\
\psi_4 &= \nabla\phi_D R_i^* e^{ikr\cos(\theta+\alpha)} \\
\psi_5 &= -ik\phi_D^*\cos(\theta-\alpha)e^{-ikr\cos(\theta-\alpha)} \\
\psi_6 &= -ik\phi_D^*\cos(\theta+\alpha)R_i e^{-ikr\cos(\theta+\alpha)}.
\end{aligned}$$

The first bracketed term represents the incident and specularly reflected fields and integrating these from 0 to π gives zero net power. The second bracketed term includes all of the coupled terms of the intensity vector, of which ψ_1 and ψ_2 represent coupling between incident and reflected fields. For these terms consider the following integral:

$$I_1(r) = \int_0^\pi (\psi_1 + \psi_2) r d\theta. \tag{3.50}$$

This integral can be evaluated for an arbitrarily large cylindrical radius by stationary phase in spite of the fact that R_i changes from -1 to R in a step-wise manner across the region of integration, since this does not effect convergence properties of the integral [7]. The stationary point (θ_s) for both terms is $\theta_s = \pi/2$ and the result from the first term for $kr \gg 1$ is

$$ik\cos(\frac{\pi}{2}+\alpha)R_1 e^{2ikr\sin\alpha - i\frac{\pi}{4}}\sqrt{\frac{\pi}{2kr}}$$

which happens to be the conjugate of the result of integrating the second term and therefore $I_1(r)$ is a real quantity at the $O(\epsilon)$ level. This implies that the imaginary parts as prescribed by Eq.(3.49) vanish at the $O(\epsilon)$ level which means $\langle\vec{I}\rangle$ is also imaginary and there is no active intensity. The next order in the asymptotic evaluation is $O(\epsilon^3)$ which we will not concern ourselves with since it vanishes with expanding cylindrical radius.

Next we examine the coupled terms denoted by ψ_3 and ψ_5, which represent coupling between incident and diffracted fields, by evaluating the following integral using stationary phase:

$$I_2(r) = \int_0^\pi (\psi_3 + \psi_5) r d\theta. \tag{3.51}$$

Both terms of the integrand are continuous functions of θ with the stationary point at $\theta_s = \alpha$. Because the stationary point is away from the transition sector near $\pi - \alpha$, the Fresnel integral part of ϕ_D is well approximated by its cylindrically spreading asymptotic form, and thus we can use

$$\nabla \phi_D(r, \alpha) = ik\phi_D(r, \alpha). \tag{3.52}$$

The result of integrating the first term is

$$ik\phi_D(r, \alpha)e^{ikr - i\frac{\pi}{4}}\sqrt{\frac{\pi}{2kr}}$$

which is also the conjugate of the result of integrating the second term, and like the previous example the imaginary parts vanish to this order, which in this case is $O(\epsilon^2)$ because $\phi_D(r, \alpha)$ is already of $O(\epsilon)$. This demonstrates that there is no coupling between the incident and diffracted fields.

Finally, ψ_4 and ψ_6, which represent coupling between the reflected and diffracted fields, must be shown to balance in the appropriate manner. But in this case the surface integral has a stationary phase point at $\theta_s = \pi - \alpha$, or the exact center of the transition region. Stationary phase methods will not work here because the Fresnel integral part of ϕ_D is rapidly varying in the transition region. To proceed, we divide the integration range from 0 to π into three regions including the transition region

$$I_3(r) = \int_0^{\pi - \alpha - \Delta} + \int_{\pi - \alpha + \Delta}^{\pi} + \int_{2\Delta} (\psi_4 + \psi_6) r\, d\theta \tag{3.53}$$

where the last integral is over the transition region and Δ is some small angular increment. From Eq. (2.46) and using the small angle approximation, we see that

$$\Delta \simeq \frac{3.55}{\sqrt{2kr}}. \tag{3.54}$$

For now, we assume Δ is sufficiently large enough such that the first two integrals are *outside* the transition region and all component fields of ϕ_D are cylindrically spreading, i.e., $\mathcal{F}(r, \theta; \alpha) = \mathcal{F}_A(r, \theta; \alpha)$ for the ϕ_{D2} component field. Because the first two integrals are outside the transition region, there is no stationary point and the asymptotic method which now applies is integration by parts [7]. Thus, for example, we have

$$\int_0^{\pi - \alpha - \Delta} \psi_4 r\, d\theta \sim \frac{-\phi_D(r, \theta) R_i^*}{r \sin(\theta + \alpha)} e^{ikr\cos(\theta + \alpha)} \Bigg|_0^{\pi - \alpha - \Delta} \tag{3.55}$$

The method of integration by parts is not valid if we come too close to the line dividing specular reflection at $\theta = \pi - \alpha$. But with sufficiently large Δ this is not a problem, and the net asymptotic evaluation of the first two integrals in Eq.(3.53) is $O(\epsilon^3)$.

We can get an idea of the intensity radial dependence and subsequent power balance within the transition region by examining the behavior of the intensity vector on both sides of the line dividing specular reflection at $\theta = \pi - \alpha$, or the exact center of the transition region. Precisely along this line, the cylindrically spreading component fields ϕ_{D1} and ϕ_{D3} vanish and the diffracted field is governed entirely by the Fresnel integral functional form. Using the properties of $\mathcal{F}(r, \theta; \alpha)$ presented in Chapter 2, and setting $R_1 = -1$ and $R_2 = R$ for clarity, we have

$$\begin{aligned} \psi_4 &\sim -ik(\frac{R+1}{2})e^{ikr(1+\cos(\pi-\delta))} \\ \psi_6 &\sim ik(\frac{R^*+1}{2})\cos(\pi-\delta)e^{-ikr(1+\cos(\pi-\delta))} \end{aligned} \tag{3.56}$$

on the $\theta = \pi - \alpha - \delta$ side of the line, and

$$\begin{aligned} \psi_4 &\sim -ik(\frac{R+1}{2})R^* e^{ikr(1+\cos(\pi+\delta)} \\ \psi_6 &\sim ik(\frac{R^*+1}{2})\cos(\theta+\delta)Re^{-ikr(1+\cos(\pi+\delta)} \end{aligned} \tag{3.57}$$

on the $\theta = \pi - \alpha + \delta$ side of the line. In the limit of vanishingly small δ, the integral over this incremental area is

$$\int_{\pi-\alpha-\delta}^{\pi-\alpha+\delta} (\psi_4 + \psi_6) r d\theta = -2ik(Real(R) + 1) \;\; dS \tag{3.58}$$

where the incremental area $dS = 2r\delta$. Upon using Eq.(3.48) the value of the coupled intensity vector across this incremental area is

$$\langle \vec{I} \rangle_{4,6} = -\omega\rho_0 k(Real(R) + 1) \tag{3.59}$$

We note that this intensity vector is real across the incremental area, and is of $O(\epsilon^0)$ or of plane wave-like radial dependence.

So far we have computed the equivalent intensity vector for the first two bracketed terms in Eq.(3.49), and have carried out the integration prescribed in Eq.(3.46) for an arbitrarily large cylindrical radius. With the exception of the transition region of angular width 2Δ, the results derived asymptotically for $kr \gg 1$ showed that the orders of intensity radial dependence to be appropriately balanced when integrated. In other words, we found no left over $O(\epsilon^0)$ or $O(\epsilon^1)$ intensity radial dependence. Within the transition region the power remains unbalanced, however, with the intensity radial dependence being $O(\epsilon^0)$ in the exact center of this region.

We have yet to examine the intensity vector due to the purely diffracted field described by the last bracketed term in Eq.(3.49). Inside the transition region the diffracted field will also be rapidly varying and so will be examined in the same manner. Specifically,

$$\phi_D \nabla \phi_D^* - \phi_D^* \nabla \phi_D \sim -ik(Real(R) + 1) \tag{3.60}$$

on either side of the line dividing specular reflection. Thus in the limit of vanishingly small δ the total diffracted power transferred across this same incremental area is

$$\frac{i\omega\rho_0}{4} \int_{\pi-\alpha-\delta}^{\pi-\alpha+\delta} (\phi_D \nabla \phi_D^* - \phi_D^* \nabla \phi_D) r d\theta = .5 \;\; \omega\rho_0 k(Real(R) + 1) \;\; dS \tag{3.61}$$

with the diffracted intensity vector across this incremental area being

$$\langle \vec{I} \rangle_D = .5\omega\rho_0 k(Real(R) + 1). \tag{3.62}$$

The intensity vector due to the diffracted field is of the same order as that found for the combination of coupled fields ψ_4 and ψ_6 [Eq.(3.59)], but is half the value and points in the opposite direction. The power is not balanced exactly since we have only looked at one incremental element of the rapidly varying transition region. Entering the next incremental element will give another relation between the coupled and diffracted intensity vectors; a relation which is not simple because the diffracted field behavior is now tied to the complex error function as discussed in Chapter 2. Nevertheless, if we plot the intensity vector corresponding to the purely diffracted field and the intensity vector corresponding to the combination of coupled fields ψ_4 and ψ_6 (Fig. 3.9), we observe that the areas under the two curves cancel (this has been confirmed by numerical integration with the two integrals cancelling within a fraction of a percent). Figure 3.9 also confirms our arguments leading to Eqs.(3.59) and (3.62). Since the two integrals represented by the figure cancel, the power transferred within the transition region is also balanced.

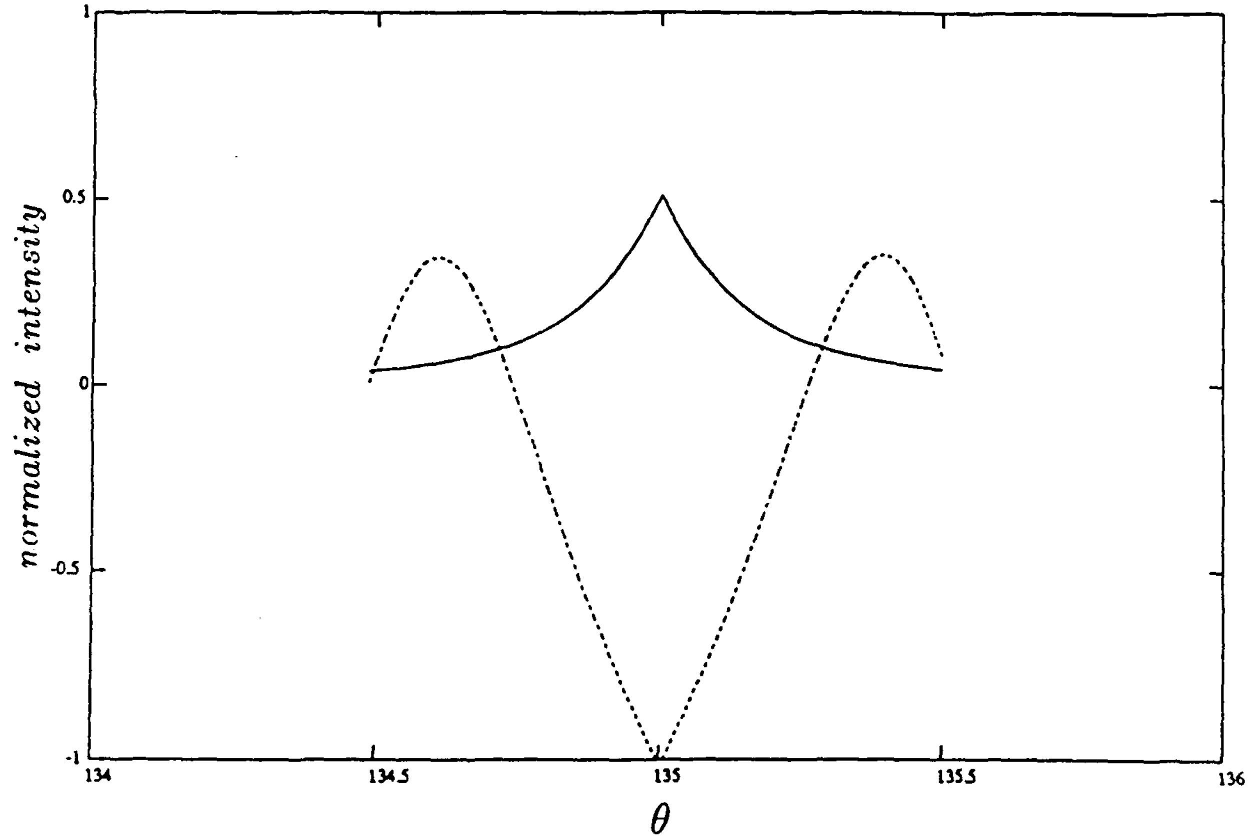

Figure 3.9: Behavior of coupled intensity vector $\langle\vec{I}\rangle_{4,6}$ (dashed line) and diffracted intensity vector $\langle\vec{I}\rangle_D$ (solid line) within the transition region with the intensity values normalized for clarity. The example is from the canonical diffraction problem where $R_1 = -1$, $R_2 = 1$ and $\alpha = 35^o$, with $kr = 100,000$ which sets the transition range angular width to be $\approx 1^o$, centered at the specular field angle $\theta = 135^o$.

Now the entire 0 to π integration range over the cylindrical surface has been balanced in terms of integrated intensity. But this balance was achieved without regard to the contribution of the diffracted field ***outside*** the transition region. Outside the transition region the diffracted field is cylindrically spreading and the net integrated intensity or power will be independent of cylindrical radius. Let us call the power contribution from this integration Π_D. But the original conservation law as expressed by Eq.(3.46) must still hold. Therefore we attribute the value of Π_D to an equivalent reduction in the specularly reflected radiated power Π_R, such that the overall power balance becomes

$$\Pi_I = \Pi_R + \Pi_D \tag{3.63}$$

where Π_I is the incident power and Π_R is the now reduced specularly reflected power.

There remains one final practical matter regarding the computation of Π_D. Since the power computation is outside the transition region we define formally that

$$\Pi_D = \int_0^{\pi-\alpha-\Delta} + \int_{\pi-\alpha+\Delta}^{\pi} \langle \vec{I_D} \rangle r d\theta \tag{3.64}$$

where $\langle \vec{I_D} \rangle$ is the diffracted intensity computed from ϕ_D, and we employ the asymptotic evaluation $\mathcal{F}(r,\theta;\alpha)$ for the ϕ_{D2} component field, which is valid outside the transition region. But the transition region angular width 2Δ decreases with $1/\sqrt{kr}$, and in this sense our intensity integration *does* depend on cylindrical radius. This kr-dependence can be thought of as due to power contributions from coupled terms which have not decayed sufficiently for their influence on Π_D to be negligible. Recall though, that we have already demonstrated analytically, in the asymptotic $kr \to \infty$ limit, that the coupled power contributions will either vanish, or be exactly balanced as is the case within the transition region, and thus do not contribute to the net power.

The progressive decay of the coupled terms is shown in the following four plots which give the far field amplitude level of $|\phi_D(r,\theta)|^2$. The solid line uses the exact evaluation of $\mathcal{F}(r,\theta;\alpha)$ for the $\phi_{D2}(r,\theta)$ component field, and the dashed line uses the asymptotic evaluation $\mathcal{F}_A(r,\theta;\alpha)$ [Eq.(2.45)] which has cylindrical spreading. Each plot has a 40 dB range, with the 0 dB point referenced to the maximum value of the diffracted field which is $|\frac{R(\alpha)+1}{2}|$ and always occurs along the line dividing specular reflection. Two examples of the locally reacting ice boundary condition are given with $H = 2$ m , $\rho_2 = .92$ and frequency of 50 Hz. In the first (Fig. 3.10) $\alpha = 15^o$ giving

$$20 \log |\frac{1+R}{2}| = -19.71 \tag{3.65}$$

in dB which is considered the 0 db point; in the second (Fig. 3.11) $\alpha = 45^o$ and therefore -12 dB is considered the 0 dB point. The third and fourth examples (Figs. 3.12 and 3.13) are from the canonical problem; here the maximum value will always be 0 dB because R is unity for all α. For increasing kr the asymptotic evaluation merges with the exact evaluation. For example, at kr = 10,000 the two evaluations are the same except within the approximately 2^o transition region.

The merging of the two evaluations indicate that the coupled terms have decayed sufficiently via destructive interference, such that a good measure of Π_D is available by integrating the cylindrically spreading diffracted field which depends on use of the asymptotic form $\mathcal{F}_A(r, \theta; \alpha)$. The integration is made up to, but not including the transition region. The transition region and the cylindrically spreading region outside (or slowly varying shadow region), are analogous to the Fresnel and Fraunhofer far field diffraction regions in acoustic scattering from finite objects [58]. Thus, the integration range expressed in Eq.(3.64) is equivalent to integrating over the Fraunhofer far field region, and we will carry out this integration at sufficiently large kr such that the Fraunhofer far field region encompasses all but approximately 1^o of angular space. The integral is evaluated numerically using Simpson's rule; convergence issues and numerical error do not pose a problem because the integrand is smoothly varying. The result Π_D is interpreted as the amount of power removed from the specularly reflected field.

Some representative values of Π_D are shown in Fig. 3.14. Included for comparison are the equivalent values for total diffracted power from a free surface coupled to a perfectly rigid surface, or the infinite impedance case, as worked out in Chapter 2. The values are presented in terms of $10 \log \Pi_D$ in dB, referenced to the maximum power level which occurs for the infinite impedance case at 1 Hz in these examples. (Note that Π_D does not depend on grazing angle α for the infinite impedance case.) There are some evident trends, for example, a linear dependence of Π_D on frequency for the finite impedance surface. These

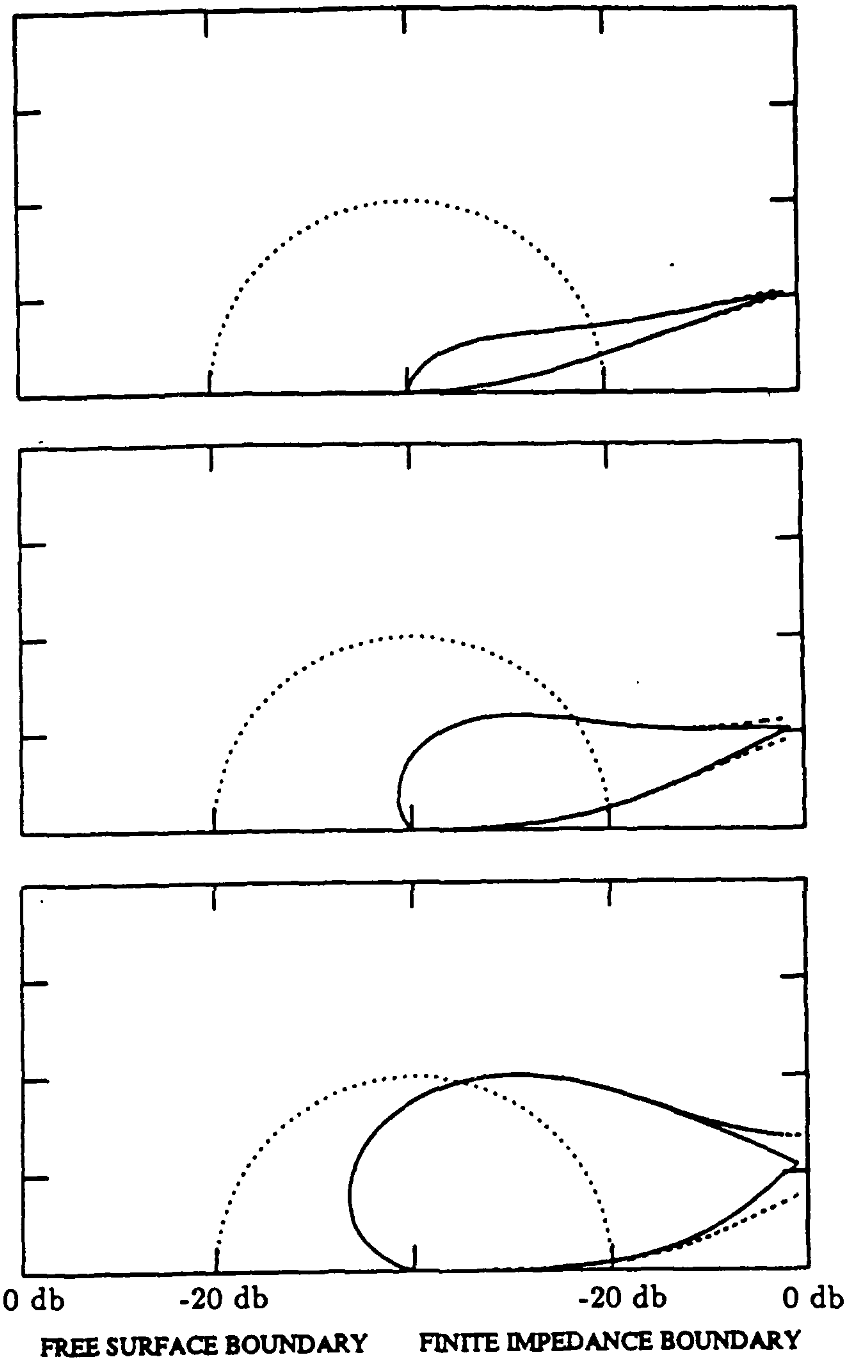

Figure 3.10: Far field amplitude level of $|\phi_D(r,\theta)|^2$ for $\alpha = 15^o$, and locally reacting boundary condititon, at fixed kr. bottom: $kr = 100$, middle: $kr = 1000$, top: $kr = 10000$. Solid line uses exact evaluation of $\mathcal{F}(r,\theta;\alpha)$, dashed line uses asymptotic evaluation $\mathcal{F}_A(r,\theta;\alpha)$. Dotted semi-circle represents the 20 dB down point from the maximum level.

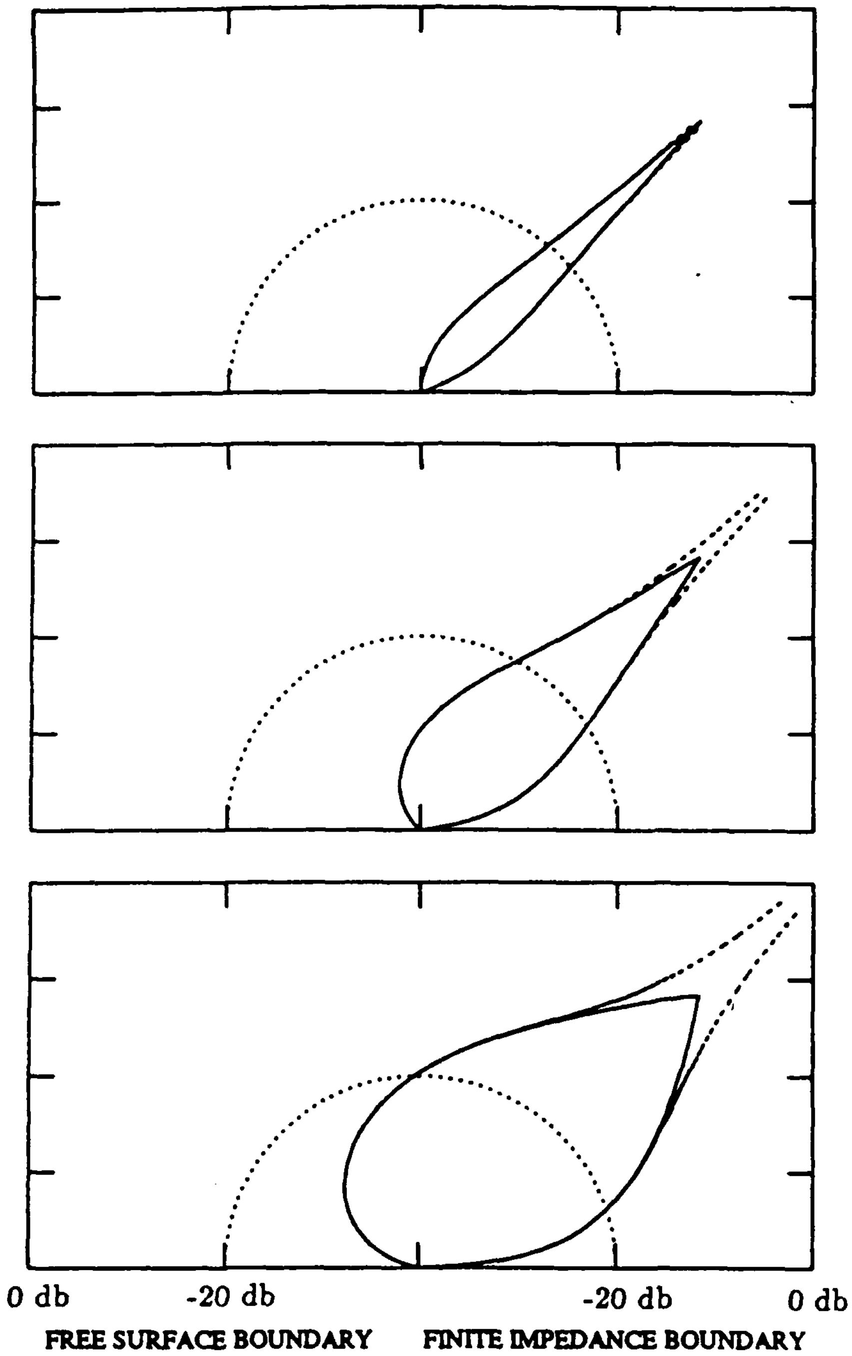

Figure 3.11: Far field amplitude level of $|\phi_D(r,\theta)|^2$ for $\alpha = 45^\circ$, and locally reacting boundary condititon, at fixed kr. bottom: $kr = 100$, middle: $kr = 1000$, top: $kr = 10000$. Solid line uses exact evaluation of $\mathcal{F}(r,\theta;\alpha)$, dashed line uses asymptotic evaluation $\mathcal{F}_A(r,\theta;\alpha)$. Dotted semi-circle represents the 20 dB down point from the maximum level.

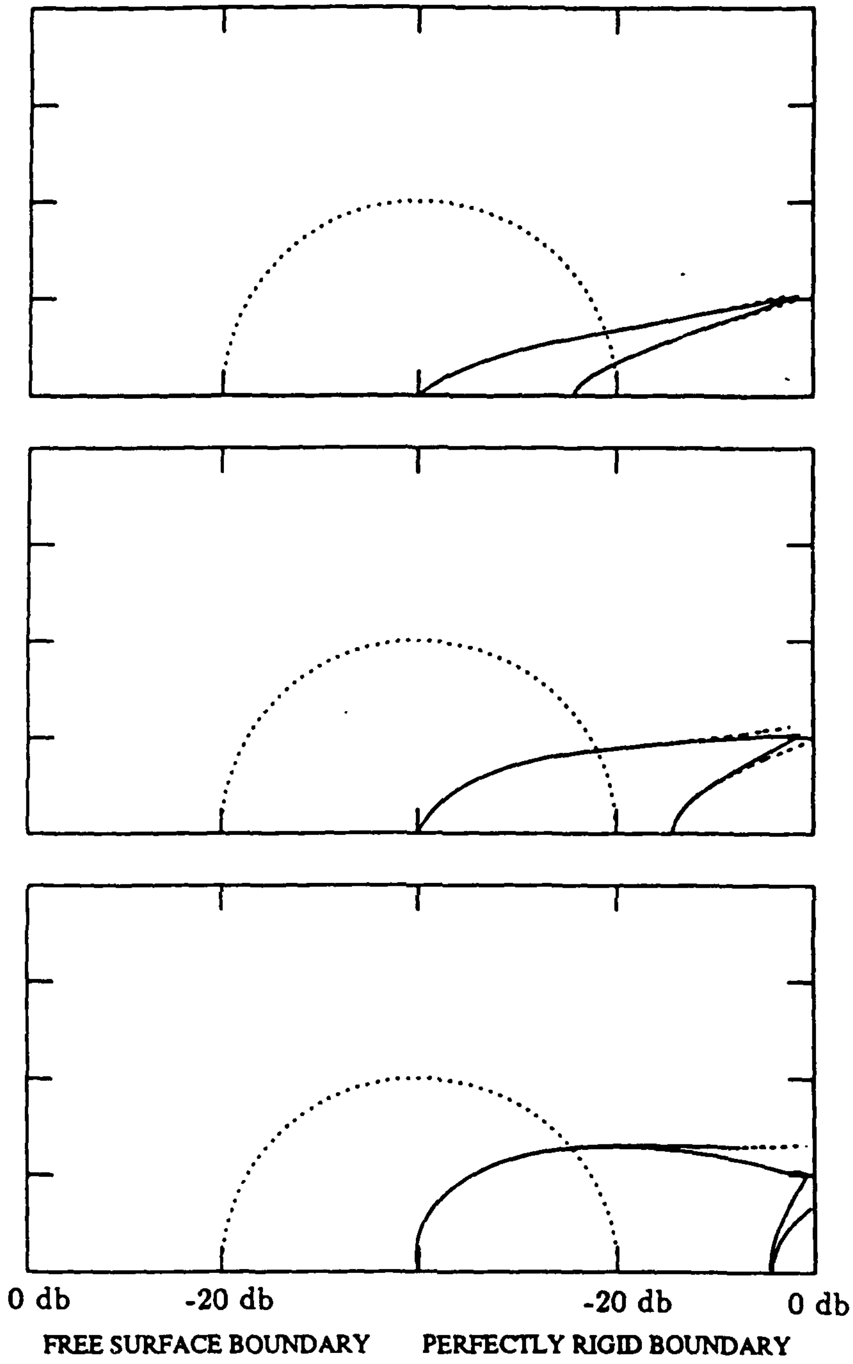

Figure 3.12: Far field amplitude level of $|\phi_D(r,\theta)|^2$ from the canonical problem for $\alpha = 15°$, at fixed kr. bottom: $kr = 100$, middle: $kr = 1000$, top: $kr = 10000$. Solid line uses exact evaluation of $\mathcal{F}(r,\theta;\alpha)$, dashed line uses asymptotic evaluation $\mathcal{F}_A(r,\theta;\alpha)$. Dotted semi-circle represents the 20 dB down point from the maximum level.

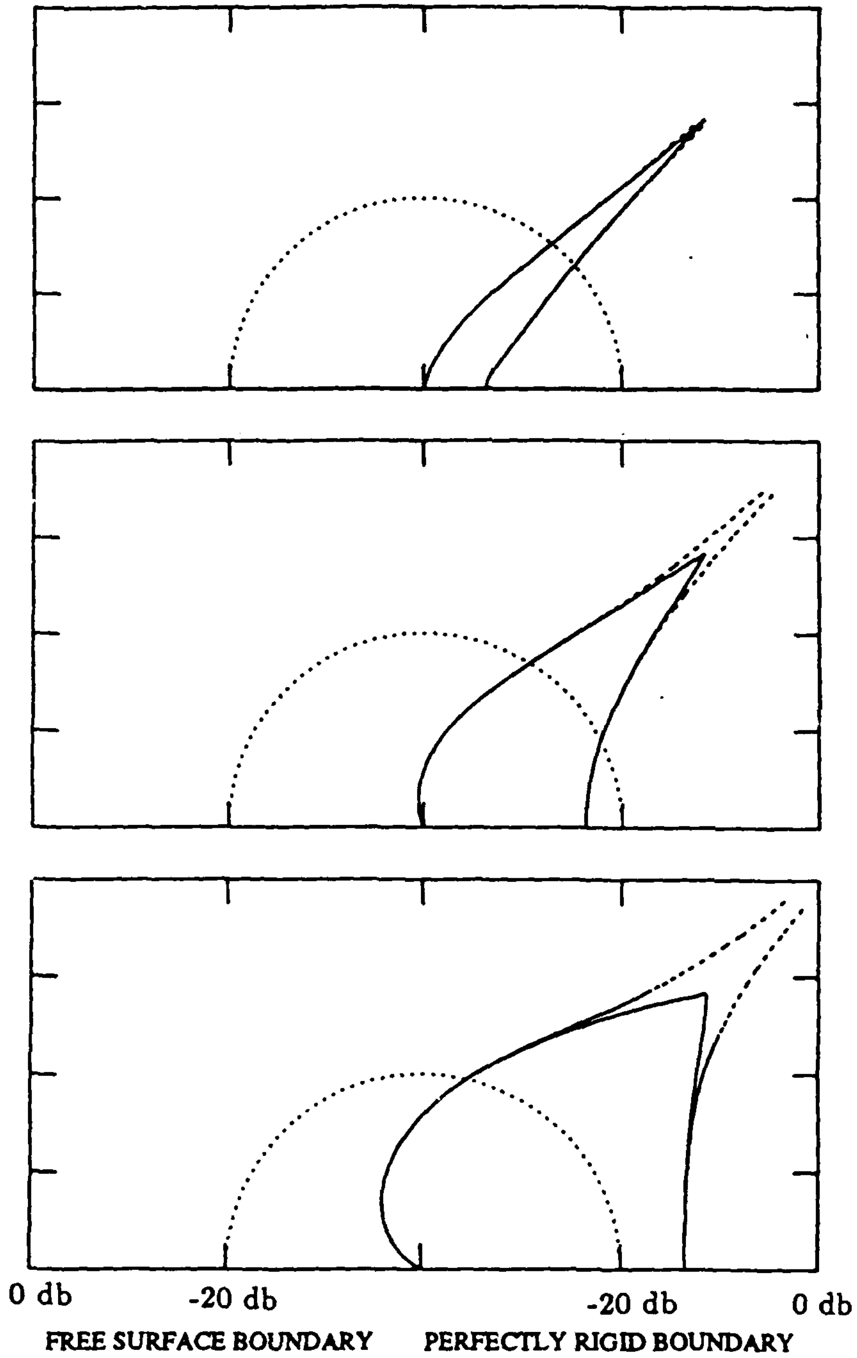

Figure 3.13: Far field amplitude level of $|\phi_D(r,\theta)|^2$ from the canonical problem for $\alpha = 45^\circ$, at fixed kr. bottom: $kr = 100$, middle $kr = 1000$, top: $kr = 10000$. Solid line uses exact evaluation of $\mathcal{F}(r,\theta;\alpha)$, dashed line uses asymptotic evaluation $\mathcal{F}_A(r,\theta;\alpha)$. Dotted semi-circle represents the 20 dB down point from the maximum level.

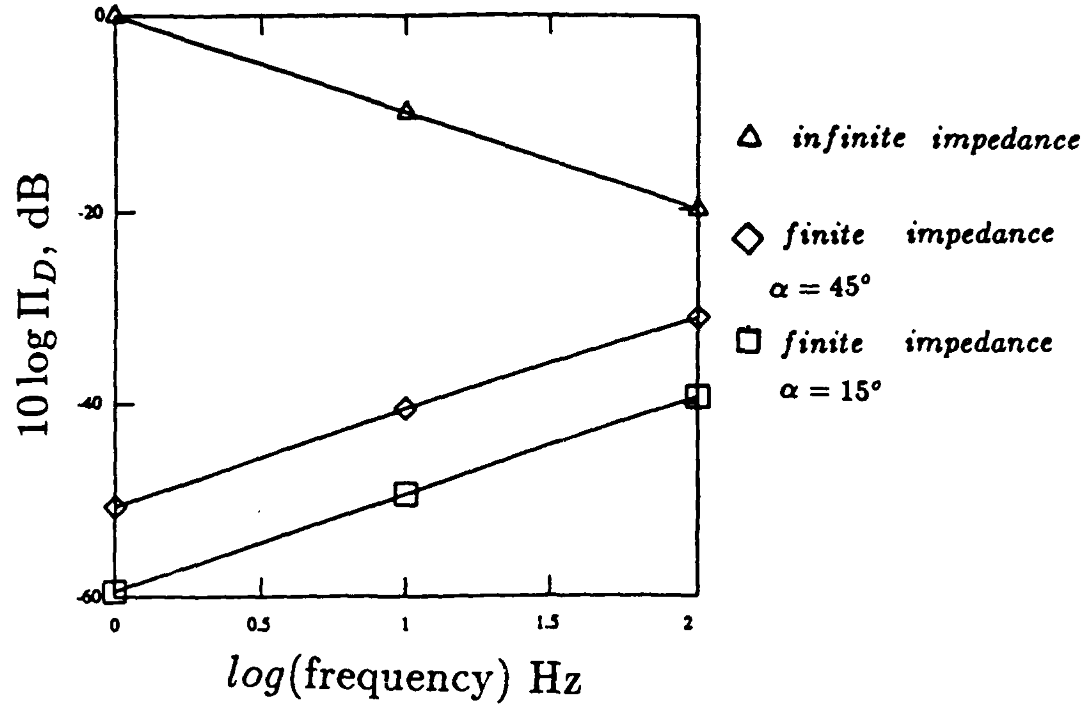

Figure 3.14: Values of $10\log\Pi_D$ in dB for 1, 10 and 100 Hz with $H = 1$m. The dB levels are referenced to the infinite impedance case at 1 Hz (0 dB).

are discussed in greater detail in Chapter 4, where we present a more complete analysis of Π_D in terms of varying ice and acoustic parameters.

The curious fact that Π_D increases with frequency in the finite impedance case and decreases with frequency in the infinite impedance (canonical problem) case, has a simple explanation. For the infinite impedance case, R is unity for all grazing angles and frequencies. Therefore the far field amplitude levels presented in this chapter and the contour plots presented in Chapter 2 are independent of frequency; a plot at $kr = 1000$ looks the same whether the incident wave is 10 Hz or 1000 Hz. Thus, for example, if the diffracted pressure field is proportional to $F(\theta)\frac{e^{ikr}}{\sqrt{kr}}$ then the relation for diffracted power is

$$\Pi_D \propto \frac{1}{k}\int_0^\pi |F(\theta)|^2 d\theta \tag{3.66}$$

and in the limit of $k \to \infty$, Π_D must approach zero in accordance with geometric optics.

On the other hand, for the case of finite, locally reacting impedance, R is a function of both grazing angle and frequency. Since $Z_{in} = -i\omega\rho_1 H$, the ice appears 'harder' with increasing frequency, and presents a sharper contrast with the free surface from which to launch a diffracted field. But we cannot, of course, continue this analysis with ever increasing frequency for the ice model because we run into issues of a non-locally reacting impedance and double diffraction [53]. (The latter is due to the scatter from the bottom edge and rescatter from the nearby top edge of a plate of thickness H.) If we could continue the analysis with increasing frequency, for example, by assuming the surface consists of a thin film with locally reacting surface impedance independent of frequency, the total diffracted power would eventually vanish as $k \rightarrow \infty$ in accordance with geometric optics.

3.7 Summary

We began this chapter with arguments for using a locally reacting boundary condition pertaining to a layer of sea ice and low-frequency acoustics. In this formulation, we ignore the part of the ice input impedance due to flexural rigidity, and as a consequence features of elastics wave propagation such as the flexural wave are ignored in computing the diffracted field. Using this boundary condition a coupled half-plane diffraction problem was solved, which serves as a model for the ice lead diffraction process. The solution used an approximate kernel in the Wiener-Hopf functional equation, which allowed us to proceed to a complete and interpretable solution. The solution is expressed in terms of the canonical angular spectrum $P(\beta)$ which is independent of any material properties, being multiplied by the material function $M(\beta)$. The material function is derived from multiplicative decomposition of the approximate kernel.

The solution satisfies the field equation exactly and the mixed boundary conditons to $O(\epsilon)$, and thus the field solution is correct to $O(\epsilon)$ with an error of $O(\epsilon^3)$. A power balance for the total field was demonstrated, with the total field being the coherent sum of incident, reflected and diffracted fields. This balance confirmed the interpretation that the diffracted field power Π_D, modified reflected field power Π_R, and incident field power Π_I, must sum to zero, and thus Π_D is the amount of power removed from the reflected field.

In the next chapter we compare this solution based on the locally reacting impedance approximation to one that includes the effects of elasticity in the ice.

Chapter 4

Diffraction problem with extended reaction boundary condition

The results of Chapter 2 gave the exact solution of a plane wave incident upon two coupled half-planes, one characterized by the Dirichlet or free surface boundary condition, equivalent to a surface with zero input impedance, the other characterized by the Neumann boundary condition, equivalent to a surface with infinite input impedance. In Chapter 3 the infinite impedance was replaced by a finite, locally reacting impedance of the form $Z_{in} = -i\omega\rho_1 H$. This was shown to be a good approximation to the ice input impedance for frequencies low enough such that the interior fields in the ice could be ignored. The infinite impedance corresponds to a perfectly rigid surface and the finite impedance corresponds to a surface which responds to local pressure, but with an impedance due only to an inertial term. In both cases the impedance is independent of the spatial distribution of the incident pressure field, which is equivalent to Z_{in} being independent of horizontal wavenumber.

This chapter now extends the solution to the case where it is possible for the ice input impedance to be a function of both horizontal wavenumber q and frequency ω

$$Z_{in} = Z_{in}(q, \omega). \tag{4.1}$$

The additional dependence of Z_{in} on the horizontal wavenumber is known as extended reaction [57]. Extended reaction in our problem is a result of including the elastic properties of ice in the calculation of Z_{in}. Thus, in this chapter we derive a complete solution of a plane wave incident upon a semi-infinite elastic plate, which, unlike the case of local reaction, incorporates elements of elastic wave propagation. With this solution we have a more accurate base from which to examine the ice lead diffraction process, and compare our earlier results based on the local reaction approximation.

4.1 Discussion of the thin plate equation

Before proceeding, we return to a more detailed discussion of the thin plate equation as it applies to a floating ice sheet. It is important to emphasize and clarify here exactly what properties of elastic wave propagation in the ice are included and what properties are ignored, when the thin plate equation is used to describe the state of vibration in the boundary plate material.

The response of the ice sheet to acoustic excitation from water can vary anywhere between the behavior of a thick layer to the behavior of a thin film, depending on the frequency-thickness product fH. (We work with fH here instead of the usual kH in order to more clearly demonstrate the dependence of Z_{in} on frequency and ice thickness.) For example, let us fix the ice thickness at 3 m and examine Z_{in} as the frequency decreases starting at 1000 Hz ($fH = 3000$), using the typical sea ice properties listed in Chapter 3. At 1000 Hz (Fig. 4.1 top) the ice is sufficiently thick enough to support interior modes. The input impedance undergoes rapid change at wavenumbers which match the phase speeds of these interior trapped modes. Thus Z_{in} at $fH = 3000$ is strongly dependent upon the horizontal wavenumber of excitation, and computation of Z_{in} depends on the additional complexity of exact elasticity theory, computed here using the Thomson-Haskell matrix representation. At 100 Hz (Fig. 4.1 middle) $|Z_{in}|$ is relatively constant in the homogeneous wavenumber region ($q/k < 1$) and approximately equal to $|-i\omega\rho_2 H|$ except for the rapid change near 62^o which is due to the longitudinal or symmetric Lamb mode. Note that the longitudinal wavenumber, which is a root of Eq.(3.3), is complex with an equivalent grazing or Mach angle $\approx 62^o$. Further out into the inhomogeneous spectrum ($q/k > 1$), $|Z_{in}|$ goes through a zero corresponding to a flexural wave in the free ice plate with *in vacuo* wavenumber k_f. The input impedance at $fH = 300$ is accurately described by the parallel addition of Z_- and $Z_\sim$, which are the wave impedances of the first two fundamental modes of the Rayleigh-Lamb equations alluded to in Chapter 3, such that

$$\frac{1}{Z_{in}} = \frac{1}{Z_-} + \frac{1}{Z_\sim} \tag{4.2}$$

An important distinction between the 1000 Hz and 100 Hz cases is that the former lies above the coincidence frequency and the latter lies below the coincidence frequency, defined by [62]

$$f_c = \frac{c^2}{2\pi}\sqrt{\frac{12\rho_1(1-\sigma^2)}{EH^2}} \tag{4.3}$$

and using typical ice parameters is equivalent to $f_c \approx 375/H$ with H in m and f_c in Hz. The coincidence frequency represents the frequency above which the free plate flexural wave phase speed becomes supersonic with respect to the ambient medium. This is evident in the 1000 Hz case where $|Z_{in}|$ increases monotonically in the inhomogeneous region of the wavenumber spectrum, and all trapped modes are confined to the homogeneous region, whereas in the 100 Hz case $|Z_{in}|$ passes through one final zero in the inhomogeneous region before starting its monotonic increase. A useful interpretation of the coincidence frequency for our purposes, is that f_c represents the frequency above which higher order modal solutions of the Rayleigh-Lamb equations are admitted.

Finally, at 10 Hz the input impedance is nearly exactly $|i\omega\rho_1 H|$ well into the inhomogeneous spectrum, except for a small perturbation due to the longitudinal wave which remains near the point $\arccos\frac{\ell}{k} \approx 62^o$. The longitudinal wave can be viewed as non-dispersive for our purposes, being nearly independent of fH. This is because it is more a function of the bulk elastic properties of the plate material. The longitudinal wave impedance Z_- becomes large in this fH range, and therefore its reciprocal has the appearance of a perturbation. This is in contrast to the free plate flexural wavenumber which has moved out further into the inhomogeneous spectrum, but remains a prominent feature of input impedance. The flexural wave is dispersive and characteristic of the bending stiffness of the plate material which in turn depends on fH. The fH value is now low enough for the thin plate equation to describe the state of vibration of the ice sheet surface. In other words, Eq.(3.10) can be used in place of Eq.(3.4) to determine the flexural wavenumber. It is conventional

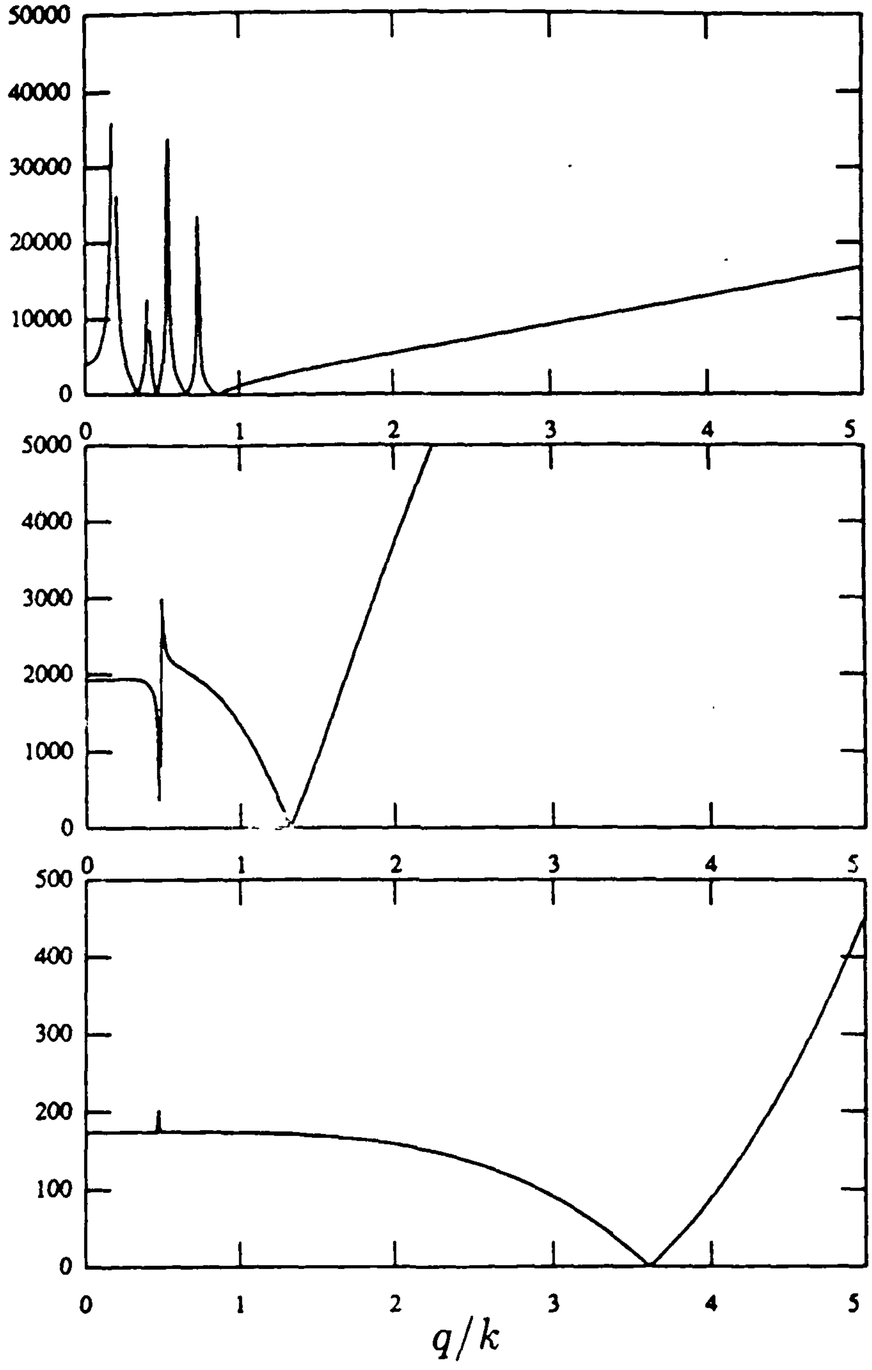

Figure 4.1: Magnitude of input impedance $|Z_{in}(q)|$. top: $fH = 3000$, middle: $fH = 300$, bottom: $fH = 30$. Horizontal axis for each case is normalized horizontal wavenumber (q/k) which corresponds to the cosine of the equivalent grazing angle.

to use the simpler plate equation to describe the dynamics of a thin plate and associated Z_{in} when the frequency is sufficiently low. Using typical ice parameters, accurate determination of the flexural wavenumber based on the thin plate equation has been verified for $fH \lesssim 150$ [68]. This value thus defines exactly what we mean by low-frequency diffraction from semi-infinite elastic ice.

Accurate prediction of the flexural wavenumber, however, does not mean the longitudinal wave has disappeared altogether; this would be equivalent to assuming $Z_{-}(q)$ is infinitely large and thus having no impact in Eq.(4.3). We have seen that ignoring the longitudinal wave is a good approximation for lower frequencies. Although, if either plane wave excitation corresponding to the critical grazing angle of the longitudinal wave ($\approx 62^o$), or the excitation is from an in-plane force due to a source within the ice, the finiteness of $Z_{-}(q)$ would become important [48]. But for the ice lead diffraction process, in the context of long range acoustic propagation, the excitation will be from plane waves coming from the ambient medium with grazing angles $\lesssim 20^o$, and we are not concerned with sources within the ice. Therefore, the original excitation does not contain spatial harmonics which violate the condition $|Z_{-}(q)| \gg |Z_{\smile}(q)|$, a necessary condition for ignoring the longitudinal wave. Thus we do ignore certain elements of elastic wave propagation in the ice when the ice response is characterized by the thin plate equation. But, when $fH \lesssim 150$, the only element ignored is the longitudinal wave which is of negligible importance, and the more important flexural wave remains fully characterized.

4.1.1 Fluid loading

Let us examine the thin plate equation under the kind of forcing conditions expected in the diffraction process, with

$$B\frac{\partial^4}{\partial x^4}U(x) - \rho_1 H\omega^2 U(x) = -p(x,t). \tag{4.4}$$

The forcing term on the right is the pressure from the acoustic field below the ice sheet. The vertical displacement of the ice surface, $U(x)$, is coupled to an external sound field supported by the fluid below the ice surface, which is the fluid loading. In this case we have a distributed, one-sided (because of the vacuum on one side) load from the plane wave excitation. The plane wave excitation means the spatial distribution of the loading has a single Fourier component, where, for example, an acoustic source under the ice presents a linear superposition of such components. Because pressure is proportional to density, one way to quantify fluid loading is the through the density of the ambient medium ρ. Thus, air with $\rho \approx 1$ kg/m^3 could be considered light fluid loading and water with $\rho \approx 1000$ kg/m^3 could be considered heavy fluid loading. But the loading must also take into account the spatial scale of excitation and the plate mass. A common parametric description of the loading which includes these factors is [27]

$$\epsilon_1 = \frac{\rho}{\rho_1}\frac{1}{kH} \tag{4.5}$$

which is a measure of the mass of fluid within one acoustic wavelength of the plate compared to the mass of the plate. For $\epsilon_1 \ll 1$ we have light fluid loading typical of problems found in aerodynamic applications.

Using the thin plate equation to characterize elastic effects, the solution of a plane wave incident upon a semi-infinite elastic plate in the asymptotic light loading limit was first demonstrated in [46], with an alternative solution given in [12]. An essential step in the solutions is the decomposition of the Wiener-Hopf kernel, which in this case is achieved asymptotically in the limit of $\epsilon_1 \rightarrow 0$. For frequencies below coincidence, the solutions include a coupled flexural wave propagating along the plate and assuming the form

$$\phi_{flex}(x, y) = Ae^{ik_{fL}x - y\sqrt{k_{fL}^2 - k^2}} \tag{4.6}$$

with complex amplitude A and flexural wavenumber k_{fL}. Since these solutions apply in the limit $\epsilon_1 \rightarrow 0$, the wavenumber k_{fL} is a perturbation from the *in vacuo* wavenumber k_f. The phase velocity of the flexural wave is subsonic ($k_{fL} > k$) and the associated pressure field decays exponentially in the y-direction. The equivalent loading parameter, however, for the case of an ice plate ensonified at a frequency of 50 Hz is $\epsilon_1 \approx 5/H$, with H the ice thickness in m. This is never a small parameter under realistic conditions, and therefore these solutions do not apply to the problem of low-frequency diffraction from an ice lead.

The other extreme is the asymptotic limit of heavy fluid loading limit and low frequency. A parameter known as the intrinsic fluid loading parameter [21], denoted here as ϵ_2, gives a measure of the fluid loading at the coincidence frequency, with

$$\epsilon_2 = \frac{\rho}{\rho_1}\sqrt{\frac{E}{12\rho_1 c^2(1-\sigma^2)}}. \tag{4.7}$$

As such, it is independent of frequency and plate thickness, and depends only on the physical properties of the plate material and ambient medium. For a steel plate immersed in water $\epsilon_2 \approx .13$, and for an ice sheet $\epsilon_2 \approx .61$, and thus the degree of fluid-structure coupling for the ice/water system is greater than that for the steel/water system. But we cannot consider the issue of "heavy" fluid loading until frequency and plate thickness are introduced. In other words, we must view the degree of fluid loading as how much the fluid-loaded flexural wavenumber, denoted here as $\bar{k}_f$, differs from the corresponding *in vacuo* wavenumber k_f. For example, one finds that the relative difference $(\bar{k}_f - k_f)/k_f$, for problems involving cm-thick steel will typically be much greater than that for m-thick ice. Use of a second parameter in the form of a Mach number

$$M = \frac{k}{k_f} \tag{4.8}$$

characterizes this property, and the heavy fluid loading, low-frequency regime is defined in [21] by the double limit

$$\epsilon_2 \ll 1, \qquad N = \frac{M}{\epsilon_2} \ll 1. \tag{4.9}$$

The solution of a plane wave incident upon a semi-infinite elastic plate in the asymptotic heavy fluid loading, low-frequency limit is presented in [21,11]. As in the light fluid loading limit, the decomposition of the Wiener-Hopf kernel is achieved asymptotically, here in the limit $N \to 0$. (In reference [11] an alternative loading parameter is used in the asymptotic decomposition). Part of this solution consists of a coupled flexural wave assuming the form

$$\phi_{flex}(x,y) = Ae^{ik_{fH}x - y\sqrt{k_{fH}^2 - k^2}}. \tag{4.10}$$

Here, k_{fH} is the low-frequency asymptotic limit of the flexural wavenumber with

$$k_{fH}^5 \sim \left(\frac{12\omega^2\rho_1}{H^3}\right)\left(\frac{1-\sigma^2}{E}\right) \tag{4.11}$$

and since $k_{fH} > k$ the associated field also decays exponentially in the y-direction.

The solution for heavy fluid loading at low-frequency is slightly more akin to our problem of sea ice and low-frequency acoustics, provided $fH \lesssim 1$. But for the more interesting cases of m-thick ice and frequencies $\gtrsim$ 10 Hz, $N = O(1)$, and we are clearly not in this asymptotic regime. (Note that one may also view the heavy fluid loading, low-frequency regime as satisfying the parametric range $1/\epsilon_1 \ll 1$. But ϵ_1 remains an $O(1)$ quantity for m-thick ice and frequencies $\gtrsim$ 10 Hz). Thus the fluid loading pertaining to sea ice and low-frequency acoustics cannot be characterized by simplifying heavy or light fluid loading limits; it lies somewhere between these limits.

In the next section we solve the diffraction problem with fluid loading pertaining to sea ice and low-frequency acoustics. Our problem will differ from those mentioned above not only in the fluid loading characteristics, but also in geometry since we are examining diffraction from two coupled half-planes, one being the free surface and the other being the elastic surface. But the crux of the problem will again lie in the decomposition of the Wiener-Hopf kernel. In this case, though, we employ a new approximate kernel built upon the framework of Chapter 3. This new kernel is not only valid in the 'mid-range' fluid loading regime, but duplicates the reported asymptotic heavy fluid loading, low-frequency limiting behavior of the kernel decompositions described in [21,11].

4.2 Solution of extended reaction diffraction problem

In this section we solve the problem of a monochromatic plane wave with grazing angle α incident upon two coupled half-planes, one representing a free surface and the other representing an elastic plate. The plate parameters and fluid loading conditions represent those found in the low-frequency ice lead diffraction process. The notation and problem geometry are the same as before, with additional notation introduced as necessary. The problem geometry is shown again in Fig. 4.2 giving the orientation of the plate displacement field $U(x)$. Note that the ambient medium lies above the planar boundary $y = 0$ with vacuum below, in order to be consistent with a more suitable display of the diffracted field.

The plane wave is incident upon a surface with the following mixed boundary conditions

$$\phi_T(x,0) = 0 \quad x < 0 \tag{4.12}$$

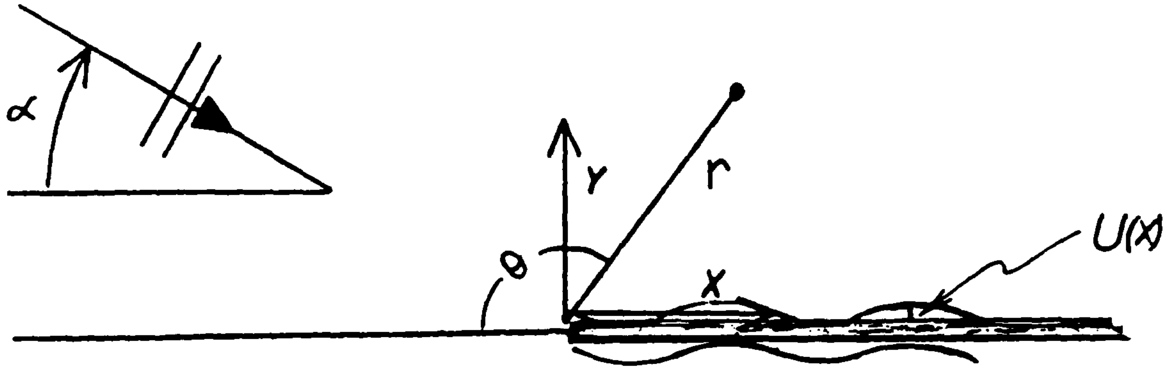

Figure 4.2: Exaggerated view of plate displacement $U(x)$ in the positive y-direction; field coordinate system is the same as in Chapters 2 and 3.

and

$$B\frac{\partial^4 U(x)}{\partial x^4} - \rho_1 H\omega^2 U(x) = i\omega\rho\phi_T(x,0) \quad x > 0. \tag{4.13}$$

As before, the total velocity potential field ϕ_T is composed of an incident, reflected, and diffracted field, with the reflected field originating from either of the semi-infinite planar boundaries. In this particular case the algebra is greatly simplified if we choose a reflected field originating from the free surface; this also maintains a parallel development with the results from Chapter 3. In using a free surface reflected field, the incident and reflected fields cancel along the boundary and thus we replace ϕ_T by ϕ_D along the boundary. The relation between the total velocity potential and the flexural wave displacement is

$$i\omega U(x) = \frac{\partial}{\partial y}\phi_T(x,0) \tag{4.14}$$

giving

$$U(x) = \frac{-i}{\omega}\frac{\partial}{\partial y}\phi_D(x,0) - \frac{2k\sin\alpha}{\omega}e^{ikx\cos\alpha}. \tag{4.15}$$

Finally, with use of Eq.(3.11) the boundary conditions become

$$\phi_D(x,0) = 0 \quad x < 0 \tag{4.16}$$

and

$$\frac{d^4}{dx^4}\phi_{Dy}(x,0) - k_f^4\phi_{Dy}(x,0) + \frac{\omega^2\rho}{B}\phi_D(x,0) = 2ik\sin\alpha[(k\cos\alpha)^4 - k_f^4]e^{ikx\cos\alpha} \quad x > 0 \quad (4.17)$$

where the partial derivative with respect to the y-coordinate is now denoted by the subscript y to simplify notation.

Applying the semi-infinite Fourier transform method (Jones's Method) to the boundary conditions we find for the $x < 0$ condition that

$$G(q) = G_-(q) \tag{4.18}$$

since $G_+(q) = 0$. For the $x > 0$ condition we utilize the following definition, consistent with the $L_+(q)$ used in Chapter 3

$$\int_0^\infty \phi_{Dy}(x,0)e^{-iqx}dx = L_-(q) \tag{4.19}$$

and therefore

$$\int_0^\infty \frac{d^4}{dx^4}\phi_{Dy}(x,0)e^{-iqx}dx = q^4L_-(q) + N(q) \tag{4.20}$$

where $N(q)$ is a polynomial in q which arises from the differentiation property of Fourier and Laplace transforms [36], with

$$N(q) = -\phi_{Dyxxx} + iq\phi_{Dyxx} + q^2\phi_{Dyx} - iq^3\phi_{Dy}. \tag{4.21}$$

The coefficients of $N(q)$ are constants, for example,

$$\phi_{Dyxxx} = \phi_{Dyxxx}(0^+,0) \tag{4.22}$$

with 0^+ indicating the elastic plate ($x > 0$) side of the origin. The coefficients depend on the boundary condition of $U(x)$ at $x = 0^+$; specifically, if the plate edge is free to move, and not hinged or fixed in any way such as in the case of an open ice lead, then the total force and moment must vanish at $x = 0^+$. These are the so-called free end boundary conditions, requiring [36]

$$U_{xxx}(0^+) = 0, \qquad U_{xx}(0^+) = 0. \tag{4.23}$$

With use of Eq.(4.15), we find two of the coefficients

$$\phi_{Dyxxx} = 2k\sin\alpha(k\cos\alpha)^3 \tag{4.24}$$

and

$$\phi_{Dyxx} = -2ik \sin\alpha (k\cos\alpha)^2. \tag{4.25}$$

The coefficients $-i\phi_{Dy}$ and ϕ_{Dyx} remain unknown at this point and will be referred to as c_1 and c_2, respectively, giving

$$N(q) = c_1 q^3 + c_2 q^2 + D_1 q + D_2 \tag{4.26}$$

with

$$D_1 = 2k\sin\alpha(k\cos\alpha)^2 \quad D_2 = -2k\sin\alpha(k\cos\alpha)^3.$$

The complete Fourier transform of the $x > 0$ boundary condition is thus

$$q^4 L_-(q) + N(q) - k_f^4 L_-(q) + \frac{\omega^2\rho}{B} G_-(q) = \frac{2k\sin\alpha[(k\cos\alpha)^4 - k_f^4]}{(q - k\cos\alpha)} \tag{4.27}$$

with the term on the right side considered a '−' function since it is a result of a semi-infinite ($x > 0$) Fourier transform. In order to proceed we need to express $L_-(q)$ in terms of $L_+(q)$ and other '−' functions. For this we observe that

$$L_+(q) + L_-(q) = -\sqrt{q^2 - k^2} \quad G(q) = -\sqrt{q^2 - k^2}\;\; G_-(q) \tag{4.28}$$

giving

$$L_-(q) = -L_+(q) - \sqrt{q^2 - k^2} G_-(q). \tag{4.29}$$

With this substitution, Eq.(4.27) becomes

$$-(q^4 - k_f^4)L_+(q) + N(q) = \frac{2k\sin\alpha[(k\cos\alpha)^4 - k_f^4]}{(q - k\cos\alpha)} - G_-(q)[\frac{\omega^2\rho}{B} - \sqrt{q^2 - k^2}(q^4 - k_f^4)]. \tag{4.30}$$

Finally, to maintain a parallel development with Chapter 3, we observe that

$$\frac{\omega^2\rho}{B} = \frac{\rho k_f^4}{\rho_1 H} = \eta k_f^4$$

and write Eq.(4.30) as

$$(q^4 - k_f^4)\frac{L_+(q)}{k_f^4} - \frac{N(q)}{k_f^4} = \frac{-\Omega}{(q - k\cos\alpha)} + G_-(q)(\sqrt{q^2 - k^2} + \eta - \frac{q^4\sqrt{q^2 - k^2}}{k_f^4}) \tag{4.31}$$

with

$$\Omega = \frac{2k\sin\alpha[(k\cos\alpha)^4 - k_f^4]}{k_f^4}. \tag{4.32}$$

Equation(4.31) is the Wiener-Hopf functional equation. It is similar to the ones developed for the asymptotic light and heavy fluid loading cases and single half-plane boundary, with common feature being the kernel

$$K(q) = \sqrt{q^2 - k^2} + \eta - \frac{q^4\sqrt{q^2 - k^2}}{k_f^4}. \tag{4.33}$$

It is interesting to see how the Wiener-Hopf functional equation changes when the elastic properties of the ice plate are removed. For this we set the Lamé constant, or shear modulus μ, equal to zero, which puts E equal to zero and k_f becomes infinite. In this limiting case Eq.(4.31) becomes

$$L_+(q) = \frac{-2k\sin\alpha}{(q - k\cos\alpha)} - G_-(q)(\sqrt{q^2 - k^2} + \eta) \tag{4.34}$$

which is the same as Eq.(3.20). It appears that the thin plate equation is a natural link to the local reacting approximation, with the effects of elasticity removed in the latter.

4.2.1 Recovery of $G_-(q)$

We are now at the crux of this problem, which is the issue of decomposing the kernel when a fluid loading parameter cannot be made small, i.e., extreme light or heavy fluid loading. Earlier we used an approximate kernel because decomposition of the exact kernel seriously restricts interpretation and utility of the final solution. Inclusion of elastic effects now compounds the kernel decomposition issue, such that an exact decomposition with its attendant complexity is feasible only through a perturbation from either the asymptotic light or heavy fluid loading limits. As before, we will employ an approximate kernel, but in this case it must track the more complicated behavior of the exact kernel.

Writing the kernel as

$$K(q) = \sqrt{q^2 - k^2} \; [\frac{\eta}{\sqrt{q^2 - k^2}} + 1 - \frac{q^4}{k_f^4}] \tag{4.35}$$

we see that if $\eta = 0$, a root of the kernel is k_f. The kernel is the characteristic equation for the modes of the thin elastic plate/water system; if $\eta = 0$ there is no fluid loading and *in vacuo* dynamics govern the problem. For $\eta \neq 0$, the roots of the kernel must be found numerically, which we do using the Newton-Raphson method [36], starting the iteration from k_f as a "seed" value. It is emphasized here, that there exist only two significant or real roots to the bracketed factor in Eq.(4.35) [20], and these will be called $\pm\bar{k}_f$, which relate to the undamped, subsonic flexural wave. In the limit of $\omega \rightarrow 0$ the roots can be determined algebraically from Eq.(4.11).

We now focus on the bracketed factor in Eq.(4.35) which houses the problem in the kernel decomposition. If we allow k_f to become infinite, such as in a limp plate, we have the same factor as the one already successfully approximated in Chapter 3. Let us call this form $k(q)$, as in Appendix B, where

$$k(q) = \frac{\eta}{\sqrt{q^2 - k^2}} + 1. \tag{4.36}$$

Now observe that $k(q) \cdot (1 - \frac{q^4}{k_f^4})$ shares the *same moments* (through the third moment) as the bracketed term. In other words, if the bracketed term is $k_1(q)$, then

$$\frac{d^m k_1(q)}{dq^m} = \frac{d^m k(q)}{dq^m} \tag{4.37}$$

evaluated at $q = 0$ for $m = 0$ through 3. This stems from the moment generating relationship between transformed quantities. Thus we can approximate the bracketed term by $\hat{k}(q) \cdot (1 - \frac{q^4}{k_f^4})$ to the same accuracy existing in the approximation for the local reacting case of Chapter 3. The details pertaining to this approximation, and a comparison with one of the known asymptotic kernel decompositions, are given in Appendix C.

An essential feature of our approximate kernel in this case is that it shares the same real root $\pm\bar{k}_f$. Other roots from the exact kernel are not retained; but these depend entirely upon the branch cut configuration in the root finding procedure, and would relate to non-propagating, evanescent waves, of no physical significance. We also agree that two additional, and entirely spurious, roots have been introduced these being $\pm i\bar{k}_f$. But these roots belong to the same class as the excluded roots whose residue contributions are exponentially small. We show later in the inversion that residue fields corresponding to the $\pm i\bar{k}_f$ roots are always severely exponentially damped. Finally, the creation of spurious roots is not a property isolated to our approximate kernel method. The asymptotic decompostion method will also introduce its own set of spurious roots [11].

Upon using the decomposed approximate kernel

$$\hat{K}(q) = \frac{\hat{K}_-(q)}{\hat{K}_+(q)} \tag{4.38}$$

the Wiener-Hopf equation becomes

$$(q^4 - k_f^4)\frac{L_+(q)}{k_f^4}\hat{K}_+(q) - \frac{N(q)}{k_f^4}\hat{K}_+(q) + \frac{\Omega}{(q - k\cos\alpha)}\hat{K}_+(q) = G_-(q)\hat{K}_-(q). \tag{4.39}$$

An additive decomposition of the last term on the left gives two terms analogous to Eqs.(3.24) and (3.25), these being

$$R_-(q) = \frac{\Omega\hat{K}_+(k\cos\alpha)}{(q - k\cos\alpha)} \tag{4.40}$$

and

$$R_+(q) = \frac{-\Omega\hat{K}_+(k\cos\alpha)}{(q - k\cos\alpha)} + \frac{\Omega\hat{K}_+(q)}{(q - k\cos\alpha)}. \tag{4.41}$$

Using the above, Eq.(4.39) assumes the form

$$(q^4 - k_f^4)\frac{L_+(q)}{k_f^4}\hat{K}_+(q) - \frac{N(q)}{k_f^4}\hat{K}_+(q) + R_+(q) = -R_-(q) + G_-(q)\hat{K}_-(q) = E(q) \tag{4.42}$$

where $E(q)$ is an entire function. Note that the polynomials $(q^4 - k_f^4)$ and $N(q)$ are analytic in the entire finite complex q-plane, and we can regard these as 'neutral' in terms of their '+' or '−' classification.

The decomposed kernel assumes the form

$$\hat{K}_-(q) = \frac{(q - i\sqrt{k^2 + \eta^2})}{\sqrt{q - ikn}} \cdot \frac{(q - kA_1)}{(q - kA_2)} \cdot (1 - \frac{q}{k_f}) \cdot (1 + \frac{iq}{k_f})e^{i\frac{\pi}{4}}\sqrt{r_1} \tag{4.43}$$

$$\hat{K}_+(q) = \frac{\sqrt{q + ikn}}{(q + i\sqrt{k^2 + \eta^2})} \cdot \frac{(q + kA_2)}{(q + kA_1)} \cdot [(1 + \frac{q}{k_f}) \cdot (1 - \frac{iq}{k_f})]^{-1}\frac{e^{i\frac{\pi}{4}}}{\sqrt{r_1}}.$$

These are very similar to the $\hat{K}_-$ and $\hat{K}_+$ decompositions employed in the local reacting problem [Eq.(3.27)], for example, the constants A_1 and A_2 are different here but perform a similar role. The $e^{i\frac{\pi}{4}}$ factor is necessary to preserve the property of evenness [59] in the approximate kernel, this being

$$\hat{K}_-(q) \cdot \hat{K}_+(-q) = 1. \tag{4.44}$$

Strictly speaking, the $e^{i\frac{\pi}{4}}$ factor should also be included in Eq.(3.27), but it cancels out when the decomposed kernel is implemented in the inversion; this will not be the case here, however. The parameter $r_1 = (\bar{k}_f/k_f)^4$ is used to insure proper behavior of $\hat{K}(q)$ as $q \to \infty$.

We are now ready to determine the nature of the entire function. Examining the '$-$' side of Eq.(4.42) we have

$$G_- \sim |q|^{-\nu-1} \quad \hat{K}_- \sim |q|^{\frac{5}{2}} \quad R_- \sim |q|^{-1} \quad q \to \infty$$

and for the '+' side we have

$$L_+ \sim |q|^{\frac{-1}{2}} \quad \hat{K}_+ \sim |q|^{\frac{-5}{2}} \quad R_+ \sim |q|^{-1} \quad q \to \infty$$

where in G_- and L_+, we have used the asymptotic properties established in Chapter 2. Taking into account the polynomials $(q^4 - k_f^4)$ and $N(q) \sim |q|^3$, and the fact that $\nu \geq 0$, we construct the combined '$-$' and '+' functions which have the property

$$|F_-(q)| < |q|^{\frac{3}{2}} \quad |F_+(q)| < |q|^{\frac{3}{2}} \quad q \to \infty.$$

Thus, the explicit version of Liouville's theorem stated in Chapter 2 tells us that $E(q)$ is a polynomial of degree 1 or less, giving

$$E(q) = e_0 + e_1 q. \tag{4.45}$$

The constants e_0 and e_1 will be determined later, but for now we may write

$$G_-(q) = \frac{1}{\hat{K}_-(q)}[e_0 + e_1 q + \frac{\Omega \hat{K}_+(k\cos\alpha)}{(q - k\cos\alpha)}]. \tag{4.46}$$

4.2.2 Determination of e_0 and e_1

The constants e_0 and e_1 which originate from the behavior of the entire function, are now resolved together with the unknowns c_1 and c_2 contained in $N(q)$. The four equations necessary to resolve the four unknowns are derived by removing the so-called apparent singularities [11,21]. Examining the '+' side of Eq.(4.42) we find that

$$(q^4 - k_f^4)L_+(q) = \frac{k_f^4 E(q)}{\hat{K}_+(q)} + N(q) - \frac{k_f^4 R_+(q)}{\hat{K}_+(q)}. \tag{4.47}$$

The function L_+ thus has singularities at $\pm k_f$ and $\pm ik_f$; but k_f and ik_f lie in the upper half-plane where L_+ is supposed to remain analytic. (Recall from Chapter Two, that L_+ is analytic for $Im(q) > -k_2$.) The removal of these singularities creates two equations

$$E(q) = R_+(q) - \frac{N(q)}{k_f^4}\hat{K}_+(q) \qquad q = k_f, ik_f. \tag{4.48}$$

Two more equations are derived from Eq.(4.27) in the same manner. Here L_- has singularities at $-k_f$ and $-ik_f$ which lie in the lower half-plane where L_- is supposed to remain analytic. (L_-, like G_-, is analytic for $Im(q) < k_2$.) The removal of these singularities creates the additional two equations

$$\frac{2k\sin\alpha[(k\cos\alpha)^4 - k_f^4]}{(q - k\cos\alpha)} - N(q) - \eta k_f^4 G_-(q) = 0 \qquad q = -k_f, -ik_f. \tag{4.49}$$

Now let the four unknowns form a column vector $\underline{x}$ with

$$\underline{x} = \begin{bmatrix} e_0 \\ e_1 \\ c_1 \\ c_2 \end{bmatrix} \tag{4.50}$$

and the coefficients of these unknowns form the coefficient matrix $\underline{\underline{A}}$, such that

$$\underline{\underline{A}}\ \underline{x} = \underline{b}. \tag{4.51}$$

The column vector $\underline{b}$ depends upon the end boundary conditions for the elastic plate which in our case are the aforementioned free end boundary conditions.

The unknowns are resolved through

$$\underline{x} = \underline{\underline{A}}^{-1}\underline{b} \tag{4.52}$$

with

$$\underline{\underline{A}} = \begin{bmatrix} 1 & k_f & \frac{\hat{K}_+(k_f)}{k_f} & \frac{\hat{K}_+(k_f)}{k_f^2} \\ 1 & ik_f & -i\frac{\hat{K}_+(ik_f)}{k_f} & -\frac{\hat{K}_+(ik_f)}{k_f^2} \\ 1 & -k_f & -\frac{\hat{K}_-(-k_f)}{\eta k_f} & \frac{\hat{K}_-(-k_f)}{\eta k_f^2} \\ 1 & -ik_f & i\frac{\hat{K}_-(-ik_f)}{\eta k_f} & -\frac{\hat{K}_-(-ik_f)}{\eta k_f^2} \end{bmatrix} \tag{4.53}$$

and

$$\underline{b} = \begin{bmatrix} R_+(k_f) - \frac{\hat{K}_+(k_f)}{k_f^4}(Ck_f + D) \\ R_+(ik_f) - \frac{\hat{K}_+(ik_f)}{k_f^4}(iCk_f + D) \\ \frac{\hat{K}_-(-k_f)}{\eta}[\frac{Ck_f - D}{k_f^4} - \frac{\Omega}{(k_f + k\cos\alpha)}] + \frac{\Omega \hat{K}_+(k\cos\alpha)}{(k_f + k\cos\alpha)} \\ \frac{\hat{K}_-(-ik_f)}{\eta}[\frac{iCk_f - D}{k_f^4} - \frac{\Omega}{(ik_f + k\cos\alpha)}] + \frac{\Omega \hat{K}_+(k\cos\alpha)}{(ik_f + k\cos\alpha)} \end{bmatrix} \tag{4.54}$$

with inversion of $\underline{\underline{A}}$ performed numerically using the MATRIXX numerical library [2].

In resolving a system of linear equations, errors in the coefficient matrix can cause errors in $\underline{x}$. The degree to which these errors propagate is measured by the condition number of the matrix $\kappa(\underline{\underline{A}})$. If $\kappa(\underline{\underline{A}})$ is large, the matrix may be ill-conditioned and small errors in $\underline{\underline{A}}$ may change $\underline{\underline{A}}^{-1}$ significantly enough to cause large errors in $\underline{x}$. A guideline to this error propagation is [30]

$$\log_{10}(\kappa(\underline{\underline{A}})) = m \tag{4.55}$$

where the loss in precision in the $\underline{x}$ vector is at most m significant digits. For example, if an element of $\underline{x}$ is .56321 and $m = 3$, the significance of the decimal digits beyond .56 may be unwarranted because of the effects of the numerical inversion of $\underline{\underline{A}}$. In our case $\kappa(\underline{\underline{A}})$ is typically $O(100)$, a number to be aware of, but not large enough to cause concern.

A related issue is the accuracy of the elements in $\underline{\underline{A}}$, specifically, whether the decompositions of the approximate kernel, $\hat{K}_+$ and $\hat{K}_-$, are accurate at the values $\pm k_f$ and $\pm ik_f$. In generating $\hat{K}(q)$ we used a four moment fit of the exact kernel $K(q)$ (Appendix C). But this does not guarantee accuracy of $\hat{K}(q)$ near $\pm k_f$ and $\pm ik_f$, where the latter is off the real-q axis. For this we employ two additional approximate kernels, with the same number of unknowns A_1 and A_2 as used in $\hat{K}$. But in this case the unknowns are determined by matching the zeroth moment or area, plus matching or "tagging" the value of the exact kernel at $\pm k_f$ and $\pm ik_f$. These will be called tagged kernels, with one tagging the value of the exact kernel at $\pm k_f$ (k_f-tagged) and the other tagging this value at $\pm ik_f$ (ik_f-tagged). In addition to providing accurate values for the coefficient matrix $\underline{\underline{A}}$, the method of tagged kernels opens up another route for which to implement approximate kernels in Wiener-Hopf problems. Details of the tagged kernels are presented in Part II of Appendix C.

4.3 Inversion of the diffracted field plane wave spectrum

In the inversion of $G_-(q)$ back to $\phi_D(r,\theta)$, we will try to parallel as much as possible the inversion pathways established earlier. The inversion in this case begins with the integral

$$\phi_D(x,y) = \int_{-\infty}^{\infty} \frac{1}{\hat{K}_-(q)}[e_0 + e_1 q + \frac{\Omega \hat{K}_+(k\cos\alpha)}{(q - k\cos\alpha)}]e^{iqx}e^{-y\sqrt{q^2-k^2}}\frac{dq}{2\pi}. \tag{4.56}$$

As before, two types of fields, SDP and residue, will come out of this inversion. For the SDP fields it will be convenient to separate e_0 and e_1 from the third term within the brackets because the latter gives rise to SDP fields which parallel those determined in Chapter 3. In this case there are two residue fields, one corresponding to the angle of specular reflection which we have seen before, the other corresponding to the coupled, subsonic flexural wave.

Before proceeding, though, it will be useful to confirm the dimensions of the various functions and constants introduced thus far. In this thesis the incident field ϕ_I is a plane wave velocity potential of unit amplitude. (We work with velocity potential, but when reporting the total diffracted power Π_D, we make the conversion to an incident plane pressure wave of unit amplitude which or 1 Pascal.) Given that ϕ_I, ϕ_R and ϕ_D are velocity potentials, the implicit dimension of the unit amplitude factor is $[L^2/T]$. In Chapter 3 the SDP diffracted fields assumed some combination of the form

$$\phi_D(r,\theta) = \chi M(\theta)P(\theta)\frac{e^{ikr}}{\sqrt{kr}} + O(\frac{1}{(kr)^{\frac{3}{2}}}) \tag{4.57}$$

where χ is a complex constant, $M(\theta)$ is the material function, and $P(\theta)$ is some dimensionless far field radiation pattern. The dimensions of χ and $M(\theta)$ are

$$[\chi] = [k^{\frac{1}{2}}] \quad [M(\theta)] = [k^{\frac{-1}{2}}]$$

such that ϕ_D remains dimensionless with implicit dimension of $[L^2/T]$. We will subsequently show that χ and $M(\theta)$ maintain these dimensions with $[\chi] = [\Omega\hat{K}_+]$ in this chapter, and with

$$[\Omega] = [k] \quad [\hat{K}_+] = [k^{\frac{-1}{2}}] \quad [\hat{K}_-] = [k^{\frac{1}{2}}].$$

These establish the dimensions of e_0 and e_1 giving

$$[e_0] = [k^{\frac{-1}{2}}] \quad [e_1] = [k^{\frac{-3}{2}}]$$

such that the integral in Eq.(4.56) is in fact dimensionless, and the elements of the $\underline{\underline{A}}\ \underline{x} = \underline{b}$ operation are dimensionally consistent.

4.3.1 The SDP and geometric wave fields

Let us begin with the third term within the brackets and write

$$\phi_{DA}(x,y) = \frac{\Omega \hat{K}_+(k\cos\alpha)}{2\pi} \int_{-\infty}^{\infty} \frac{1}{\hat{K}_-(q)} \frac{1}{(q - k\cos\alpha)} e^{iqx} e^{-y\sqrt{q^2-k^2}} dq \tag{4.58}$$

where the additional A in the subscript distinguishes this term from the first two terms within the brackets of Eq.(4.56). Employing the transformations used previously, we write

$$\phi_{DA}(r,\theta) = \chi \int_{\Gamma} P(\beta) M(\beta) e^{ikr\cos(\beta-\theta)} d\beta. \tag{4.59}$$

The inversion contour Γ, similar to the one in Fig. 3.2, is shown in Fig. 4.3. The $P(\beta)$ is the canonical angular spectrum used in Chapters 2 and 3, with

$$\chi = \frac{\Omega \hat{K}_+(k\cos\alpha)}{2\pi} \tag{4.60}$$

and $M(\beta)$ is a new material function, based on the approximate kernel developed in this chapter, of the form

$$M(\beta) = \frac{-\cos\frac{\beta}{2}}{\hat{K}_-(-k\cos\beta)}. \tag{4.61}$$

Equation(4.59) is strictly analogous to Eq.(3.29), where the decomposed kernels $\hat{K}_+, \hat{K}_-$ are from Eq.(4.43). It is emphasized here that Eqs.(4.60) and (4.61) are also analogous to Eqs.(3.30) and (3.31), respectively, but not the same. We will reuse the established relations for these expressions found in Eqs.(3.36) and (3.37). The common thread running through all three diffraction problems is the canonical angular spectrum $P(\beta)$, which assumes the same form established in Chapter 2.

The material function, like the one introduced in Chapter 3, is well-behaved for $0 < Re(\beta) < \pi$. But since $\hat{K}_-(q)$ contains zeroes at $q = \bar{k}_f$ and $q = i\bar{k}_f$, these translate into poles in $M(\beta)$ at

$$\beta = \arccos(\frac{-\bar{k}_f}{k}) \tag{4.62}$$

and

$$\beta = \arccos(\frac{-i\bar{k}_f}{k}) \tag{4.63}$$

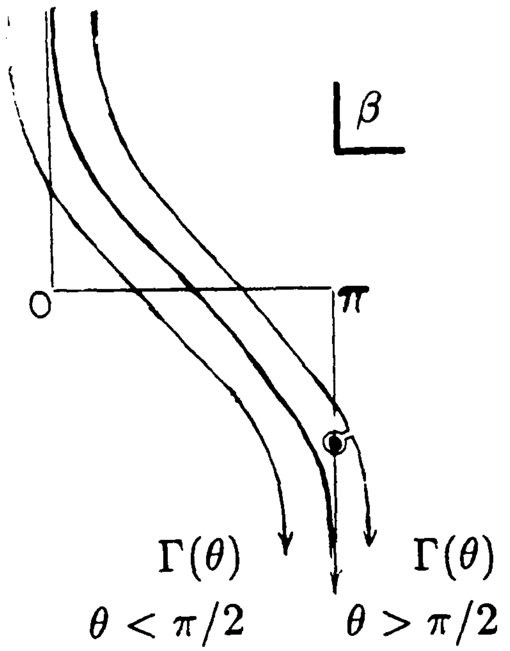

Figure 4.3: Orientation of the subsonic flexural wave pole with $\Gamma(\theta)$. Three SDP contours are shown. They are from left to right, $\theta < \frac{\pi}{2}, \theta = \frac{\pi}{2}$ and $\theta > \frac{\pi}{2}$.

respectively. The residue contributions from these poles are discussed in the next section, for now it is sufficient to note that any steepest descent path $\Gamma(\theta)$, characterized by real angle θ, will not have a saddle point which lies close to either of these poles.

Figure 4.3 shows the orientation of the subsonic flexural wave pole with the SDP contour $\Gamma(\theta)$. In deforming the Γ contour to $\Gamma(\theta)$, one sees that the flexural wave pole is captured only if the observation angle θ is greater than $\pi/2$. We have encountered this property before, with the pole at the specular angle $\beta = \pi - \alpha$, and the result was to express the field in the vicinity of $\theta = \pi - \alpha$ in terms of the Fresnel integral such that the field remains continuous across the line $\theta = \pi - \alpha$. For the flexural wave pole, however, we will not employ the Fresnel integral, since it adds unnecessary complexity without the benefit of improved accuracy. This is because the flexural wave field always decays exponentially in the y-direction, with the maximum rate of decay along the line $\theta = \frac{\pi}{2}$, and has nearly vanished at the point $kr \gg 1$ where the SDP fields become valid.

Thus we proceed with the analogy between Eq.(4.59) and Eq.(3.29), and write

$$\phi_{DA}(r,\theta) = \chi\int_{\Gamma}[P_1(\beta) + P_2(\beta)]M(\beta)e^{ikr\cos(\beta-\theta)}d\beta \tag{4.64}$$

giving

$$\phi_{DA1}(r,\theta) = (1-i)\sqrt{\pi}\chi P_1(\theta)M(\theta)\frac{e^{ikr}}{\sqrt{kr}} + O(\frac{1}{(kr)^{\frac{3}{2}}}) \tag{4.65}$$

with a remaining part

$$I = \chi\int_{\Gamma} P_2(\beta)M(\beta)e^{ikr\cos(\beta-\theta)}d\beta. \tag{4.66}$$

Equation(4.66) is analogous to Eq.(3.34), yielding a residue field contribution for the angular sector $\theta > \pi - \alpha$. We identify this as a geometric field, with

$$\phi_{geo}(r,\theta) = -2\pi i\frac{\chi M(\pi-\alpha)}{\sin\frac{\alpha}{2}}e^{ikr\cos(\alpha+\theta)}. \tag{4.67}$$

The equality of Eq.(3.37) also applies here, giving ϕ_{geo} the correct complex amplitude of $1 + R(\alpha)$. Here the reflection coefficient $R(\alpha)$ is that of a thin plate in which the elastic properties are modeled by the thin plate equation, with

$$R(\alpha) = \frac{Z_{in}(\alpha) - \frac{\rho\omega}{k\sin\alpha}}{Z_{in}(\alpha) + \frac{\rho\omega}{k\sin\alpha}} \tag{4.68}$$

and Z_{in} is the input impedance from Eq.(3.10). Having accounted for the pole in Eq.(4.66) we can express the rest of the integral in a way analogous to Eqs.(3.39) and (3.40), giving

$$\phi_{DA2}(r,\theta) = \frac{1+R(\alpha)}{2}\mathcal{F}(r,\theta;\alpha) \tag{4.69}$$

plus

$$\phi_{DA3}(r,\theta) = (1-i)\sqrt{\pi}\chi P_2(\theta)[M(\theta) - M(\pi-\alpha)]\frac{e^{ikr}}{\sqrt{kr}} + O(\frac{1}{(kr)^{\frac{3}{2}}}). \tag{4.70}$$

The remaining portion of the integral in Eq.(4.56) is denoted

$$\phi_{DB}(x,y) = \frac{1}{2\pi}\int_{-\infty}^{\infty}\frac{1}{\hat{K}_-(q)}[e_0 + e_1 q]e^{iqx}e^{-y\sqrt{q^2-k^2}}dq \tag{4.71}$$

which we express in polar coordinates as

$$\phi_{DB}(r,\theta) = \frac{k}{2\pi}\int_{\Gamma}\frac{\sin\beta}{\cos\frac{\beta}{2}}[-e_0 + e_1 k\cos\beta]M(\beta)e^{ikr\cos(\beta-\theta)}d\beta. \tag{4.72}$$

Since this integral is well-behaved for $0 < Re(\beta) < \pi$ ($\cos\frac{\beta}{2}$ is not a problem because $M(\beta)$ vanishes at $\beta = 0$ and π) thus we can use the SDP evaluation method [Eq.(2.38)] directly and write

$$\phi_{DB}(r,\theta) = (1-i)\frac{k\sin\theta}{2\sqrt{\pi}\cos\frac{\theta}{2}}[-e_0 + e_1 k\cos\theta]M(\theta)\frac{e^{ikr}}{\sqrt{kr}} + O(\frac{1}{(kr)^{\frac{3}{2}}}). \tag{4.73}$$

4.3.2 The coupled, subsonic flexural wave field

The diffracted field plane wave spectrum represented by the integral in Eq.(4.56) has now been completely inverted except for the contribution due to the flexural wave; we will call the flexural wave contribution ϕ_{flex}. The flexural wave arises from the pole at $q = \bar{k}_f$; here it is more convenient to maintain the x, y coordinate system for evaluating the residue. The pole at $q = \bar{k}_f$, and the one at $q = i\bar{k}_f$, are due to equivalent zeroes in $\hat{K}_-$ (Eq.(4.43)); because both poles lie in an upper half-plane with respect to the inversion contour, their residues are captured only for $x > 0$. Therefore the pole at $q = i\bar{k}_f$ always gives an exponentially damped residue contribution of no physical significance and will be ignored. We evaluate Eq.(4.56) for $x > 0$ by extending the inversion contour into a semi-circle in the upper half of the complex q-plane with the residue contribution at $\bar{k}_f$ giving

$$\phi_{flex}(x,y) = Ae^{i\bar{k}_f x - y\sqrt{\bar{k}_f^2 - k^2}} \tag{4.74}$$

where

$$A = \frac{-\bar{k}_f}{\sqrt{2r_1}}[e_0 + e_1\bar{k}_f + \frac{\Omega\hat{K}_+(k\cos\alpha)}{(\bar{k}_f - k\cos\alpha)}]\frac{\sqrt{\bar{k}_f - ikn}(\bar{k}_f - kA_2)}{(\bar{k}_f - i\sqrt{k^2+\eta^2})(\bar{k}_f - kA_1)}. \tag{4.75}$$

The inversion of Eq.(4.56) is now complete, with the total diffracted field being the coherent sum of five component fields

$$\phi_D = \phi_{DA1} + \phi_{DA2} + \phi_{DA3} + \phi_{DB} + \phi_{flex}. \tag{4.76}$$

The first three component fields are analogous to those found in the local reaction case. The additional cylindrical field ϕ_{DB} and the surface wave field ϕ_{flex} are the result of including the elastic properties of the thin plate in the diffraction process.

4.4 The diffracted field and check of the boundary conditions

Because the component fields, with the exception of ϕ_{flex}, are not individually observable, meaningful interpretation must be reserved for their coherent sum, and the component fields themselves are only of academic interest. Nevertheless, partitioning into component fields was an effective strategy for inverting the Fourier integral of the diffracted field, which was the end product of the Wiener-Hopf procedure. The new set of component fields allows one to compare the changes between the local reaction case and the extended reaction case, with the latter including elements of elastic wave propagation. One such change is the additional residue contribution due to excitation of the flexural wave; another change is the additional SDP field which we call ϕ_{DB}.

Let us repeat the display of the component fields for the case of extended reaction. Here, as in Chapters 2 and 3, the incident field is a monochromatic plane wave of 50 Hz with $\alpha = 15^o$. The material now is ice with $\rho_2 = 920\text{kg/m}^3$, $H = 2\text{m}$, and the ice elastic properties represented by $c_l = 3500\text{m/s}$ and $c_t = 1800\text{m/s}$ with Poisson's ratio $\sigma = .32$ and Young's modulus $E = 7.92\ 10^9\text{Pa}$. The phase speed of the coupled flexural wave with wavenumber $\bar{k}_f$ is 616 m/s, down from 748 m/s which represents the *in vacuo* (k_f) phase speed. Note that the coupled flexural wave is subsonic with respect to the water sound speed but supersonic with respect to the air sound speed, and thus there is propagation and subsequent energy loss into the air medium due to the flexural wave. But with the air density 1000 times less than ice/water density, the energy loss will at most be a small perturbation and our vacuum approximation for the air medium remains a good one. Contours of equal amplitude level for ϕ_{DA1}, ϕ_{DA2} and ϕ_{DA3} are shown in Figs. 4.4, 4.5 and 4.6. These are the extended reaction counterparts to Figs. 3.3, 3.4 and 3.5.

The additional cylindrical spreading field ϕ_{DB} is shown in Fig. 4.7. Inclusion of elasticity in the diffraction problem gave rise to this field together with the coupled flexural wave. The overall level of ϕ_{DB} is considerably lower (by about 20 dB) than the other component fields, and therefore, in the ice lead diffraction process, ϕ_{DB} plays a minor role in the total diffracted field. Nevertheless, ϕ_{DB} is of particular interest because the directivity of this

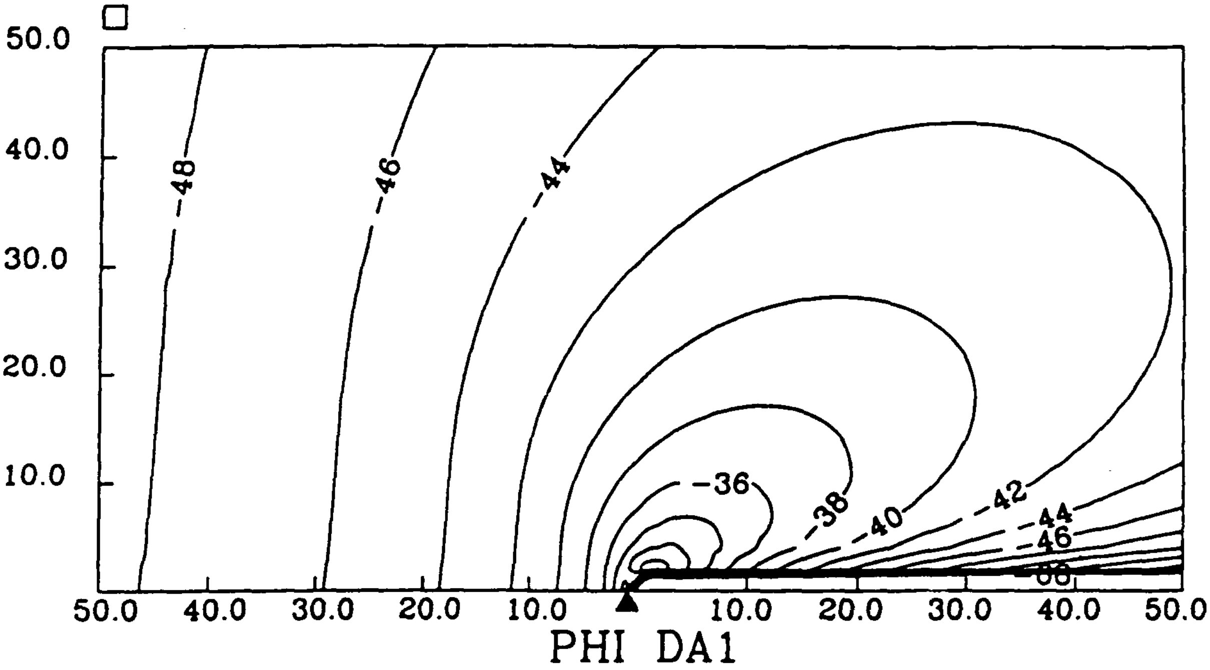

Figure 4.4: Contours of equal amplitude level for $\phi_{DA1}(r, \theta)$ with $\alpha = 15°$. The boundary discontinuity at the origin is marked by the triangle, with the free surface on the left side and the elastic thin plate surface on the right side. The distance from the origin is in units of $10 \cdot kr$. The contour levels are in dB referenced to a unit amplitude incident wave field.

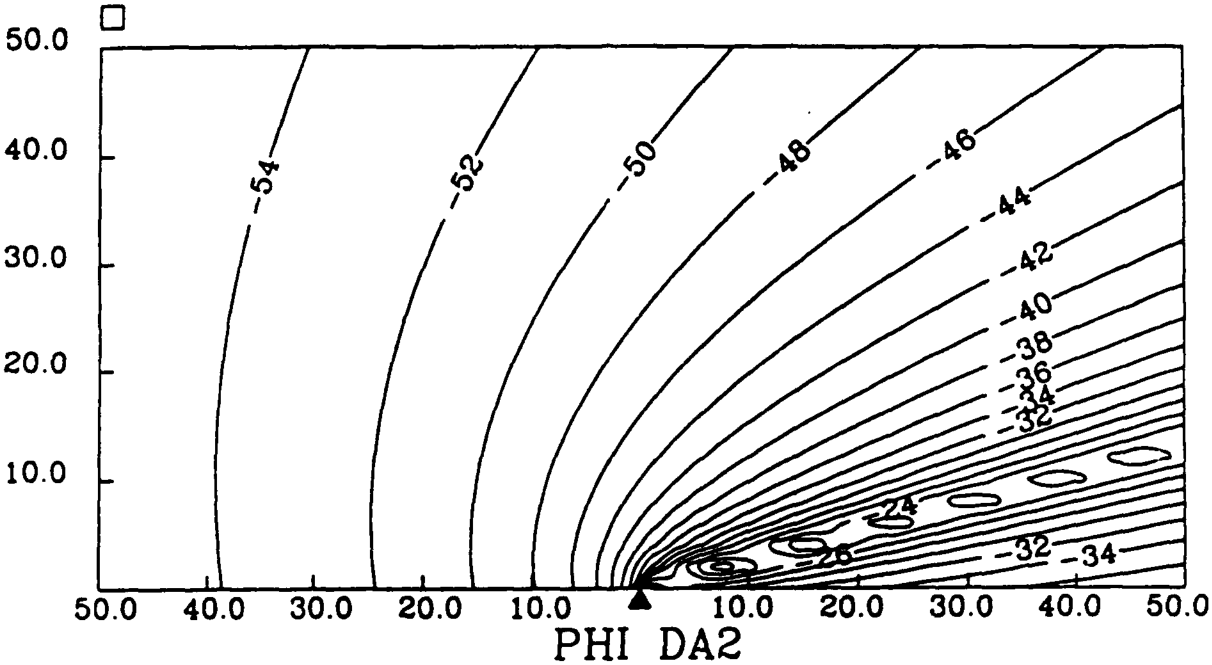

Figure 4.5: Contours of equal amplitude level for $\phi_{DA2}(r,\theta)$ with $\alpha = 15^o$. The boundary discontinuity at the origin is marked by the triangle, with the free surface on the left side and the elastic thin plate surface on the right side. The distance from the origin is in units of $10 \cdot kr$. The contour levels are in dB referenced to a unit amplitude incident wave field.

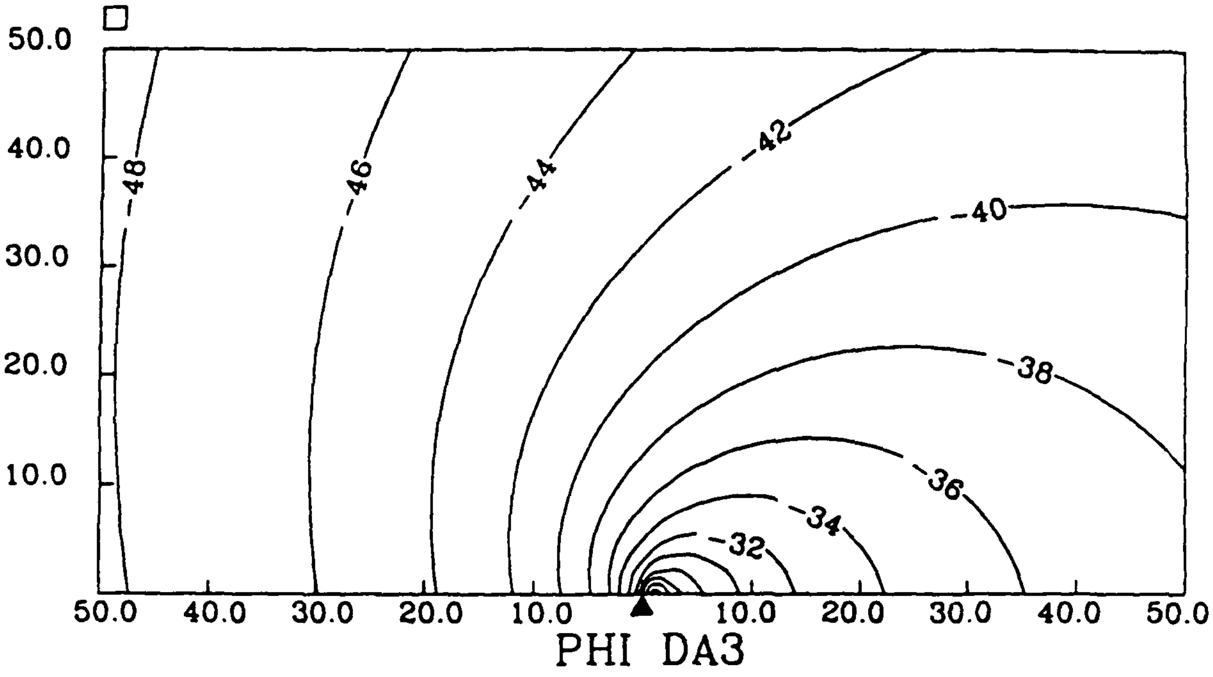

Figure 4.6: Contours of equal amplitude level for $\phi_{DA3}(r,\theta)$ with $\alpha = 15^o$. The boundary discontinuity at the origin is marked by the triangle, with the free surface on the left side and the elastic thin plate surface on the right side. The distance from the origin is in units of $10 \cdot kr$. The contour levels are in dB referenced to a unit amplitude incident wave field.

field, unlike the other component fields, does not strongly depend on grazing angle α. The only α dependence lies in the constants e_0 and e_1, and these seem to change in a manner such that the directivity remains unchanged with change in α. The ϕ_{DB} directivity is similar to a dipole, but with the maximum level of its far field radiation pattern off the vertical axis by roughly 20° for this example. One expects the directivity properties of the ϕ_{DB} field to be similar to the total diffracted field resulting from an ice-borne flexural wave incident upon a discontinuity such as a floe edge, and thereby acting as a possible source of ambient noise in the Arctic waters [47].

Returning to the focus of our problem, the coherent sum of the component fields ϕ_{DA1}, ϕ_{DA3} and ϕ_{DB} is shown in Fig. 4.8. This combined field is qualitatively rather different from the analogous combined field for case of local reaction (Fig. 3.6). The reason for this is unclear, but small changes in the reflection coefficient phase (cf. below) will establish a different coherent relation among the various component fields. The total diffracted field is shown in Fig. 4.9, and included here is the contribution from the coupled flexural wave for $x > 0$ [Eq.(4.74)]. One notices that qualitatively the diffracted field from the extended reaction case is quite similar to the one for local reaction (Fig. 3.7). Adding the flexural wave raises the level of ϕ_D only a small fraction along the $x > 0$ boundary for the extended reaction case. Also, the -60 dB contour for the local reaction case lies slightly further into the backscatter region than for the extended reaction case. Evidently this is due to the small increase in Z_{in} for the local reaction case over the extended reaction case.

The reflection coefficient for the extended reaction case is

$$R(\alpha) = -.9814 \quad - .1918 \ i. \tag{4.77}$$

For the equivalent local reaction case presented in Chapter 3 the reflection coefficient is

$$R(\alpha) = -.9786 \quad - .2056 \ i. \tag{4.78}$$

In both cases $|R| = 1$, however, by incorporating effects of elasticity in the ice, the input impedance modulus is reduced or "softened" by a small amount

$$\epsilon_z = (\frac{k \cos \alpha}{k_f})^4 \tag{4.79}$$

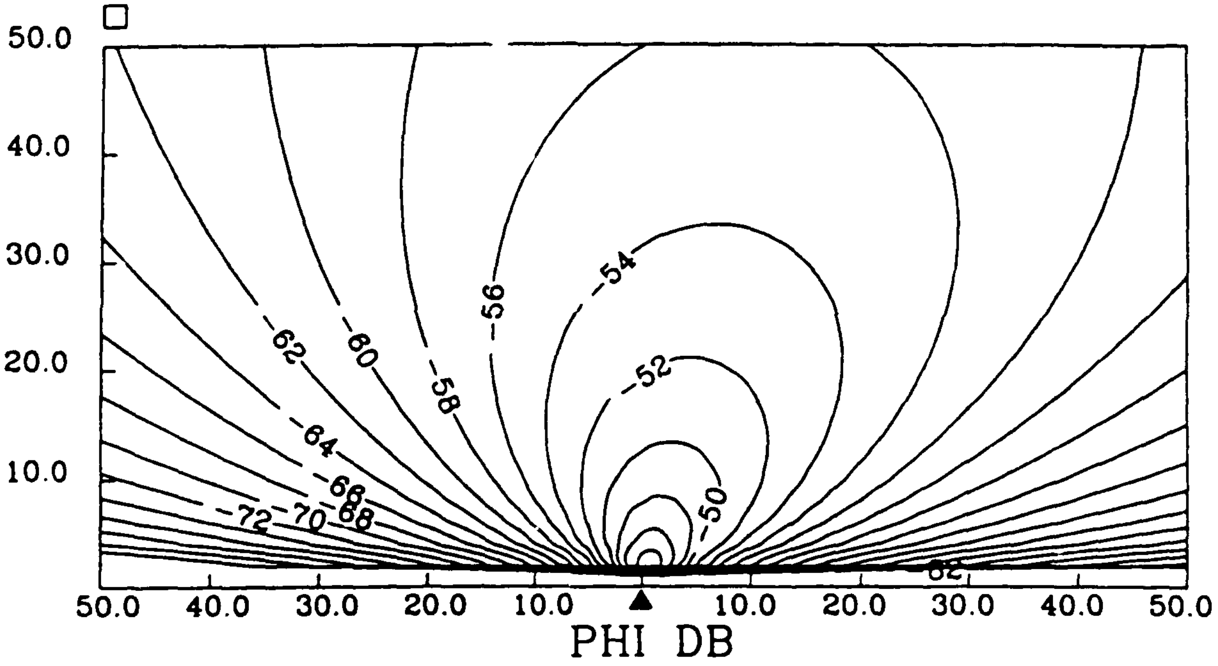

Figure 4.7: Contours of equal amplitude level for $\phi_{DB}(r,\theta)$ with $\alpha = 15°$. The boundary discontinuity at the origin is marked by the triangle, with the free surface on the left side and the elastic thin plate surface on the right side. The distance from the origin is in units of $10 \cdot kr$. The contour levels are in dB referenced to a unit amplitude incident wave field.

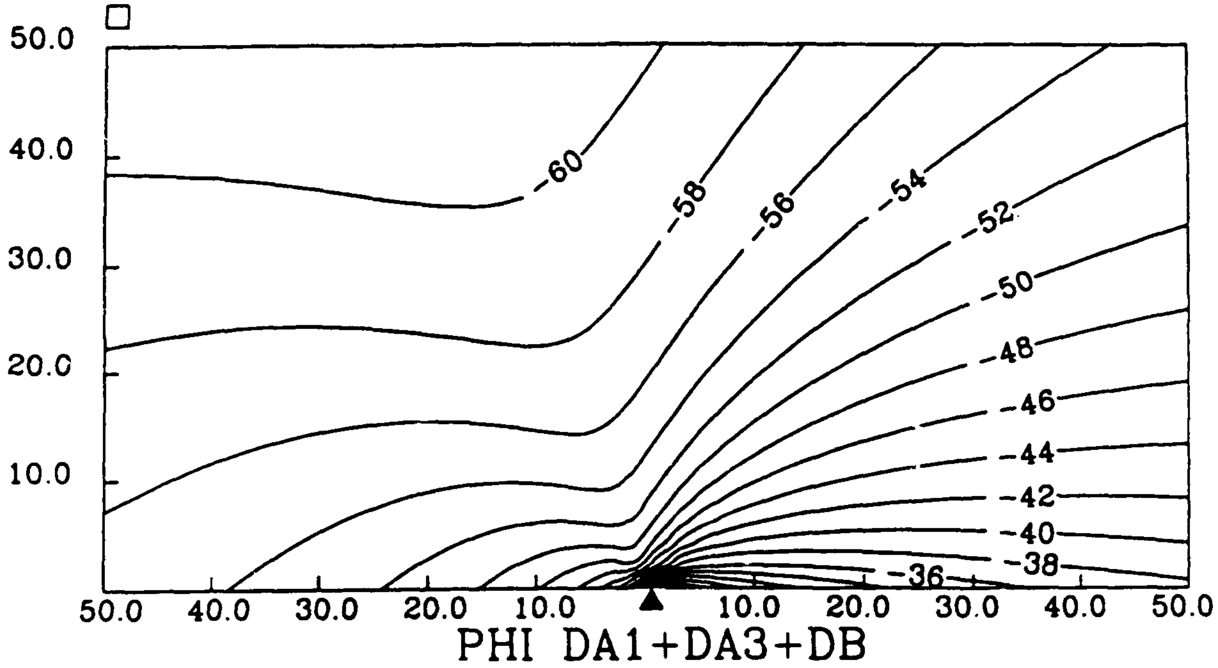

Figure 4.8: Contours of equal amplitude level for the superposition of $\phi_{DA1}(r,\theta)$, $\phi_{DA3}(r,\theta)$ and $\phi_{DB}(r,\theta)$ with $\alpha = 15^o$. The boundary discontinuity at the origin is marked by the triangle, with the free surface on the left side and the elastic thin plate surface on the right side. The distance from the origin is in units of $10 \cdot kr$. The contour levels are in dB referenced to a unit amplitude incident wave field.

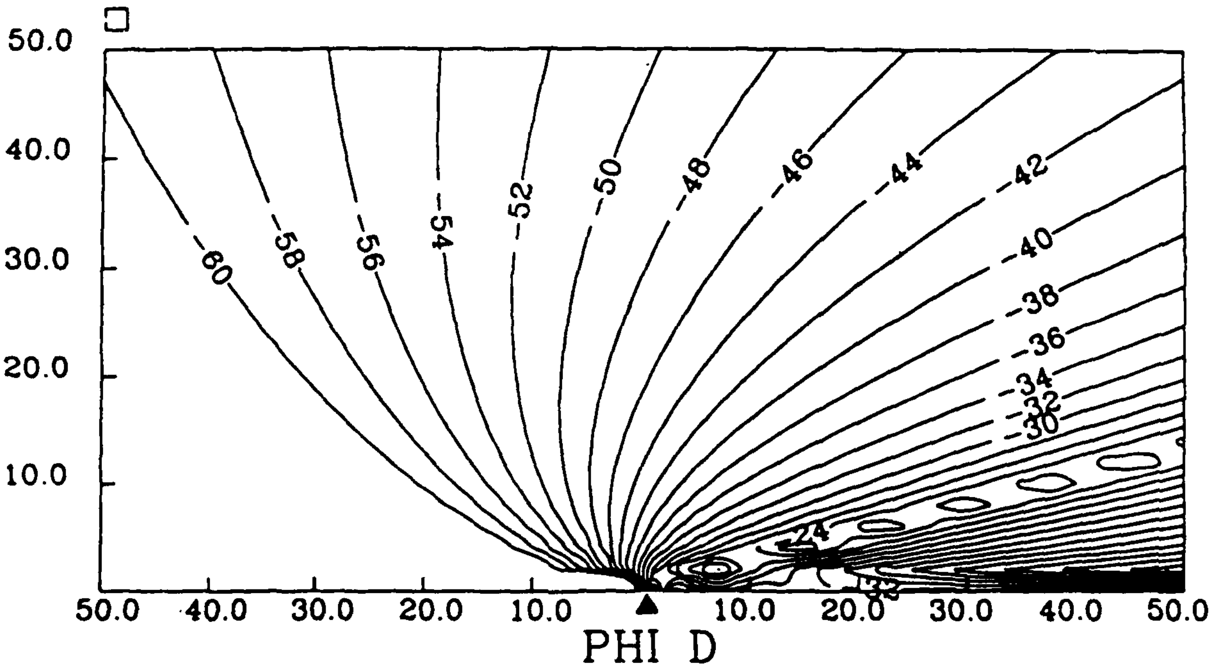

Figure 4.9: Contours of equal amplitude level for $\phi_D(r,\theta)$ with $\alpha = 15^o$. The boundary discontinuity at the origin is marked by the triangle, with the free surface on the left side and the elastic thin plate surface on the right side. The distance from the origin is in units of $10 \cdot kr$. The contour levels are in dB referenced to a unit amplitude incident wave field.

such that

$$Z_{in} = -i\omega\rho_1 H(1 - \epsilon_z) \tag{4.80}$$

with ϵ_z=.06 in this example. With consideration of Eq.(4.68), the small value of ϵ_z accounts for the observed change in R. We note that for small grazing angles $\alpha \lesssim 15^\circ$, the parametric dependence for the reduction in Z_{in} from its equivalent local reacting value is $\epsilon_z = \xi(kH)^2$ with $\xi \approx .33$. The ξ parameter is an intrinsic property of the water and sea ice material properties, being independent of frequency and ice plate thickness.

Before confirming that our solution satisfies the mixed boundary conditions, let us first review the hierarchy used in Chapters 2 and 3 for examining the accuracy of the solution along the planar boundary. Plane wave fields, or fields which orginate from residue contributions, are considered $O(1)$ fields and their coherent sum must satisfy the mixed boundary conditions exactly. Cylindrical wave fields which arise from SDP contributions and are expressed in terms of an asymptotic series in $\epsilon = 1/\sqrt{kr}$, must also satisfy the mixed boundary conditions, but the accuracy here need be only at the level of their lowest order $O(\epsilon)$, and we tolerate errors in the next order which is $O(\epsilon)^3$.

For $x < 0$ *the boundary condition* Eq.(4.12) *is satisfied by the incident and free surface* reflected fields, giving the equivalent boundary condition for ϕ_D as Eq.(4.16). No residues in the integral representation of $\phi_D(x,0)$ are captured for $x < 0$, and the fields resulting from SDP evaluation, ϕ_{DA1} and ϕ_{DA3}, plus the asymptotic form of ϕ_{DA2}, are in exact antiphase to $O(\epsilon)$ satifying Eq.(4.16) to the same order. Note that ϕ_{DB} vanishes along the entire $y = 0$ boundary and so does not enter into this boundary condition.

For $x > 0$, the relevant boundary condition is Eq.(4.17). First, let us confirm whether the residues correctly balance. These residues are from the following integrals which are derived from Eq.(4.17):

$$\phi_D(x,0) = \int_{-\infty}^{\infty} \frac{1}{\hat{K}_-(q)}[e_0 + e_1 q + \frac{\Omega\hat{K}_+(k\cos\alpha)}{(q - k\cos\alpha)}]e^{iqx}\frac{dq}{2\pi} \tag{4.81}$$

$$\phi_{Dy}(x,0) = -\int_{-\infty}^{\infty} \frac{\sqrt{q^2 - k^2}}{\hat{K}_-(q)}[e_0 + e_1 q + \frac{\Omega\hat{K}_+(k\cos\alpha)}{(q - k\cos\alpha)}]e^{iqx}\frac{dq}{2\pi} \tag{4.82}$$

$$\frac{d^4\phi_{Dy}(x,0)}{dx^4} = -\int_{-\infty}^{\infty} \frac{q^4\sqrt{q^2 - k^2}}{\hat{K}_-(q)}[e_0 + e_1 q + \frac{\Omega\hat{K}_+(k\cos\alpha)}{(q - k\cos\alpha)}]e^{iqx}\frac{dq}{2\pi}. \tag{4.83}$$

Each integral yields a residue contribution for the poles at $q = k\cos\alpha$ and $q = \bar{k}_f$; for the pole at $q = k\cos\alpha$ the residue contributions are

$$\phi_D(x,0) = \frac{i\Omega}{\hat{K}(k\cos\alpha)} e^{ik\cos\alpha x} \tag{4.84}$$

$$\phi_{Dy}(x,0) = \frac{-\Omega k\sin\alpha}{\hat{K}(k\cos\alpha)} e^{ik\cos\alpha x} \tag{4.85}$$

$$\frac{d^4\phi_{Dy}(x,0)}{dx^4} = \frac{-(k\cos\alpha)^4\Omega k\sin\alpha}{\hat{K}(k\cos\alpha)} e^{ik\cos\alpha x}. \tag{4.86}$$

Entering the above into the right side of Eq.(4.17), we find that the equality

$$\frac{-(k\cos\alpha)^4\Omega k\sin\alpha}{\hat{K}(k\cos\alpha)} + \frac{k_f^4\Omega k\sin\alpha}{\hat{K}(k\cos\alpha)} + \frac{\omega^2\rho}{B}\frac{i\Omega}{\hat{K}(k\cos\alpha)} = 2ik\sin\alpha[(k\cos\alpha)^4 - k_f^4] \tag{4.87}$$

must hold for the residue contributions at $q = k\cos\alpha$ to be balanced. To confirm this equality, we use the established relations from Eqs.(3.36) and (3.37), where in this case the constant $i\Omega$ is strictly analogous to the $-2ik\sin\alpha$ found in these equations, giving

$$\frac{i\Omega}{\hat{K}(k\cos\alpha)} = 1 + R \tag{4.88}$$

where it is understood that $R = R(\alpha)$. We recast Eq.(4.87) using the relation between B and k_f giving

$$(1+R)\left[i\omega\rho_1 H[(\frac{k\cos\alpha}{k_f})^4 - 1] + \frac{\omega\rho}{k\sin\alpha}\right] - 2i\omega\rho_1 H[(\frac{k\cos\alpha}{k_f})^4 - 1] = 0. \tag{4.89}$$

This is an exact equality in light of the definition of the reflection coefficient [Eq.(4.68)] and therefore the residues from the pole at $q = k\cos\alpha$ are balanced.

The pole at $q = \bar{k}_f$ arises from a zero in the decomposed kernel $\hat{K}_-(q)$. We have already evaluated the residue contribution of $\phi_D(x,0)$ due to this pole [Eq.(4.74)], and therefore expect the following:

$$\phi_{Dy}(x,o) = -\sqrt{\bar{k}_f^2 - k^2} A e^{i\bar{k}_f x} \tag{4.90}$$

and

$$\frac{d^4\phi_{Dy}(x,o)}{dx^4} = -\bar{k}_f^4\sqrt{\bar{k}_f^2 - k^2} A e^{ik_f x} \tag{4.91}$$

as residue contributions for Eqs.(4.82) and (4.83), respectively. Collecting the three residue contributions we find that

$$-\bar{k}_f^4\sqrt{\bar{k}_f^2 - k^2} + k_f^4\sqrt{\bar{k}_f^2 - k^2} + \frac{\omega^2\rho}{B} = 0 \tag{4.92}$$

is a requirement for the residue contributions from the pole at $q = \bar{k}_f$ to balance. But Eq.(4.92) is simply the characteristic equation [Eq.(4.35)] restated, and since $\bar{k}_f$ is necessarily a root of the characteristic equation, the residues from the pole at $q = \bar{k}_f$ are indeed balanced. With this we have demonstrated that the boundary condition for $x > 0$ is satisfied exactly by the plane wave fields.

To evaluate the $x > 0$ boundary conditions for the SDP fields, let us recast Eq.(4.17) into

$$\phi_{Dy}(x,0) - \frac{1}{k_f^4}\frac{d^4\phi_{Dy}(x,0)}{dx^4} = \eta\phi_D(x,0). \tag{4.93}$$

(Note that we did not include the right side of Eq.(4.17) because this belongs to the residue balance.) The above is the extended reaction analogy to Eq.(3.44); let us also examine this equation in terms of an asymptotic balance in powers of ϵ as in Chapter 3. First, we observe that the leading order term of the SDP contributions to $\phi_D(x,0)$ vanishes, because $\phi_{DA3}(x,0)$ and $\phi_{DA2}(x,0)$ are in exact anti-phase at the $O(\epsilon)$ level, with $\phi_{DA1}(x,0)$ and $\phi_{DB}(x,0)$ vanishing along the boundary for $x > 0$. Now to strike an asymptotic balance between both sides of Eq.(4.93) requires the two terms on the left side to also vanish at the $O(\epsilon)$ level. The integral representation of the first term is given in Eq.(4.82), and in a manner exactly parallel to the analysis of Eq.(3.45), one sees that the leading order behavior of this term is $O(1/(kx)^{\frac{3}{2}})$ or $O(\epsilon^3)$, meaning this term vanishes at the $O(\epsilon)$ level. The second term behaves the same way, with its leading order behavior being exactly $(k/k_f)^4$ times that of the first term, and the asymptotic balance of Eq.(4.93) is confirmed to the $O(\epsilon)$ level.

We return a final time to the Karp-Karal lemma as we are applying it to the ice lead diffraction process. The Karp-Karal lemma applies only to a local reacting, finite impedance boundary condition. In Chapter 3 we worked with such a boundary condition [Eq.(3.12)] and observed that the behavior of ϕ_D along the finite impedance boundary conformed with this lemma, namely that the $O(\epsilon)$ behavior had vanished and the lowest order was $O(\epsilon^3)$.

We can recover this same boundary condition from Eq.(4.93) by allowing the Lamé constant $\mu \to \infty$, and thereby $k_f \to \infty$. But for $\mu \neq 0$, or the case of extended reaction, there exists an $O(1)$ plane wave field along the $x > 0$ boundary in the form of the coupled flexural wave ϕ_{flex}. The flexural wave is a residue contribution of ϕ_D and was shown to be appropriately balanced along the boundary. We will show subsequently that the allocation of the total diffracted field power between ϕ_{flex} and the rest of the component fields in Eq.(4.76), strongly favors the latter. Thus if we ignore for the moment the power contribution from the ϕ_{flex} component field, we can say that $\phi_D(x,0)$ also vanishes in the extended reaction case at the $O(\epsilon)$ level with the leading order being $O(\epsilon^3)$.

The $O(\epsilon^3)$ leading order behavior of $\phi_D(x,0)$ implies that the intensity of $\phi_D(x,0) \sim 1/(kx)^3$. That is, for $x = l \gtrsim \lambda$, where λ is the wavelength in the ambient medium, the intensity level of $\phi_D(x,0)$ has diminished in excess of 24 dB. This property will be exploited in the next chapter when we apply our results to diffraction from finite-length ice leads of some characteristic length $\gtrsim l$.

4.5 Total diffracted power for extended reaction case and comparison with local reaction case

In this section we examine the total diffracted power Π_D due to a monochromatic plane wave incident upon a free surface coupled to a semi-infinite surface composed of a layer of sea ice. This is our basic model for the ice lead diffraction process. In view of the Karp-Karal lemma, the semi-infinite aspect of the model is not a serious restriction. There are, of course, other limitations placed on the interpretation of Π_D which arise from the two-dimensional geometry, limitations no different from those which pertain to the majority of solutions to range-dependent problems in ocean acoustics e.g., the difficulty in handling out of plane scattering effects. Notwithstanding these limitations, our solution based on idealized geometry reproduces the essential physics of the problem and can be used as an approximate solution for more realistic geometries.

The total diffracted field power is divided between the portion carried by the radiating cylindrical wave and the portion carried by the coupled subsonic flexural wave. The latter is defined here as

$$\Pi_{flex} = \int_0^{\infty} \langle I_x \rangle dy \tag{4.94}$$

where $\langle I_x \rangle$ is the x-component of the intensity vector as derived from Eq.(4.74). The y-component of the intensity is imaginary for the flexural wave and thus there is no energy radiating across planes parallel to the $x = 0$ surface. The total diffracted field power consists of the two terms

$$\Pi_D = \Pi_{Dcyl} + \Pi_{flex} \tag{4.95}$$

where Π_{Dcyl} is based on the precise definition of integrated Fraunhofer far field intensity discussed in Chapter 3.

We define a measure of the energy partitioning between Π_{Dcyl} and Π_{flex} as

$$\sigma_p = 10 \log_{10} \frac{\Pi_{Dcyl}}{\Pi_{flex}} \tag{4.96}$$

in dB. The value of σ_p is plotted against grazing angle α in Fig. 4.10 for diffraction from 2 m-thick ice layer with the incident field frequency at 50 Hz. We see that this ratio increases with grazing angle starting at about 26 dB. Furthermore, we will find this value to be in excess of 20 dB for all examples pertaining to sea ice and low-frequency acoustics, and therefore we may ignore the power carried by the coupled flexural wave in the ice lead diffraction process. This is not surprising considering the large disparity between the phase speed of the coupled flexural wave, e.g. 616 m/s for 50 Hz and H =2m, and the ambient medium phase speed of about 1450 m/s

In the following examples we compare the diffracted power Π_{Dcyl}, which we now refer to as the total diffracted power, with the corresponding value of total diffracted power derived from the equivalent locally reacting surface, i.e., the semi-infinite ice sheet consists of a layer of H m and density $\rho_2 = 920 \text{kg/m}^3$. Figure 4.11(top) shows the effect of the grazing angle α on total diffracted power for a 2 m-thick ice layer with the incident field frequency at 50 Hz. There is $\sin^2 \alpha$ ($\sim \alpha^2$ for $\alpha \lesssim 20^o$) dependence evident in this figure as indicated by the dotted line.

Next we examine the effect of frequency; for this we fix $H = 1$m, $\alpha = 15^o$ and span the range $fH = 1$ to 150 Hz-m. (We do not consider the limit of $f \rightarrow 0$ Hz because gravitional

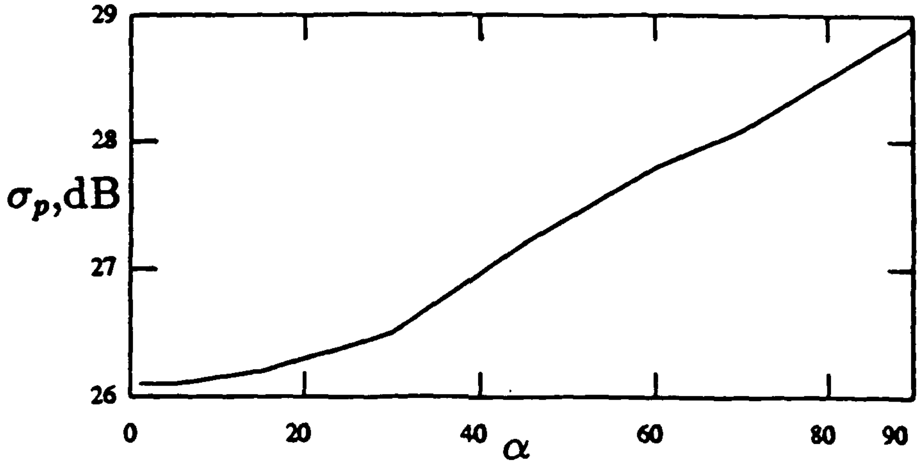

Figure 4.10: The ratio of cylindrical wave power $\Pi_{D_{cyl}}$ to coupled flexural wave power Π_{fles} in terms of σ_p, as a function of grazing angle α

effects would become important in Eq.(4.13) for frequencies below .3 Hz [68].) The results in Fig. 4.11(middle) show a negligible difference between the local reaction case and the extended reaction case for $fH \lesssim 50$, and indicates a clear linear dependence of Π_D on frequency at least for the locally reacting case. Finally we examine the effect of ice thickness H; for this we fix the frequency at 30 Hz, $\alpha = 15^\circ$ and again span the range $fH = 0$ to 150 Hz-m. The results in Fig. 4.11(bottom) also show a negligible difference between the two cases for $fH \lesssim 50$, but the dependence on H is clearly non-linear.

Let us now study these results using the equivalent locally reacting ice surface as a guideline. In Chapter 3 we showed that the material properties of the semi-infinite surface modified the diffracted field ϕ_D via the rather complicated material function $M(\beta)$ [Eq.(3.31)], and the θ-dependence of a *field point* assumed the form $M(\theta)P(\theta)$. On the other hand, in the course of checking the boundary conditions we determined that the material properties of the semi-infinite surface modified a *boundary point* by the simple

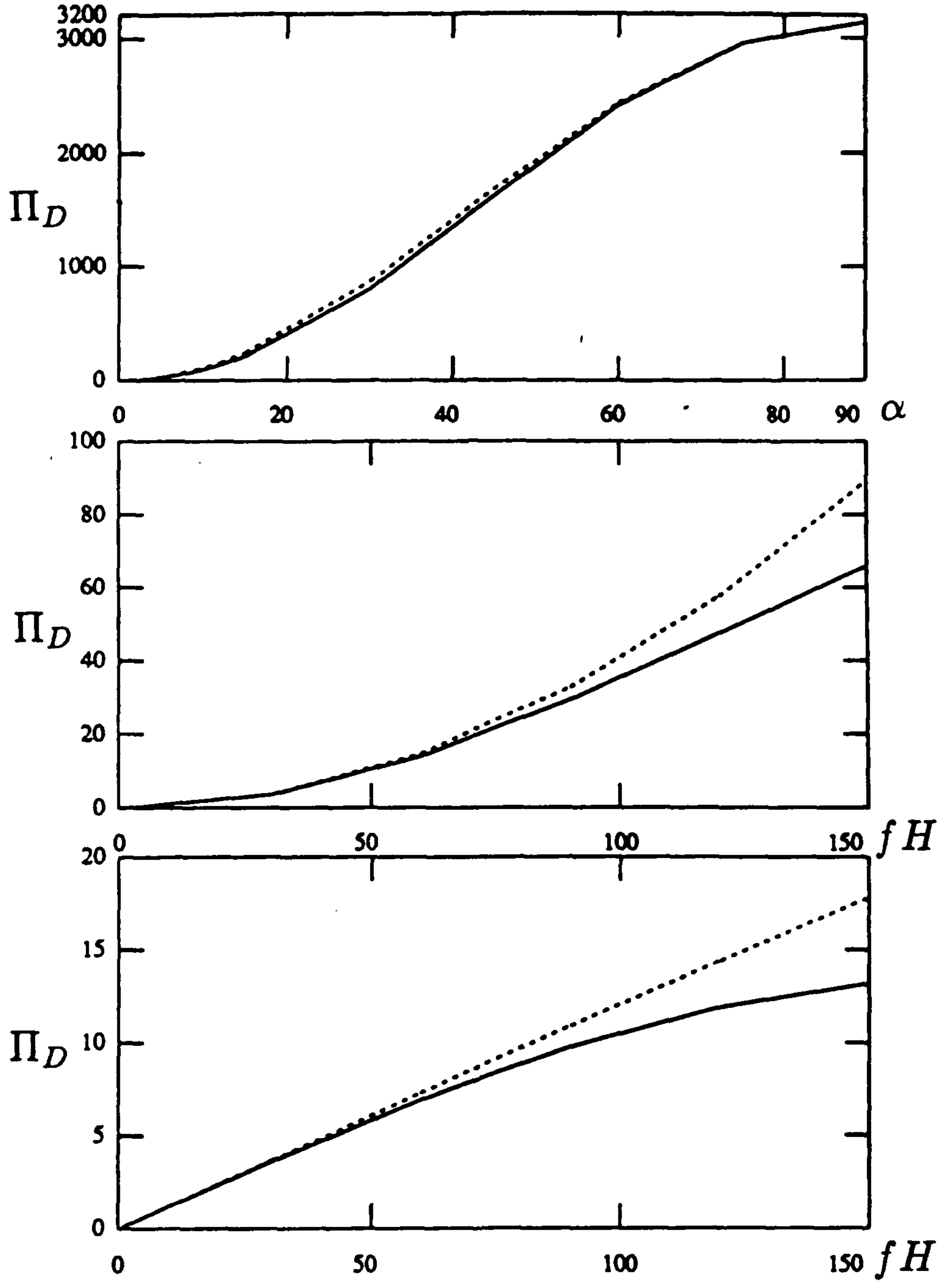

Figure 4.11: Total diffracted power for extended reaction case (solid line) and local reaction case (dashed line). top: as a function of grazing angle α, middle: as a function of frequency with H = 1m, bottom: as a function of H with frequency =30 Hz.

expression $1 + R$ [for example, cf. Eq.(3.41)].

From Green's theorem, the integral of the values of ϕ_D and its normal derivative along the boundary uniquely determine the value of ϕ_D for a field point. This integral is of the form [59]

$$\phi_D(\vec{r}) = \frac{1}{4\pi}\int_{S_0}[g(\vec{r},\vec{r_0})\frac{\partial\phi_D(\vec{r_0})}{\partial n_0} - \frac{\partial g(\vec{r},\vec{r_0})}{\partial n_0}\phi_D(\vec{r_0})]dS_0 \tag{4.97}$$

where $g(\vec{r},\vec{r_0})$ represents a two-dimensional Green's function and $\vec{r},\vec{r_0}$ are the respective field and boundary coordinates; the integration along the boundary S_0 is along the planar interface $y = 0$ in our case. A suitable Green's function for our problem is the Hankel function which satisfies the free surface boundary condition, and which we emphasize has no dependence on the material properties of the boundary surface. Therefore, we can say quite generally that the diffracted field behavior is

$$p_D(r,\theta) = (1+R)F(\theta)\frac{e^{ikr}}{\sqrt{kr}} \tag{4.98}$$

for a field point in the Fraunhofer far field. Here $p_D(r,\theta)$ is the diffracted field pressure and $F(\theta)$ is some general far field radiation pattern *independent* of material properties and frequency, which we do not specify further. Thus we have

$$\Pi_D = .5Re[(1+R^*)(1+R)]\frac{1}{k}\int|F(\theta)|^2d\theta \tag{4.99}$$

where the integration is assumed to be over the Fraunhofer region. This tells us that

$$\Pi_D \sim \frac{1+Re(R)}{k} \tag{4.100}$$

with

$$R = \frac{-i\omega\rho_1 H - \frac{\rho\omega}{k\sin\alpha}}{-i\omega\rho_1 H + \frac{\rho\omega}{k\sin\alpha}}. \tag{4.101}$$

We now observe that

$$1 + Re(R) = \frac{2(\omega\rho_1 H)^2}{(\omega\rho_1 H)^2 + (\frac{\rho\omega}{k\sin\alpha})^2} = \frac{2(\omega\rho_1 H)^2}{(\frac{\rho\omega}{k\sin\alpha})^2} + O[(kH\sin\alpha)^4] \tag{4.102}$$

giving a parametric dependence for the total diffracted power from a locally reacting surface as

$$\Pi_D \sim (\frac{\rho_1}{\rho})^2 kH^2\sin^2\alpha. \tag{4.103}$$

Equation(4.103) fully explains the above results for the locally reacting case, for example, the $\sin^2\alpha$ behavior of Fig. 4.11(top), the linear dependence on frequency in Fig. 4.11(middle), and the kH^2 dependence in Fig. 4.11(bottom). If $fH \lesssim 50$ then Eq.(4.103) nearly fully explains the results for the extended reaction case, which means this fH range is almost entirely dominated by mass loading effects as far as the ice lead diffraction process is concerned.

For $fH \lesssim 50$, the results for the extended reaction case begin to diverge from the basic dependencies described in Eq.(4.103). But, knowing the flexural wave carries only a small fraction of the total diffracted power, we can also proceed with the same Green's theorem arguments as in the local reaction case, using for the reflection coefficient

$$R = \frac{-i\omega\rho_1 H[1-\xi(kH)^2] - \frac{\rho\omega}{k\sin\alpha}}{-i\omega\rho_1 H[1-\xi(kH)^2] + \frac{\rho\omega}{k\sin\alpha}} \tag{4.104}$$

where $\xi \approx .33$ as discussed earlier. This gives a parametric dependence for the total diffracted power from an elastic ice (thin plate) surface as

$$\Pi_D \sim (\frac{\rho_1}{\rho})^2 kH^2 \sin^2\alpha[1-2\xi(kH)^2] + O[\xi^2(kH)^4, (kH\sin\alpha)^4]. \tag{4.105}$$

Equation(4.105) provides the necessary correction for the effects of elasticity. For example, at 30 Hz with H =5m, $2\xi(kH)^2 = .28$ and this value accounts for the difference between the local and extended reaction cases at $fH = 150$ *in Fig. 4.11(bottom); this difference* being ≈ 1.3 dB.

Thus far our work has been limited to the $fH \lesssim 150$ range or $kH \lesssim .65$. We took this value from ref.[68] because it represents the range for which the coupled flexural wavenumber for an ice plate can be accurately derived from the thin plate equation. We would like to extend this range, knowing the accuracy of the coupled flexural wavenumber will be diminished. But our purpose here is to provide a first order correction for the effects of elasticity in the ice lead diffraction process. As a guide for this we use a traditional bound for the application of the thin plate equation in structural acoustics [43] which is $k_fH \lesssim 2\pi/5$. Using the typical sea ice physical parameters, this is equivalent to $fH \lesssim 250$ or $kH \lesssim 1$ which defines a less conservative range of applicablity for our results. We note that $fH \lesssim 250$ keeps us well below the coincidence frequency $fH \approx 375$ [from Eq.(4.3)], a frequency considered by some to be too high to apply thin plate theory [27].

As a final note before ending our analysis of a plane wave incident upon a semi-infinite elastic plate, we consider the reciprocal problem as defined by a plane wave incident from the opposite direction. Recall that the Wiener-Hopf kernel $K(q)$ is an even function of q, for both the local and extended reaction cases. We successfully decomposed this kernel such that $\hat{K}_-(q)\hat{K}_+(-q) = 1$, which is a property of even functions and is related to the the reciprocity condition [64]. Thus, for example, if we set up our problem in the opposite sense: with the plate boundary condition for $x < 0$ and free surface boundary condition for $x > 0$, we end up with the same kernel, but now find that a pole at $q = -\bar{k}_f$ is captured for $x < 0$ (rather than $q = -\bar{k}_f$ for $x > 0$), representing a coupled subsonic flexural wave travelling in the left direction. Furthermore, the boundary behavior of ϕ_D will now be governed by $(-R - 1)$, rather than $(1 + R)$ as before, but the total diffracted power remains the same.

4.6 Summary

We have examined in detail the problem of a low-frequency monochromatic plane wave incident upon a free surface coupled to a semi-infinite elastic surface, focussing on sea ice as the elastic surface. The elastic behavior of the sea ice was modeled by the thin plate equation. A key issue here is the fluid loading pertaining to sea ice and low-frequency acoustics, which cannot be characterized by simplifying heavy or light fluid loading limits. Using an approximate kernel for the Wiener-Hopf equation, valid in this mid-range fluid loading regime, we proceeded to a complete and interpretable solution of the diffraction problem.

We determined that the amount of power carried by the cylindrical spreading portion Π_{cyl} of the diffracted field to be in excess of 20 dB greater than that carried by the coupled subsonic flexural wave Π_{flex}, and therefore the latter can be ignored in the low-frequency ice lead diffraction process. By applying Green's theorem to the properties of the diffracted field along the boundary, we derived the primary functional dependencies of the diffracted power on k, H and grazing angle α, and the ice elastic properties as characterized by the parameter ξ.

Chapter 5

Demonstration of a mechanism for propagation loss associated with the ice lead diffraction process

In Arctic regions long range oceanic sound propagation is governed by an upward refracting sound speed profile which gives rise to an acoustic channel bounded from above by the Arctic ice canopy. The efficiency of long range acoustic propagation, and thus the use of the Arctic ocean as a communication channel, is significantly influenced by sound interacting with the complex ice-covered surface.

The effects of this interaction is the subject of considerable research effort focussing on various characteristics of the ice-covered surface. For example, the effects of a stochastically rough elastic ice interface have been studied using a perturbation method, in order to understand the combined effects of ice elasticity and roughness [45]. Scattering of low-frequency narrow band pulses from ice keels has been examined using a numerical approach based on the finite difference method [28], and acoustic scattering from a point source below an open lead has been studied from the viewpoint of laboratory scale model experiments [52].

The overall effect of the ice surface on sound transmission is due to a combination of mechanisms, depending on acoustic frequency and Arctic environment. For example, the under-ice roughness will be less influential at low frequencies where the acoustic wavelength is much greater than the rms roughness of the ice surface; or the ice canopy in the central Arctic is considered contiguous with few open leads, in contrast to the time-varying, partially ice-covered surface characteristic of marginal ice zone regions. Our work has application to partially ice-covered marginal ice zone waters, and, in particular, to the study of diffraction effects from the open leads and polynya.

Thus far in this thesis we have viewed the ice lead diffraction process from the standpoint of diffraction of an acoustic plane wave from a free surface coupled to a semi-infinite elastic surface. The analysis led to a determination of total diffracted power Π_D, and its prime descriptors k, H and grazing angle α. Our primary goal in this chapter is to convert these results, in a simple yet relevant manner, for the purpose of demonstrating a mechanism for acoustic propagation loss attributed directly to the ice lead diffraction process.

The framework of this demonstration is a set of long range acoustic propagation data from MIZEX84 (marginal ice zone experiments, June-July 1984), but we emphasize that we cannot depend on conclusive agreement between theoretical values and experimental data. Too many important parameters, such as ice floe size and concentration, enter the problem in the form of only nominal estimates. Furthermore, our analytic results can only address a small subset of this experimental data. We will, however, indicate a discrepancy between available theory and experimental data, and show that ice lead diffraction effects are a plausible mechanism to account for this discrepancy.

The experimental data are in the form of continuous wave (cw) acoustic signals which were transmitted between two ships separated by approximately 100 km, and propagated via a partially ice-covered path. The signals were stepped in frequency between 25 and 200 Hz, with each tone lasting 1 h. The acoustic environment was characterized by generally upward refracting range variable sound speed profiles, an undulating bottom of mean depth of about 700 m, and a variable ice cover. The overall complexity and range variation of the acoustic channel is depicted by contours of sound speed using sound-speed profiles every 15 km during the course of the experiment [56] (Fig. 5.1). The acoustic signals analyzed here were received by a vertical array with six receivers between 72 and 265 m, with the source being at 78 m depth. The primary data reduction, from received signal to acoustic

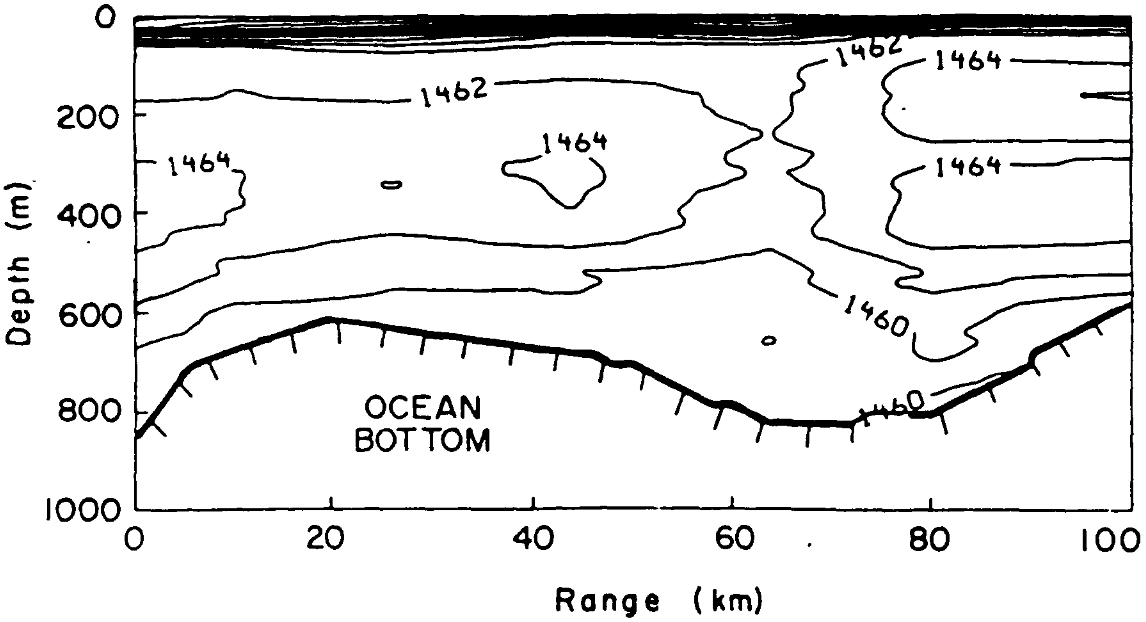

Figure 5.1: Contours of sound speed from data taken every 15 km. The sound speed changes from approximately 1440 to 1460 m/s, within the top 50-m near-surface channel. Bold black line denotes the bathymetry. Acoustic source (R/V POLAR QUEEN) is at range 0 km and vertical receiving array (R/V KVITBJØRN) is at range 100 km.

transmission loss (TL) in dB referenced to 1 m, is documented in ref.[23].

5.1 Transmission loss analysis based on the ray average method

Our approach is to examine the MIZEX84 data using ray theory, and view the problem in terms of a dB loss for each ray interaction with the partially ice-covered surface. Essential to this approach is an accurate estimate of geometrical spreading loss, which must be frequency independent. We begin by computing the depth-averaged geometrical spreading loss, or background loss component of total transmission loss, using the ray average method [66,25]. The depth average is from the surface to D_e, or effective depth [25], which we define

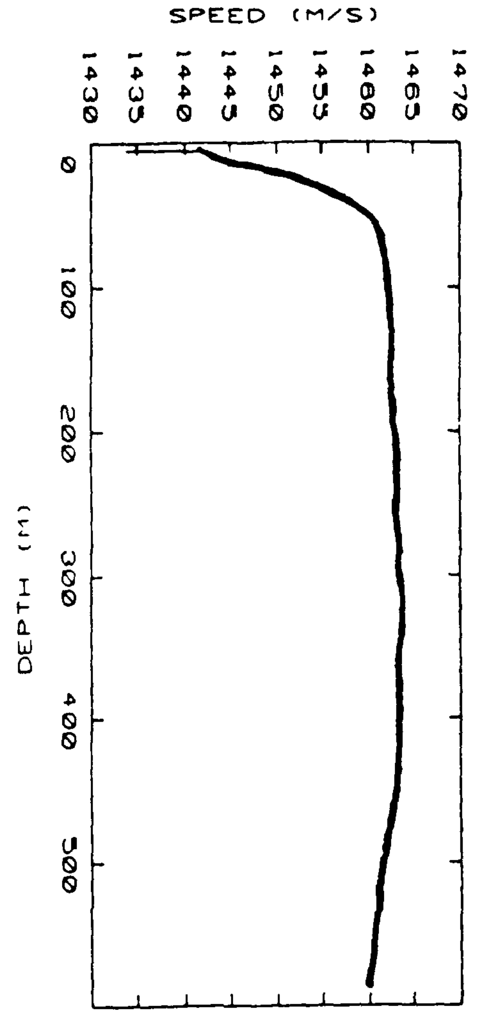

Figure 5.2: Range independent (ensemble averaged) sound speed profile used in the ray average method.

subsequently. In order to use the ray average method we ensemble average in range the original sound speed profile data on which Fig. 5.1 is based, and work with a smoothed, range independent profile in Fig. 5.2.

The effective depth D_e of the acoustic channel is the depth above which all rays follow refracted paths confined to the water column (RSR paths). Rays passing below D_e interact with the bottom (BB paths), and it is assumed that because of higher attenuation this contribution is neglected from the sound field calculation. We will find that this assumption limits the frequency range of the experimental data available for this kind of analysis. Nevertheless, the simplicity of our approach has merit, enabling us to succeed in converting

depth m	sound speed m/s	angle from horizontal
surface	1441.0	10.2^o
50	1460.0	4.2^o
78	1461.6	3.3^o
100	1462.1	2.9^o
300	1464.0	0^o

Table 5.1: Set of horizontal ray angles used in the ray average method.

our results without introducing further complexity. In choosing D_e we observe that the maximum sound speed for the range-averaged profile in Fig. 5.2 occurs at approximately 300 m, with a tendency for slight downward refraction below this depth. Furthermore, the experimental data above 85 Hz tend to have measured pressure levels which taper off by 2-5 dB for the deepest receiver at 265 m depth. We thus set $D_e \approx 300$ m as a nominal value, which also spans the entire length of the vertical array.

The next step is to determine the source launch angle θ_L such that all rays with launch angle θ satisfy $|\theta| < \theta_L$. From Table 5.1 we find θ_L=.057, where we have assumed a linear sound speed gradient between each depth listed in the table. The values in Table 5.1 are computed by starting with a ray which reaches a vertex at 300 m and tracing this ray to the surface. The depth-averaged geometric spreading loss derived from the ray averaged method is

$$TL = 10\log R + 10\log D_e - 10\log 2\theta_L \tag{5.1}$$

and is 84 dB for R =100 km. This becomes our background loss value to which additional losses will be added. Associated with our ray model is a nominal cycle distance for the vertex ray which is approximately 16 km. This ray interacts with the surface approximately six times, with a grazing angle $\alpha \approx 10^o$.

In working with a range-averaged sound speed profile, we eliminated a prominent range-dependent aspect from the problem. To assess the significance of this, we also compute a depth-averaged geometrical spreading loss using the parabolic equation (PE) method [40]. The PE analysis takes into account the lateral heterogeneity in sound speed and bathymetry as shown in Fig. 5.1. The ocean bottom is modeled as a fluid halfspace with compressional sound speed 1600 m/s, density 1500 kg/m^3 and an attenuation of .5 db/λ. No other loss

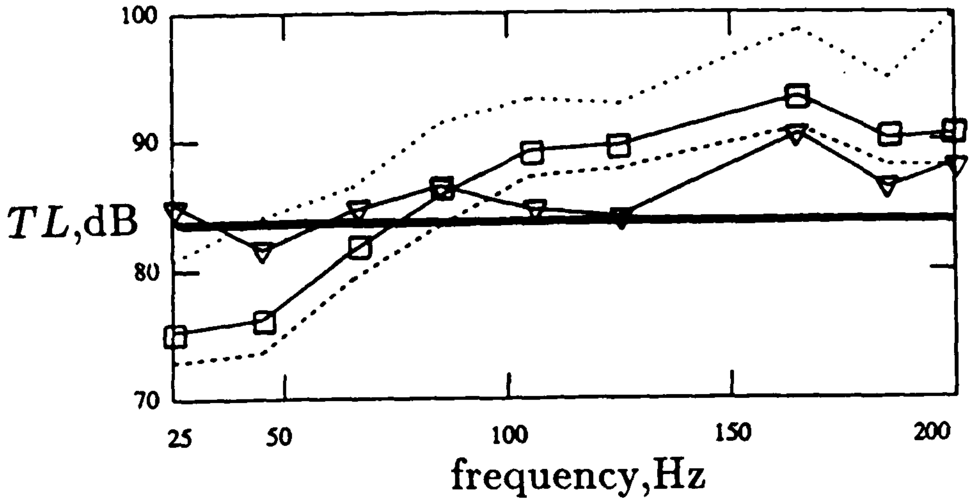

Figure 5.3: Transmission loss in dB ref. 1 m. The solid line through square symbol connects mean values of MIZEX84 experimental data for discrete frequencies. The solid line through triangle symbol connects mean values derived from the PE method. For clarity the data spread, as indicated by the dotted line, is shown only for the experimental data; a similar data spread exists about the mean values derived from the PE method. Bold solid line at 84 dB is the frequency independent value derived from the ray average method.

mechanisms are incorporated; our purpose here is only to compare with, and lend credence to, the 84 dB value derived from the ray average method. It is important that the 84 dB background loss value not be encumbered by a large and unknown variance, since we want to distinguish the background loss from losses attributed to ice lead diffraction and other relevent losses.

The PE sound propagation model gives TL as a function of depth, at range 100 km for a 78-m source depth. The TL values are converted to linear intensity, and the latter are averaged over the depth range 72-265 m to obtain an estimate of depth-averaged geometrical spreading loss. The measured transmission loss values for the six receivers spanning the vertical array are also averaged in the same manner. Both data sets are reported in dB referenced to 1 m, and thus pertain to the log of the mean transmission loss for the channel with $D_\ell \approx 300$ m. These values are summarized in Fig. 5.3, with the frequency independent ray theory value represented by the line at 84 dB.

Data of this nature are always accompanied by a substantial spread about the mean value. For both data sets this spread is approximately −2 dB and +4 dB about the mean value. The asymmetrical spread is introduced by taking the logarithm of the mean depth-averaged intensity ±1 standard deviation, which serves as a useful measure of variability [15]. We also note there may be an additional spread in the experimental data on the order of ±1.5 dB, originating from the uncertainties in source level and hydrophone receiving sensitivities.

We accept the large spread in the data, but now focus on the mean values as shown by the solid lines. A basic assumption in our demonstration is that the background loss as computed by the ray average and the PE methods should be less than the corresponding measured loss. This assumption is correct for frequencies greater than about 85 Hz, where at 85 Hz the PE and measured data lines reach a cross-over point. One may conclude that the strong near-surface gradient is of less importance and bottom propagation plays an increasing role in these waters for frequencies $\lesssim$ 85 Hz. This in turn would require more accurate bottom modeling for the PE method to provide useful estimates of background loss in this frequency range, an endeavor we do not wish to undertake since bottom modeling introduces additional unknown parameters, and bottom propagation paths are not consistent with the effective depth concept. For the same reason, the frequency range $\lesssim$ 85 Hz also represents a departure from the ray theory value, in that the 84 dB background loss is now greater than the measured data. Thus we consider frequencies $\lesssim$ 85 Hz to be below the range necessary to isolate a geometrical spreading loss estimate based on the effective depth concept, with sufficient certainty for our purposes.

The higher frequencies are reported for completeness, but these frequencies are beyond the limits in applying the thin plate approximation to the ice surface, if $H \gtrsim 2$ m. Furthermore, although the PE data continues to track the experimental data with an offset, a frequency-independent background loss assumption does not hold here, presumably due to range-dependent oceanographic features which have begun to influence acoustic propagation. For these reasons we limit the subsequent analysis to the 105 and 125 Hz data, where we can use the 84 dB background loss value with confidence.

5.2 Conversion of Π_D to dB loss per bounce

In order to carry through the conversion of Π_D to an estimate of dB loss per bounce, we require a nominal estimate of the incident power Π_I. In the usual modifications to ray theory to account for acoustic interaction with a boundary, one assumes the field behaves locally as a plane wave and the plane wave reflection coefficient provides the necessary modification of the field. We proceed with the local plane wave assumption, but in our case the incident power depends upon the range extent l_p of the interacting bundle of rays. One can obtain a nominal estimate of l_p from the principle of rays being the superposition of modes of neighboring orders, and the relationship between modal cycle distance and ray cycle distance. From such arguments one obtains [69]

$$l_p \approx \frac{\pi}{k\alpha^2} \tag{5.2}$$

and therefore a nominal estimate of the incident power is

$$\Pi_I \approx \frac{.5}{\rho c} \sin\alpha \;\; l_p. \tag{5.3}$$

The power balance established in Chapter 3 is

$$\Pi_I = \Pi_R + \Pi_D \tag{5.4}$$

and writing $\Pi_R = |R|^2 \Pi_I$ we can express Eq.(5.4) as

$$|R|^2 = 1 - \frac{\Pi_D}{\Pi_I}\bar{n}. \tag{5.5}$$

In the above $|R|^2$ is the squared modulus of the coherent reflection coefficient for a partially ice-covered surface, which is diminished by edge diffraction processes, and the dB loss per bounce estimate we seek is $20\log|R|$. Note that we assume $|R|^2 = 1$ in the absence of diffraction effects. The constant $\bar{n}$ is included here in an ad hoc manner, for the purpose of weighting Π_D according to ice floe size and concentration. We estimate $\bar{n}$ subsequently, but two remarks are in order before continuing.

First, our idealized two-dimensional geometry presumes that an ice lead diffracts approximately as a lineal element, an assumption being recognized by others [52]. This means the diffracting edge is effectively of infinite extent in a direction perpendicular to the x, y

plane. Let us call this extent of the ice lead L; but the effective lateral extent depends on the field point of the receiver. That is, if $L \gg 2\sqrt{r\lambda}$, where r is a field point from which pressure is measured, then the diffraction process can be considered approximately two-dimensional, and the diffracted pressure far field behaves as a cylindrical wave with $1/\sqrt{kr}$ range dependence as we have determined. This follows from the extent L being much greater than the radius of the first Fresnel zone of the receiver, and thus it can be considered effectively of infinite extent [67]. Since our diffracted far field behavior applies for $kr \gg 1$, this is equivalent to $L \gg 2\lambda/\sqrt{2\pi}$, which is a reasonable criterion to satisfy. From Chapter 3, however, we found it convenient to consider kr very large (e.g. $kr = N \approx 1000$ or more) in order to numerically integrate the diffracted intensity and arrive at the total diffracted power Π_D, and we see that this now requires $L \gg 2\lambda\sqrt{\frac{N}{2\pi}}$ in order to preserve the same two-dimensional geometric divergence of the diffracted field. For now we accept this as a drawback in our approach to computing Π_D, and we refer to some new techniques for studying diffraction from edges with finite extent in Chapter 6.

Our second remark concerns the semi-infinite approximation for the range extent of the ice floe in the x-direction. In Chapter 4 we showed that along the boundary at range $x = l \gtrsim \lambda$, the diffracted field has diminished in excess of 24 dB. This suggests that when two diffracting edges are involved, with separation l_i such that $kl_i \gg 1$, a natural first approximation is to consider each edge as arising from separate half-planes [59]. In this demonstration we will find it likely that more than one edge can be ensonified, for example, both leading and trailing type edges separated by l_i (ice range extent) or l_w (free surface or water range extent). In these cases we add the individual edge diffracted powers incoherently and ignore the interaction field [59] due to the proximity of the diffracting edges, where the interaction field is $O(1/k\sqrt{dr})$ and $d = l_i$ or l_w.

5.2.1 Disk model for partially ice-covered surface

Our final task is to estimate $\bar{n}$ which depends on the characteristic size of the ice floes and concentration. An elaborate probabalistic model is not warranted here; we are simply after some reasonable mean values of l_i and l_w which we denote as $\bar{l}_i$ and $\bar{l}_w$. For this purpose we have adopted a model used to study ice floe collisions for floe fields typically encountered

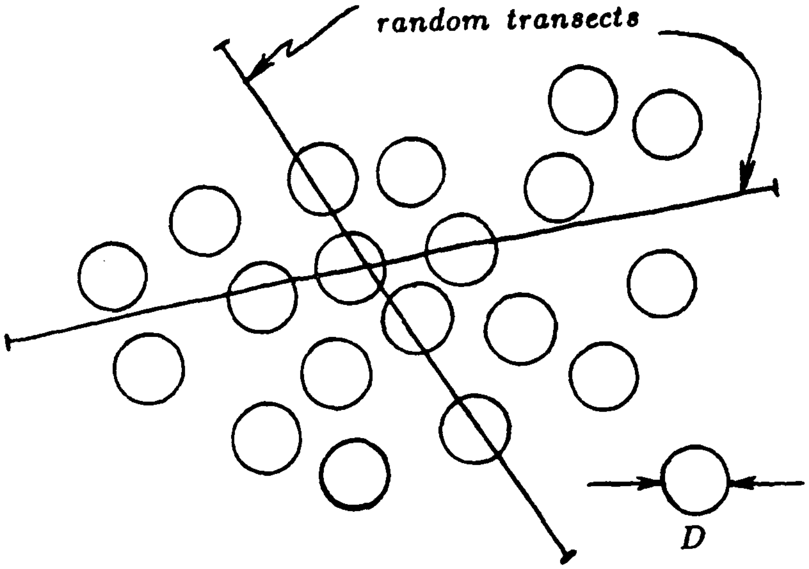

Figure 5.4: Isotropic distribution of uniform disks of characteristic diameter D, sampled by a random transect.

in the marginal ice zone [65].

In this model the ice floe field is viewed as an isotropic distribution of identical disks (Fig. 5.4). For our problem a random transect across this idealized floe field will intersect N floes/unit length in total range, with

$$N = \frac{4}{\pi}\frac{C}{D} \tag{5.6}$$

where D is the floe characteristic diameter and C is the percent of surface ice coverage. The random transect bisects each floe such that the mean range extent of an ice floe as sampled by the transect is the mean chord length, giving

$$\bar{l}_i = \frac{\pi}{4}D. \tag{5.7}$$

We now have the necessary information to produce a nominal estimate of the likelihood of ensonifying an ice floe leading or trailing edge, which we do in the following example. The characteristic diameter for ice floes in the vicinity of the MIZEX84 acoustic transmission experiment was approximately 100 m [51]; thus we set $D \approx 100$m. The ice coverage varied on a daily basis; on the day these measurements were taken (19 June, 1984) the coverage was approximately 30% as determined by microwave remote sensing [10], and therefore we set $C \approx .3$. The number of floes intersected in the 100 km transmission path was therefore

$$\frac{4}{\pi}\frac{C}{D}100 \approx 382. \tag{5.8}$$

From Eq.(5.7) the mean range extent of an ice floe along the transect is $\bar{l}_i \approx 79$ m or $k\bar{l}_i \approx 36$ for 105 Hz. We derive an estimate of the mean water-covered extent from $\bar{l}_i$ and the concentration, giving $\bar{l}_w \approx 183$ or $k\bar{l}_w \approx 83$ for 105 Hz. At this floe size and concentration the diffracting edges are sufficiently separated to apply our semi-infinite approximation and we consider each leading and trailing edge as a separate diffraction feature and add the diffracted powers incoherently.

The total number of diffraction features per m is 2·382/100 km=.0076, and the mean number of features $\bar{n}$ ensonified during each interaction with the surface is given by

$$\bar{n} \approx l_p \quad .0076. \tag{5.9}$$

We determined the nominal grazing angle to be $\alpha \approx 10°$, and using Eq.(5.2) $l_p \approx$226 m for 105 Hz, we arrive at $\bar{n} \approx 1.72$.

The ice floe thickness in the region varied from 1 to 5 m, with the peak of sample density functions near 2 m [31], and therefore we use $H \approx 2$ m in order to compute Π_D in the manner described in Chapter 4. Our estimate for dB loss per bounce is finally computed from

$$-10\log(1 - \frac{\Pi_D}{\Pi_I}\bar{n})$$

which is .7 dB at 105 Hz. The total loss due to diffraction depends on the number of ray surface interactions; from the ray average method we estimated this number to be six, thus giving a total diffraction loss $\approx$ 4 dB. For 125 Hz, $l_p \approx 190$ m giving $\bar{n} \approx 1.44$ and a total diffraction loss $\approx$ 3.3 dB. (Note that use of $\bar{n}$ *inside* the logrithm, is consistent with presenting the logarithm of the mean transmission.)

We next take inventory of other loss mechanisms contributing to the total transmission loss. For volumetric absorption we use an empirical result which applies to sub-Arctic waters [9] giving δ_1 =.002 dB/km at 105 Hz and .003 dB/km at 125 Hz. Volume scattering loss from ocean dynamical features such as eddies and fronts is estimated from [54] using ocean dynamical parameters for the marginal ice zone given in [26]. The parameters are $\mu^2 \approx 2.5\ 10^{-5}$, which is the rms spatial contrast in index of refraction, and $L_o \approx 10$km, which is the spatial scale of the ocean feature. These give $\delta_2 = .015$ dB/km or about 1.5 dB for 100 km as a frequency-independent value.

The majority of theoretical estimates of loss due to ice roughness are based on a randomly rough ice-water interface, where the rms roughness and correlation length is assumed known. It is unclear how the open water areas in the marginal ice zone affect the statistical stationarity assumptions inherent in these estimates. For our purposes, we adopt $\delta_3 = f^{1.5}$ db/km [55], where f is frequency in Hz, as a nominal estimate, and assume an *effective range* for loss due to ice roughness which is approximately equal to the ice concentration percentage of the total range. Thus, for example, $\delta_3 = .051$ dB/km at 105 Hz, which we apply to an effective range of 30 km for $C \approx .3$, giving a total loss due to roughness of about 1.5 dB.

The additional losses attributed to the ice lead diffraction process (DL), volume scattering loss (VL), ice surface roughness (SRL) and volumetric absorption loss (AL), are summarized in Table 5.2 for 105 and 125 Hz. These are added to the 84 dB background loss for an estimate of total transmission loss (est. TL). Included is a likely range of ice concentration and floe sizes, with our best estimate ($C \approx .3, D \approx 100$ m) in the top entry. Our estimated TL at 105 and 125 Hz compares favorably with the measured transmission loss (meas. TL) when $C \approx .3$. We emphasize, however, that the floe concentration and size estimates are only nominal values, and we do not have a proper statistical, or "ground truth", description of the overall ice conditions. We also admit to being fortunate in that the ice floe concentration was relatively low on the day of the experiment. Had the ice concentration been greater, e.g. $C \gtrsim .75$, we could not justify the conditions $k\bar{l}_i, k\bar{l}_w \gg 1$, a necessary condition to convert our values of Π_D to a diffraction loss estimate.

For completeness we plot in Fig. 5.5 the DL for the entire frequency range 25-125 Hz using $H = 2$m and the same range of floe sizes and ice concentrations. We observe an interesting maximum in DL at about 85 Hz. Let us recall Eq.(4.105) giving the parametric dependence for total diffracted power from a semi-infinite elastic half-plane. Using the small

conc/size C/D	freq	DL	VL	SRL	AL	est. TL	meas. TL
.3/100	105 Hz	4.1	1.5	1.5	.2	91	89
	125 Hz	3.3	2.0	1.5	.3	91	90
.3/200	105 Hz	2.0	1.5	1.5	.2	89	89
	125 Hz	1.6	2.0	1.5	.3	89	90
.5/100	105 Hz	7.4	2.6	1.5	.2	96	89
	125 Hz	5.8	3.3	1.5	.3	95	90
.5/200	105 Hz	3.4	2.6	1.5	.2	92	89
	125 Hz	2.7	3.3	1.5	.3	92	90

Table 5.2: Additional losses in dB attributed to ice lead diffraction (DL), volume scattering (VL), ice surface roughness (SRL) and volumetric absorption (AL), which are added to an 84 dB background loss.

angle approximation for grazing angle α, we write this dependence as

$$\Pi_D = \Delta_1 k H^2 \alpha^2 [1 - 2\xi(kh)^2] \qquad (5.10)$$

where Δ_1 is a constant we need not specify further, and the parameter $\xi = .33$ which relates to the properties of the sea ice and ambient medium. The dB loss per bounce estimate takes the form

$$-10 \log\{1 - \frac{\Delta_1 k H^2 \alpha^2 [1 - 2\xi(kh)^2] \tilde{n}}{\frac{.5}{\rho c} \alpha l_p}\}.$$

Since $\tilde{n}$ is proportional to l_p, the above simplifies to

$$f(k) = -10 \log\{1 - \Delta_2 k [1 - 2\xi(kH)^2]\} \qquad (5.11)$$

where all frequency-independent constants are absorbed into the constant Δ_2. Finally, by taking the derivative with respect to k of Eq.(5.11), we find a local maximum at

$$k = \frac{1}{\sqrt{6\xi}} \frac{1}{H} \qquad (5.12)$$

which translates to approximately 85 Hz for H =2 m. Equation(5.12) may prove useful in considering the acoustic channel filtering properties for partially ice-covered waters.

5.3 Summary

In this chapter we tied together earlier results for total diffracted power Π_D, with numbers C and D representing ice floe concentration and characteristic size, respectively. The result

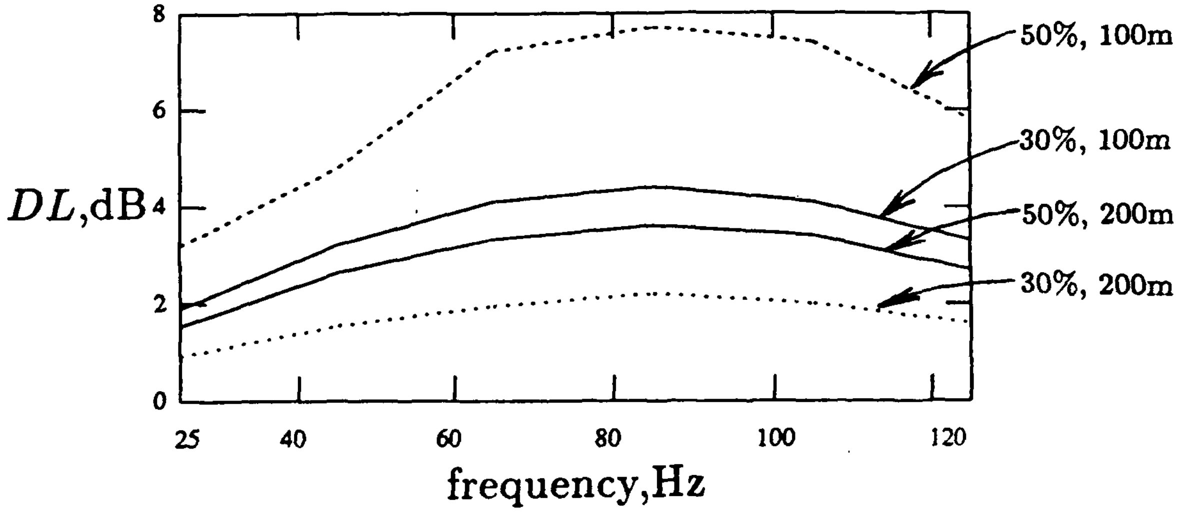

Figure 5.5: Estimated DL as a function of frequency for 100 km range and 2-m nominal ice thickness. Each line represents a different combination of ice coverage percent and ice floe characteristic size.

was converted to an estimate of acoustic transmission loss attributed directly to the ice lead diffraction process (DL). This component of total transmission loss was compared to components attributed to volumetric scattering (VL), ice surface roughness (SRL), and volumetric absorption (AL). Analysis of acoustic propagation data from MIZEX84 indicated a discrepancy between available theory and measured values for 100 km transmission loss. Subsequent comparison of the MIZEX84 data with transmission loss values derived from the ray average method was limited to the data at 105 and 125 Hz, and it was shown here that ice lead diffraction effects are a plausible mechanism to account for this discrepancy.

Chapter 6

Conclusions and suggestions for future research

In this thesis we have examined in detail the essential physics of the acoustic diffraction process due to a plane wave interacting with a two-part planar surface characterized by different boundary conditions. We have focussed on a free surface coupled to an ice-covered surface for the purpose of understanding the effects of diffraction from ice leads in long range acoustic propagation.

We began in Chapter 2 by deriving an exact solution to a canonical problem concerning diffraction from a free surface coupled to a perfectly rigid surface. The exact solution to this particular problem has not been shown before. The solution is derived from the Wiener-Hopf method which gave the Fourier transform of the diffracted field, and the inversion of this Fourier transform was facilitated by partitioning the diffracted field into component fields.

In Chapter 3 we argued the merits of a locally reacting approximation for the input impedance of an ice sheet for low frequencies, and the perfectly rigid surface was replaced by an ice surface characterized by a locally reacting finite impedance. Inclusion of the finite impedance boundary condition greatly complicated the kernel decomposition step in the Wiener-Hopf procedure. An approximate kernel, based on matching the moments of the exact kernel, was used here which enabled us to proceed to a complete and readily interpretable solution for the diffracted field ϕ_D. Important properties of ϕ_D were developed, such as its relation to $1 + R(\alpha)$, where $R(\alpha)$ is the ice reflection coefficient evaluated at grazing angle α, and a power balance among incident, reflected and diffracted fields was demonstrated.

The groundwork of Chapter 3 was utilized in Chapter 4 in the solution of the problem of a plane wave incident upon a free surface coupled to a semi-infinite elastic plate, which serves as a model for the ice lead diffraction process. The thin plate approximation for the ice impedance was shown to be a natural extension of the locally reacting approximation, with effects of ice elasticity being ignored in the latter. A new approximate kernel for the Wiener-Hopf solution technique was developed here. This kernel retains the properties of the coupled flexural wave, and is valid in the fluid loading conditions which pertain to sea ice and low-frequency acoustics ($kH \lesssim 1$). By using Green's theorem, in conjunction with behavior of the diffracted field along the boundary, we determined the dependence of total diffracted power Π_D on k (frequency), H (ice thickness) and α (grazing angle), in addition to the combined elastic properties of the ice sheet and ambient medium.

Finally in Chapter 5 we developed a means to convert Π_D into an estimate of dB loss per bounce, using an approach based on the ray average method. Our purpose here was to demonstrate a mechanism for acoustic propagation loss attributed directly to the ice lead diffraction process. As a framework for this demonstration, we analyzed a set of acoustic propagation data from MIZEX84. The analysis indicated a discrepancy between available theory and measured values for 100 km transmission loss, and it was shown that ice lead diffraction effects are a plausible mechanism to account for this discrepancy.

6.1 Suggestions for future research

In this thesis we pursued an analytic approach to the diffraction problem, which gave us additional insight into the mathematical and physical structure of the acoustic field due to range discontinuities. In particular, our focus on the solution of the water-to-ice planar diffraction problem using the Wiener-Hopf method has given us useful insights into the ice lead diffraction process. Our solution, with the problem framed in idealized two-dimensional geometry, is a logical first step to a more complete understanding of low-frequency acoustic interaction with a partially ice-covered surface. In the following we mention some research areas that extend from this work.

6.1.1 General oblique incidence

The two-dimensional geometry assumes the diffracting edge lies along the z-coordinate (the out-of-page coordinate in Fig. 2.1), and the incident field lies entirely in the x, y plane. With this geometry, there is no dependence of ϕ_D on the z-coordinate. We can introduce z-dependence by allowing the angle between the z-axis and the direction of the incident field to be arbitrary (oblique incidence) instead of being $\pi/2$. Calling this angle γ, we now have for the incident field

$$\phi_I(x,y,z) = e^{ik\cos\alpha\sin\gamma - iky\sin\alpha\sin\gamma + ikz\cos\gamma} \tag{6.1}$$

where setting $\gamma = \pi/2$ recovers our original incident field confined to the x, y plane. We obtain a three-dimensional solution (with the restriction that the edge discontinuity remain along the z-axis) from our two-dimensional solution by replacing k with $k\sin\gamma$ and multiplying by $e^{ik\cos\gamma}$ [73].

A related issue concerns the probability distribution for the ice floe leading and trailing edge *orientations* with respect to the acoustic propagation path. The analogous problem has been addressed for the scattering from lineal ice keels, where the classic Buffon needle problem [60] from probability theory was used to derive the orientation probability density function [34]. In our case the random variable corresponding to the orientation is the angle γ, and we note that the expected value of γ, when modeled by a Buffon needle process, is indeed $\pi/2$.

6.1.2 Finite extent L

The two-dimensional solution also assumes the diffracting edge is of infinite extent in the z-direction or perpendicular to the x, y plane. The diffracted field therefore takes on the appearance of a field radiated by an infinite line soure in the z-direction, with the general form

$$\phi_D(r,\theta) \sim F(\theta)\frac{e^{ikr}}{\sqrt{kr}}. \tag{6.2}$$

Recent work [67] on sound scattering by finite length cylinders, has shown that the solution for a finite length cylinder can be obtained from the infinite length counterpart through effectively integrating the latter over the length of the cylinder. Equation(6.2) is analogous to the scattered field for an infinite length cylinder, provided the field point does not lie in the transition region. An interesting approach would be to this method to our solution in order to examine the effects of finite extent L.

6.1.3 Further use of the locally reacting approximation

In Chapter 3 we studied the locally reacting approximation for the input impedance of an ice sheet, where

$$Z_{in} = -i\omega\rho_1 H \tag{6.3}$$

which we found to be a useful initial step towards the solution of the full elastic ice diffraction problem in Chapter 4. For low frequencies such that $fH \lesssim 50$ (where in this range we showed that the locally reacting approximation was quite accurate) it would be interesting to exploit this approximation further, by studying range-dependent ice thickness variation in which the ice impedance assumes the form

$$Z_{in}(x) = -i\omega\rho_1 H(x). \tag{6.4}$$

Appendix A

Asymptotic evaluation of integrals

Integrals of the form

$$\int_{\Gamma} Q(\beta)e^{ikr\cos(\beta-\theta)}d\beta \tag{A.1}$$

are evaluated asymptotically in this appendix. This integral represents a superposition of plane waves weighted by the angular spectral function $Q(\beta)$. The contour Γ is the same contour shown in Fig. 2.4. For $kr \gg 1$ there is exponential decay in the integrand for values of β away from the saddle point at $\beta = \theta$, and the contribution of Γ in the vicinity of $\beta = \theta$ constitutes the first order contribution to the integral.

The contour Γ is deformed into the steepest descent path (SDP) contour Γ_θ, and in the vicinity of $\beta = \theta$ we use the transformation

$$\cos(\beta - \theta) = 1 + i\tau^2 \tag{A.2}$$

changing Eq.(A.1) into

$$\sqrt{2}e^{ikr-i\frac{\pi}{4}}\int_{-\infty}^{\infty}\frac{Q(\beta)}{\sqrt{1+i\frac{\tau^2}{2}}}e^{-kr\tau^2}d\tau. \tag{A.3}$$

If the function $Q(\beta)$ is slowly varying in the region of the saddle point $\beta = \theta$ we can bring this factor outside the integral, giving

$$\sqrt{2}e^{ikr-i\frac{\pi}{4}}Q(\theta)\int_{-\infty}^{\infty}[1 - i\frac{\tau^2}{4} + \ldots]e^{-kr\tau^2}d\tau \tag{A.4}$$

where we have used a Taylor series to represent the square root factor. Term by term integration gives

$$(1-i)\sqrt{\pi}Q(\theta)e^{ikr}[\frac{1}{(kr)^{\frac{1}{2}}}-\frac{i}{8(kr)^{\frac{3}{2}}}+...] \tag{A.5}$$

Note that the next order term is 38 dB down from the leading order term at $kr = 10$.

Appendix B

Approximation of the Wiener-Hopf kernel and subsequent multiplicative decomposition for local reaction case

We can write the Wiener-Hopf kernel $K(q)$ as

$$K(q) = \sqrt{q^2 - k^2}[1 + \frac{\eta}{\sqrt{q^2 - k^2}}] \tag{B.1}$$

where the factor in brackets is $k(q)$ and is approximated as follows:

$$\hat{k}(q) = \frac{(\eta^2 + k^2 + q^2)}{\sqrt{q^2 - k^2}\sqrt{q^2 + Nk^2}} \cdot \frac{(q^2 - k^2 A_1^2)}{(q^2 - k^2 A_2^2)}. \tag{B.2}$$

The unknowns A_1^2 and A_2^2 are determined by matching the area and first three moments of the inverse Fourier transform of $k(q)$; these depend on the integer parameter $N = n^2$ which determines the relative height of the branch points of $\sqrt{q^2 + Nk^2}$ above and below the real q axis. To match the moments, one uses the moment generating relationship between transformed quantities, giving the matching equations

$$\frac{d^m \hat{k}(q)}{dq^m} = \frac{d^m k(q)}{dq^m} \tag{B.3}$$

which are evaluated at $q = 0$.

The result, with non-dimensional parameter λ defined here as η/k, is

$$A_1^2 = \frac{nA_2^2}{\lambda + i} \quad A_2^2 = \frac{\Lambda_1}{\Lambda_2} \tag{B.4}$$

where

$$\Lambda_1 = \lambda^3 \frac{2}{n} + \lambda^2 (\frac{2i}{n} - 2) + \lambda \frac{2}{n} + (\frac{2i}{n} - 2) \tag{B.5}$$

$$\Lambda_2 = \frac{-\lambda^2}{n^2} - i\lambda + (3 - \frac{1}{n^2}) \tag{B.6}$$

such that

$$\hat{K}(q) = \sqrt{q^2 - k^2}\ \hat{k}(q). \tag{B.7}$$

The four moment match ($m = 4$) gives a very accurate approximation with an error of a few percent in the homogeneous ($q < |k|$) region of the spectrum (Fig. B.1). For the inhomogeneous ($q > |k|$) region the approximation is less accurate; although we utilize only the homogeneous portion of the final plane wave spectrum in the inversion to the diffracted far field, and the necessary property of the ratio $K/\hat{K} \to 1$ as $q \to \infty$ is maintained.

The multiplicative decomposition of $\hat{K}(q)$ is defined as

$$\hat{K}(q) = \frac{\hat{K}_-(q)}{\hat{K}_+(q)}. \tag{B.8}$$

With this definition, zeroes and poles of $\hat{K}(q)$ in an upper (lower) half-plane are defined as '−' ('+') functions [59]. (The upper and lower half-planes are established by the branch cuts of $\sqrt{q^2 - k^2}$ as discussed in Chapter 2.) For example, two zeroes of the kernel originate from

$$q^2 + k^2 + \eta^2 = (q + i\sqrt{k^2 + \eta^2}) \cdot (q - i\sqrt{k^2 + \eta^2}). \tag{B.9}$$

The factor $(q + i\sqrt{k^2 + \eta^2})$ is a zero in the lower half-plane and is classified as a '+' function, and in the same manner $(q - i\sqrt{k^2 + \eta^2})$ is classified as a '−' function. The complete decompositon of Eq.(B.7) is

$$\hat{K}_-(q) = \frac{(q - i\sqrt{k^2 + \eta^2})}{\sqrt{q - ikn}} \cdot \frac{(q - kA_1)}{(q - kA_2)} \tag{B.10}$$

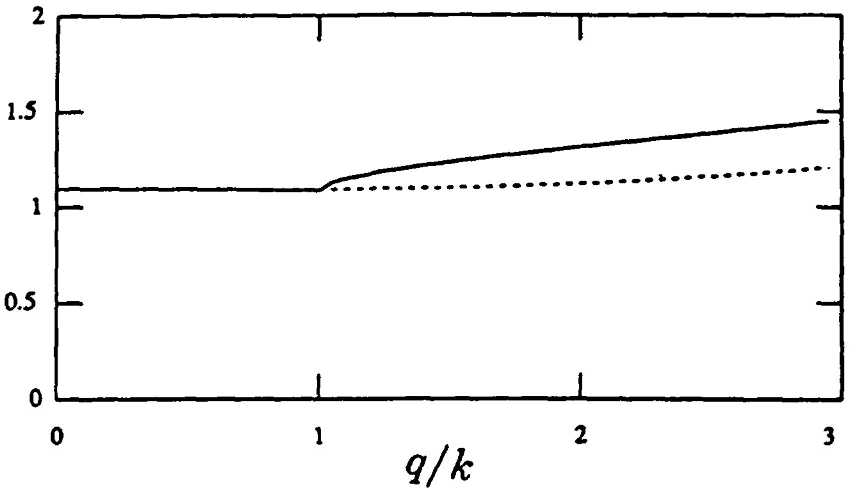

Figure B.1: Comparison of the modulus $K(q)$ (solid line) with $\hat{K}(q)$ (dashed line) for 30 Hz, $H = 1\text{m}$ and $\rho_1 = .92$.

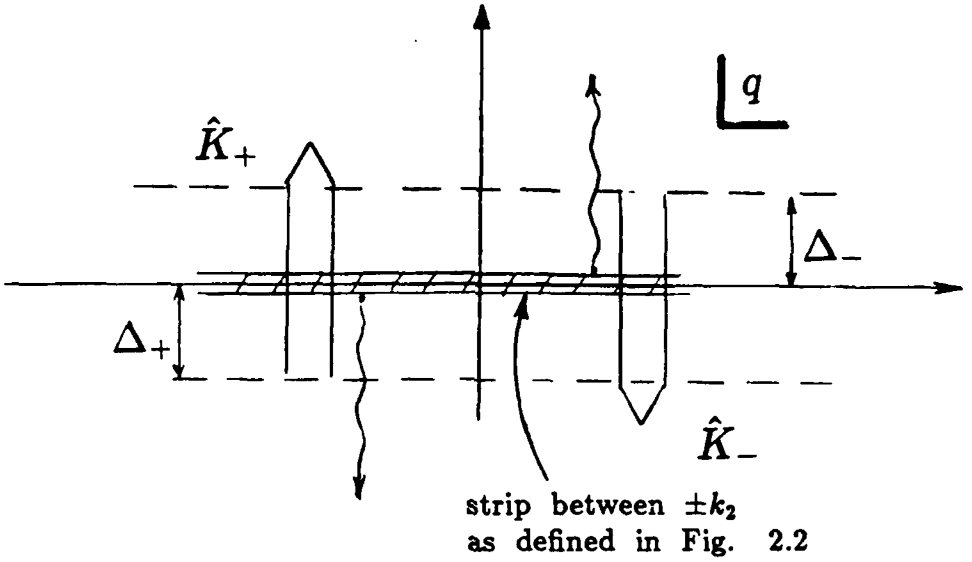

Figure B.2: Upper and lower half-planes of the approximate kernel as defined in the complex q-plane.

$$\hat{K}_+(q) = \frac{\sqrt{q + ikn}}{(q + i\sqrt{k^2 + \eta^2})} \cdot \frac{(q + kA_2)}{(q + kA_1)}.$$

The regions of analyticity for $\hat{K}_-$ and $\hat{K}_+$ are determined by

$$\Delta_- = k_1 Im(A_2) + k_2 Re(A_2) \quad \Delta_+ = k_1 Im(A_1) + k_2 Re(A_1) \tag{B.11}$$

such that $\hat{K}_-$ is analytic for $Im(q) < \Delta_-$ and $\hat{K}_+$ is analytic for $Im(q) > -\Delta_+$. (Note that k_2 is either a small positive constant or zero). These regions are shown in Fig. B.2.

The parameter N is a positive number, adjusted to optimize the phase coherence between $K(q)$ and $\hat{K}(q)$. Its upper bound is determined by the requirement

$$\Delta_+, \Delta_- > 0 \tag{B.12}$$

in order to maintain the '+' and '−' function definitions. For example, N is typically $O(10)$, establishing Δ_+ and Δ_- as $O(k)$.

Finally, a comparison of $\hat{K}_-(q)$ with one obtained via an asymptotic decompositon [22] for $\eta \rightarrow 0$ (which can be viewed as a perturbation from a perfectly rigid surface) show agreement within 1 percent for magnitude and phase. For this case we use $N = -1$ and $n = -i$ (consistent with the established branch cuts), which we find to more accurately approximate the kernel when $\eta \ll 1$. With the choice of either $N = -1$ or $N =$ a positive integer, the entire range of locally reacting boundary conditions from Neumann to Dirichlet is spanned.

Appendix C

Approximation of the Wiener-Hopf kernel and subsequent multiplicative decomposition for extended reaction case

In this Appendix we develop the approximate kernels used in the extended reaction case, which do not depend upon a small fluid loading parameter and therefore are valid in the fluid loading regime characteristic of sea ice and low-frequency acoustics. Three different approximations are developed here. Part I presents the details of the approximate kernel which represents an extension of the technique of matching moments as discussed in Appendix B. This kernel is $\hat{K}(q)$ and its decomposition into $\hat{K}_-/\hat{K}_+$ is the one employed in the diffracted field plane wave spectrum [Eq.(4.46)], and it has the necessary accuracy in the homogeneous region of the plane wave spectrum, along with accurately characterizing the pole at $q = k_f$. We also employ two additional kernels solely for use in the coefficient matrix [Eq.(4.53)] and right-side column vector [Eq.(4.54)]. These are referred to in this thesis as tagged kernels and details of their development are given in Part II of this Appendix. In

Part III we compare our results with an asymptotic result available in the literature.

Part I: matched moment kernel

As in Appendix B we write the kernel as

$$K(q) = \sqrt{q^2 - k^2}[\frac{\eta}{\sqrt{q^2 - k^2}} + 1 - \frac{q^4}{k_f^4}] \tag{C.1}$$

and focus on the bracketed term $k(q)$ which is approximated as follows

$$\hat{k}(q) = r_1^2 \frac{(\eta^2 + k^2 + q^2)}{\sqrt{q^2 - k^2}\sqrt{q^2 + Nk^2}} \cdot \frac{(q^2 - k^2 A_1^2)}{(q^2 - k^2 A_2^2)} \cdot (1 - \frac{q^4}{k_f^4}). \tag{C.2}$$

Apart from the parameter r_1, and $(1 - \frac{q^4}{k_f^4})$ which we will call the root factor, $\hat{k}(q)$ is the same as the one developed in Appendix B. We proceed to match the area plus first three moments of $k(q)$ in the manner of Appendix B and thereby determine the two unknowns A_1 and A_2. The result using the parameter λ equal to η/k is

$$A_1^2 = \frac{nA_2^2}{(\lambda + i)r_1}, \quad A_2^2 = \frac{\Lambda_1}{\Lambda_2} \tag{C.3}$$

where

$$\Lambda_1 = \lambda^3 r_1 \frac{2}{n} + \lambda^2 (r_1 \frac{2i}{n} - 2) + \lambda r_1 \frac{2}{n} + (r_1 \frac{2i}{n} - 2) \tag{C.4}$$

$$\Lambda_2 = \frac{-\lambda^2}{n^2} - i\lambda + (3 - \frac{1}{n^2}) \tag{C.5}$$

such that

$$\hat{K}(q) = \sqrt{q^2 - k^2} \;\; \hat{k}(q). \tag{C.6}$$

We insert a parameter $r_1 = (\bar{k}_f/k_f)^4$ to recover the correct asymptotic property

$$\lim_{q \to \infty} \frac{\hat{K}(q)}{K(q)} = 1. \tag{C.7}$$

The multiplicative decomposition of $\hat{K}(q)$ is defined as

$$\hat{K}(q) = \frac{\hat{K}_-(q)}{\hat{K}_+(q)} \tag{C.8}$$

which we write down in exactly the same manner as in Appendix B, with the additional decomposition of the root factor, giving

$$\hat{K}_-(q) = \frac{\sqrt{r_1}(q - i\sqrt{k^2 + \eta^2})}{\sqrt{q - ikn}} \cdot \frac{(q - kA_1)}{(q - kA_2)} \cdot (1 - \frac{q}{k_f}) \cdot (1 + \frac{iq}{k_f}) e^{i\frac{\pi}{4}} \tag{C.9}$$

$$\hat{K}_+(q) = \frac{\sqrt{q+ikn}}{\sqrt{r_1}(q+i\sqrt{k^2+\eta^2})} \cdot \frac{(q+kA_2)}{(q+kA_1)}[(1+\frac{q}{\bar{k}_f})\cdot(1-\frac{iq}{\bar{k}_f})]^{-1}e^{i\frac{\pi}{4}}.$$

Decomposition of the root factor is done by inspection, with one of the factorizations, $(1-\frac{q}{\bar{k}_f})$, having a zero at $q = \bar{k}_f$, for example. This zero is in the *upper half* of the complex q-plane because $\bar{k}_f$ may lie on the real q-axis, or just above it if we allow for damping of the coupled flexural wave; but it never lies below the real q-axis. Following our pole/zero allocation rules, this factorization is properly assigned to the '−' function classification, and since the zero at $q = \bar{k}_f$ becomes a pole in the diffracted field plane wave spectrum, the '−' function assignment correctly results in the pole being captured for $x > 0$ only.

Part II: tagged kernels

In this part we develop two additional approximate kernels, one which tags the value of the exact kernel at $q = \pm k_f$ (k_f-tagged), and the other which tags the value at $q = \pm ik_f$ (ik_f-tagged). Results from the tagged kernels are used in the coefficient matrix for recovering the constants e_0 and e_1. It is emphasized here that the tagged kernels represent an alternative approximation to the same exact kernel, and thus we could, in many cases, complete the solution using only one approximate kernel to represent all the critical regions in the complex q-plane. These regions are: the $q < k$ or homogeneous region, $q = \pm k_f, \pm ik_f$, and the $q = \bar{k}_f$ region where the kernel goes through a zero point. We are simply using the tagged kernels where we know they perform best at $q = \pm k_f, \pm ik_f$, a region the matched moment kernel is not specifically designed for.

The tagged kernels assume the same initial form as Eq.(C.2). Both versions of tagged kernels are given the same area or zeroth moment as the exact kernel; this puts

$$A_1^2 = \frac{nA_2^2}{(\lambda+i)r_1}. \tag{C.10}$$

We now find the other unknown A_2 by tagging the value of the exact kernel at a fixed point in the complex q-plane. The tag at $q = k_f$ (also $-k_f$) gives

$$\Lambda_1 = r_2(1-\Phi) \tag{C.11}$$

$$\Lambda_2 = \frac{n}{(\lambda+i)r_1} - \Phi \tag{C.12}$$

with

$$\Phi = \frac{\eta\sqrt{k^2N + k_f^2}}{(r_1 - 1)(k^2 + \eta^2 + k_f^2)} \tag{C.13}$$

and $r_2 = (k_f/k)^2$. The tag at $q = ik_f$ (also $-ik_f$) gives

$$\Lambda_1 = r_2(\Phi - 1) \tag{C.14}$$

$$\Lambda_2 = \frac{n}{(\lambda + i)r_1} - \Phi \tag{C.15}$$

with

$$\Phi = \frac{\eta\sqrt{k^2N - k_f^2}}{(r_1 - 1)(k^2 + \eta^2 - k_f^2)} \tag{C.16}$$

and we determine A_2^2 by the ratio Λ_1/Λ_2 as as in the matched moment kernel.

The three approximate kernels are shown in Fig. C.1 for the ice plate example presented in Chapter 4 (50 Hz, H=2 m). In this example $k_f = .419814$ and $\bar{k}_f = .509958$. Each kernel approximation will pass through a zero at $q = \bar{k}_f$ ($q/k \approx 2.35$ on the plots). Figure C.1(bottom) is the matched moment kernel and it tracks the homogeneous ($q/k < 1$) region of the exact kernel in both magnitude and phase with a maximum relative error of 3%. The maximum error occurs near the end of the homogeneous region and for the majority of this region the relative error is on the order of 1%. The exact behavior through the zero point is also completely reproduced in magnitude and phase.

We see, however, that the matched moment kernel is less accurate in the critical area at $q = k_f$ ($q/k \approx 1.94$ on the plots). Thus we resort to the k_f-tagged kernel in Fig C.1(middle). Here the magnitude and phase properties of the exact kernel at $q = k_f$ are precisely reproduced. The performance of the k_f-tagged kernel through the zero point is noteworthy. The k_f-tagged kernel will always track the slope of the exact kernel as it passes through the zero point, because the critical points in determining the slope, $q = k_f$ and $q = \bar{k}_f$, are precisely matched. For the ice plate examples studied in this thesis, either the matched moment kernel or k_f-tagged kernel is adequate for tracking the slope through the zero point region. But one may encounter cases, such as the low-frequency, heavy fluid loading comparison example presented below, where the k_f-tagged kernel clearly performs better. Finally we have the ik_f-tagged kernel in Fig. C.1(top) which at first glance appears to display none of the above properties we are looking for. But its sole purpose is to provide a good estimate *off* the real q-axis at $q = \pm ik_f$, for which it is precisely matched.

Part III: Comparison of the approximate kernel performance with available asymptotics

Let us compare the performance of our approximate kernels and subsequent decomposition, with an available asymptotic decomposition given in ref.[21]. Since we set up our problem and go about the kernel decomposition in a slightly different manner, this necessitates comparing a modification of our decomposition, $e^{-i\frac{\pi}{4}}k_f^2/\hat{K}_+$, to their asymptotic decomposition K_+^a. The asymptotic decomposition is valid only in the limit of low-frequency, heavy fluid loading. A typical example in this regime is a .25 m-thick steel plate immersed in water and ensonified at a frequency of 5 Hz.

Results of a comparison from this example are presented in Table C.1. The left side of the table shows results from our suitably modified approximate kernels (including the double-sided fluid loading) but denoted here as simply $\hat{K}_+$, the right side shows the asymptotic result K_+^a as derived from ref.[21]. The results represent the three critical regions in the complex q-plane. The matched moment kernel is used in the homogeneous region; the k_f-tagged kernel is used at $q = k_f$, and the $q = ik_f$-tagged kernel is used at $q = ik_f$. The k_f-tagged kernel is also used at $q = \bar{k}_f$ because it more accurately tracks the slope of the exact kernel in this low-frequency, heavy fluid loading example. The proper phase relation between the two sets of complex results is evident, with the maximum relative difference $(|\hat{K}_+|/|K_+^a|)$ being $\lesssim$ 5%. Finally, the equations in ref.[21] from which the asymptotic results were derived, arise from considerable manipulation of the small fluid loading parameter in order to come up with a usable expression. The small parameter in this case is M [Eq.(4.8)], and the expressions are presented in the form of a series expansion in M, with complicated coefficients which themselves are reported only to leading order. Considering this, a 5% relative difference appears quite justified.

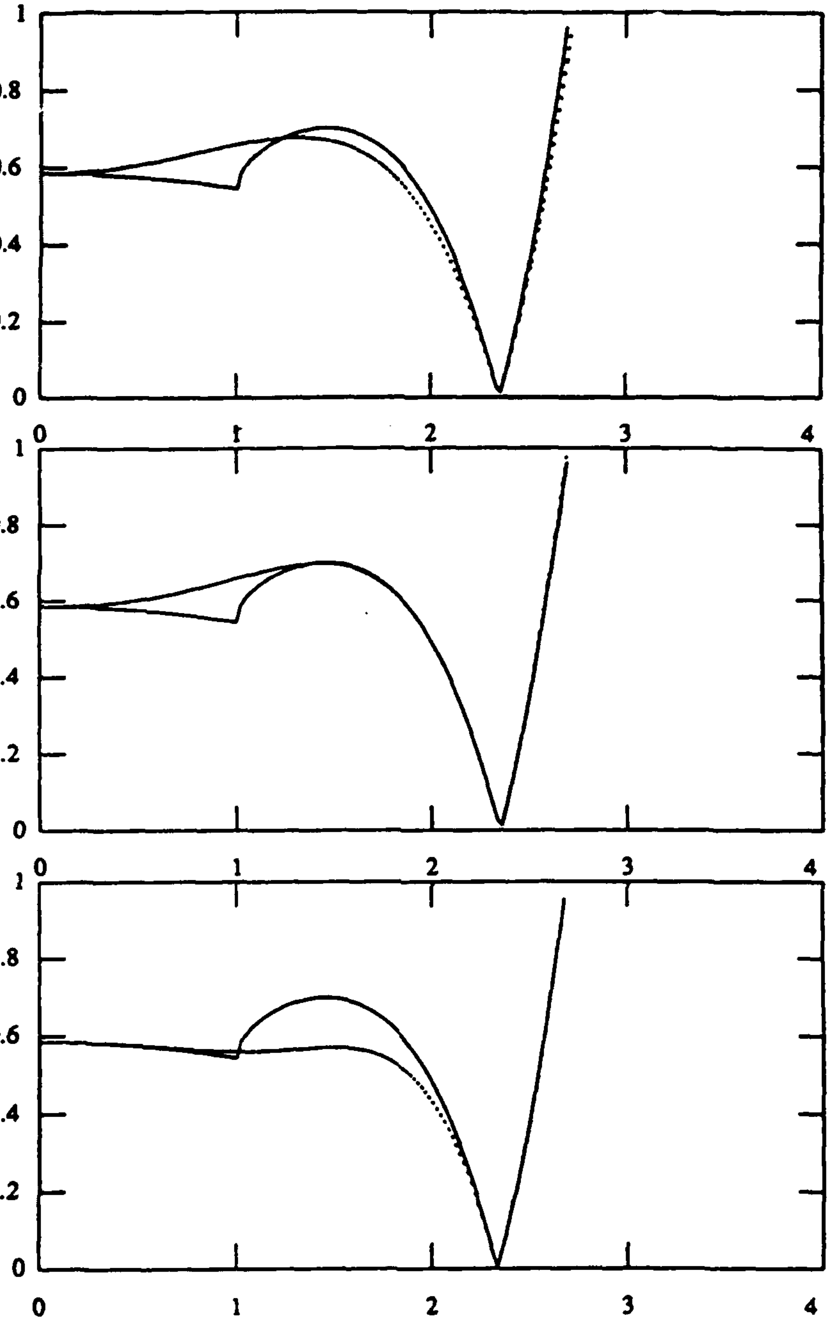

Figure C.1: Comparison of the modulus of extended reaction kernel $K(q)$ (solid line) with $\hat{K}(q)$ (dashed line). bottom: matched moment kernel, middle: k_f-tagged kernel, top: ik_f-tagged kernel. Normalized wavenumber (q/k) is used with $q/k < 1$ representing the homogeneous wavenumber spectrum.

region	$Re(\check{K}_+)$	$Im(\check{K}_+)$	$Re(\check{K}^a_+)$	$Im(\check{K}^a_+)$
$q = 0$	-.0016	-.0805	-.0006	-.0802
$q = .5k$	-.0047	-.0837	-.0032	-.0820
$q = .95k$	-.0083	-.0872	-.0063	-.0840
$q = k_f$	-.1699	-.1065	-.1499	-.1200
$q = ik_f$	.1480	-.1893	.1268	-.1856
$q = \bar{k}_f$	-.2767	-.0920	-.2603	-.0900

Table C.1: Comparison of the performance of the approximate kernels with an available asymptotic decomposition, in the three critical regions of the complex q-plane.

Bibliography

[1] *International Mathematical and Statistical Library, Ed. 8.* IMSL, Houstin, TX, 1980.

[2] *MATRIXX linear algebra program.* Integrated Sytems, Inc., Houstin, TX, 1984.

[3] M. Abramowitz and I. A. Stegun. *Handbook of Mathematical Functions.* U.S. Department of Commerce, 1964.

[4] B.B. Baker and E.T. Copson. *The Mathematical Theory of Huygens's Principle.* Clarendon Press, Oxford, 1949.

[5] J. Bazar and S.N. Karp. Propagation of plane electromagnetic waves past a shoreline. *J. Res. Natl. Bur. Std.*, D66:319 - 334, 1962.

[6] A.D. Bekifi and A.H. Barrett. *Electromagnetic Vibrations, Waves, and Radiation.* MIT Press, Cambridge, MA, 1977.

[7] C.M. Bender and S.A. Orszag. *Advanced Mathematical Methods for Scientists and Engineers.* McGraw-Hill, New York, 1978.

[8] L. M. Brekhovskikh. *Waves in Layered Media.* Academic, New York, 1960.

[9] D.G. Browning and R.H. Mellen. Attenuation of low-frequency sound in the sea: recent results. In *Progess in Underwater Acoustics*, International Congress on Acoustics, Toronto, Canada, July 1986.

[10] W.J. Campbell et. al. Variations of mesoscale and large-scale sea ice morphology in the 1984 Marginal Ice Zone Experiment as observed by microwave remote sensing. *J. Geophysical Res.*, 92 no.C7:6805 - 6823, 1987.

[11] P. A. Cannell. Acoustic edge scattering by a heavily loaded elastic half-plane. *Proc. R. Soc. Lond.*, A350:71 - 89, 1976.

[12] P. A. Cannell. Edge scattering of aerodynamic sound by a lightly loaded elastic half-plane. *Proc. R. Soc. Lond.*, A347:212 - 238, 1975.

[13] G. F. Carrier. Useful approximations in Wiener-Hopf problems. *J. Applied Phys.*, 30:1769 - 1774, 1959.

[14] G.F. Carrier, M. Krook, and C.E. Pearson. *Functions of a complex variable*. McGraw-Hill, New York, 1966.

[15] D.M.F Chapman. A simple estimate of propagation loss fluctuations due to modal interference. *J. Acoust. Soc. Am.*, 85:1097 - 1106, 1989.

[16] P.C. Clemmow. A method for the exact solution of a class of two-dimensional diffraction problems. *Proc. R. Soc. Lond.*, A205:286 - 308, 1951.

[17] P.C. Clemmow. *The Plane Wave Spectrum Representation of Electromagnetic Fields*. Pergamon Press, London, 1964.

[18] R.E. Collin. *Antenna Theory, Part II*. McGraw-Hill, New York, 1969.

[19] D.G. Crighton. Acoustics of a stiff locally reacting structure. *Proc. R. Soc. Lond.*, A397:99 - 119, 1985.

[20] D.G. Crighton. The free and forced waves on a fluid-loaded elastic plate. *J. Sound and Vib.*, 63:225 - 235, 1979.

[21] D.G. Crighton and D. Innes. The modes, resonances and forced response of elastic structures under heavy fluid loading. *Phil. Trans. R. Soc. Lond.*, A312:295 - 341, 1984.

[22] D.G. Crighton and F.G. Leppington. Scattering of aerodynamic noise by a semi-infinite compliant plate. *J. Fluid Mech.*, 43, 1970.

[23] P.H. Dahl, A.B. Baggeroer, P.N Mikhalevsky, and I. Dyer. Measurement of the temporal fluctuations of cw tones propagated in the marginal ice zone. *J. Acoust. Soc. Am.*, 83:2175 - 2179, 1988.

[24] M.E. Dougherty and R.A. Stephen. Geoacoustic scattering from seafloor features in the ROSE area. *J. Acoust. Soc. Am.*, 82:238 - 256, 1987.

[25] I. Dyer, A.B. Baggeroer, J.D. Zittel, and R.J. Williams. Acoustic backscattering from the basin and margins of the Arctic Ocean. *J. Geophysical Res.*, 87 no.C12:9477 - 9488, 1982.

[26] I. Dyer, P.H. Dahl, A.B. Baggeroer, and P.N Mikhalevsky. Ocean dynamics and acoustic fluctuations in the Fram Strait marginal ice zone. *Science*, 236:435 - 436, 1987.

[27] D. Feit. Pressure radiated by a point-excited plate. *J. Acoust. Soc. Am.*, 40:1489 -1494, 1966.

[28] J. R. Fricke. Numerical modeling of the scattered acoustic field from elastic ice. *J. Acoust. Soc. Am.*, Supp. 1, Vol 83, 1988.

[29] G.J. Fryer. Reflectivity of the ocean bottom at low frequency. *J. Acoust. Soc. Am.*, 63:35 - 42, 1978.

[30] G.H. Golub and C.F. Van Loan. *Matrix Computations.* The Johns Hopkins University Press, Baltimore, Md., 1983.

[31] A.J. Gow and W.B. Tucker III. Physical properties of sea ice discharged from the Fram Straight. *Science*, 236:436 - 439, 1987.

[32] K.F. Graff. *Wave Motion in Elastic Solids.* Ohio State U.P., Columbus, OH, 1975.

[33] R.D. Graves, A. Nagl, and H. Überall. Range-dependent normal modes in underwater sound propagation: application to the wedge-shaped ocean. *J. Acoust. Soc. Am.*, 58:1171 - 1177, 1975.

[34] R.R. Greene and P.A. Stokes. A model of acoustic backscatter from Arctic sea ice. *J. Acoust. Soc. Am.*, 78:1699 - 1701, 1985.

[35] A.E. Heins and H. Feshbach. On the coupling of two half planes. *J. Math. Physics (MIT)*, 26:143 - 155, 1947.

[36] F.B. Hildebrand. *Advanced Calculus for Applications*. Prentice-Hall, Englewood Cliffs, N.J., 1976.

[37] J. D. Jackson. *Classical Electrodynamics*. John Wiley & Sons, Inc., New York, 1962.

[38] G.L. James. *Geometrical Theory of Diffraction for Electromagnetic Waves*. Peter Peregrinus, London, 1986.

[39] F.B. Jensen and W.A. Kuperman. Sound propagation in a wedge-shaped ocean with a penetrable bottom. *J. Acoust. Soc. Am.*, 67:1564 - 1566, 1980.

[40] F.B. Jensen and M.G. Martinelli. *The SACLANTCEN Parabolic Equation Model (PAREQ)*. Technical Report, Saclant ASW Research Centre, December 1985.

[41] D.S. Jones. *Acoustic and Electromagnetic Waves*. Clarendon Press, Oxford, 1986.

[42] D.S. Jones. A simplifying technique in the solution of a class of diffraction problems. *Q. J. Math.*, 3:189 - 196, 1952.

[43] W.F. King III. The influence of fluid loading on acoustic propagation near surfaces. *J. Sound and Vib.*, 30:279 - 288, 1973.

[44] W.T. Koiter. Approximate solutions of Wiener-Hopf type integral equations with applications. *Koninkl. Ned. Akad. Wetenschap Proc.*, B57:558 - 564, 1954.

[45] W.A. Kuperman and H. Schmidt. Rough surface elastic wave scattering in a horizontally stratified ocean. *J. Acoust. Soc. Am.*, 79:1767 - 1777, 1986.

[46] G. L. Lamb. Diffraction of a plane sound wave by a semi-infinite thin elastic plate. *J. Acoust. Soc. Am.*, 31:929 - 935, 1959.

[47] A.J. Langley. Acoustic emission from the Arctic ice sheet. *J. Acoust. Soc. Am.*, 85:692 - 701, 1989.

[48] A.J. Langley. Exact and approximate theories for fluid-loaded,infinite, elastic plates. *J. Acoust. Soc. Am.*, 83:1366 – 1376, 1988.

[49] A.J. Langley. The sound fields of an infinite, fluid-loaded plate excited by a point force. *J. Acoust. Soc. Am.*, 83:1360 – 1365, 1988.

[50] A.K. Mann III, J. Tichy, and A.J. Romano. Instantaneous and time-averaged energy transfer in acoustic fields. *J. Acoust. Soc. Am.*, 82:17 – 29, 1987.

[51] S. Martin and P. Becker. High-frequency ice floe collisions in the Greenland Sea during the 1984 Marginal Ice Zone Experiment. *J. Geophysical Res.*, 92 no.C7:7071 – 7084, 1987.

[52] H. Medwin, M.J. Browne, K.R. Johnson, and P.L. Denny. Low-frequency backscatter from Arctic leads. *J. Acoust. Soc. Am.*, 83:1794 – 1803, 1988.

[53] H. Medwin, E. Childs, and G.M. Jebsen. Impulse studies of double diffraction: A discrete Huygens interpretation. *J. Acoust. Soc. Am.*, 72:1005 – 1013, 1982.

[54] R.H. Mellen, D.G. Browning, and J.M. Ross. Attenuation in randomly inhomogeneous sound channels. *J. Acoust. Soc. Am.*, 56:80 – 82, 1974.

[55] R.H. Mellen and P.M. Scheifele. *Arctic ice attenuation model study: final report.* Technical Report 8089, NUSC Technical Report, 1987.

[56] P.M. Mikhalevsky. *Data Summary MIZEX84 XBT and XSV Profiles.* Technical Report, MIT Department of Ocean Engineering, 1985.

[57] P.M. Morse. *Vibration and Sound.* McGraw-Hill, New York, 1948.

[58] P.M. Morse and K.U. Ingard. *Theoretical Acoustics.* McGraw-Hill, New York, 1964.

[59] B. Noble. *The Wiener-Hopf Technique.* Pergamon Press, London, 1958.

[60] A. Papoulis. *Probability, Random Variables and Stochastic Processes.* McGraw-Hill, New York, 1965.

[61] C.E. Pearson. *Handbook of Applied Mathematics.* Van Nostrand Reinhold, New York, 1974.

[62] A.D. Pierce. *ACOUSTICS An Introduction to its Physical Principles and Applications.* McGraw-Hill Book Co., New York, 1981.

[63] M.M. Schiffer. Partial differential equations of the elliptic type. In N. Aronszajn and C.B. Morrey, Jr., editors, *Lecture Series of the Symposium on Partial Differential Equations*, University of Kansas Press, Lawrence, Kansas, 1957.

[64] T. B. A. Senior. Diffraction by a semi-infinite metallic sheet. *Proc. R. Soc. Lond.*, 213:436 – 548, 1952.

[65] H.H. Shen, W.D. Hibler, and M. Leppäranta. The role of floe collisions in sea ice rheology. *J. Geophysical Res.*, 92 no.C7:7085 – 7096, 1987.

[66] P.W. Smith. Averaged sound transmission in range-dependent channels. *J. Acoust. Soc. Am.*, 55:1197 – 1204, 1974.

[67] T.K. Stanton. Sound scattering by cylinders of finite length I: Fluid cylinders. *J. Acoust. Soc. Am.*, 83:55 – 63, 1988.

[68] P.J. Stein. *Acoustic monopole in a floating ice plate.* PhD thesis, Massachusetts Institute of Technology, Feb. 1986.

[69] M. Townsend-Manning and I. Dyer. Acoustic events radiated by Arctic ice. *submitted to J. Acoust. Soc. Am.*, 1988.

[70] H. Überall. Surface waves in acoustics. In W.P. Mason and R.N. Thurston, editors, *Physical Acoustics Vol. 10*, Academic, New York, 1973.

[71] J. L. Uretsky. The scattering of plane waves from periodic surfaces. *Annals of Physics*, 33:400 – 427, 1965.

[72] P.J. Vidmar and T.L. Forman. A plane-wave reflection loss model including sediment rigidity. *J. Acoust. Soc. Am.*, 66:1830 – 1835, 1979.

[73] L.A. Weinstein. *The theory of diffraction and the factorization method.* The Golem Press, Boulder, Co., 1969.

DOCUMENT LIBRARY

July 5, 1989

Distribution List for Technical Report Exchange

Attn: Stella Sanchez-Wade
Documents Section
Scripps Institution of Oceanography
Library, Mail Code C-075C
La Jolla, CA 92093

Hancock Library of Biology &
Oceanography
Alan Hancock Laboratory
University of Southern California
University Park
Los Angeles, CA 90089-0371

Gifts & Exchanges
Library
Bedford Institute of Oceanography
P.O. Box 1006
Dartmouth, NS, B2Y 4A2, CANADA

Office of the International
Ice Patrol
c/o Coast Guard R & D Center
Avery Point
Groton, CT 06340

Library
Physical Oceanographic Laboratory
Nova University
8000 N. Ocean Drive
Dania, FL 33304

NOAA/NESDIS Miami Library Center
4301 Rickenbacker Causeway
Miami, FL 33149

Library
Skidaway Institute of Oceanography
P.O. Box 13687
Savannah, GA 31416

Institute of Geophysics
University of Hawaii
Library Room 252
2525 Correa Road
Honolulu, HI 96822

Library
Chesapeake Bay Institute
4800 Atwell Road
Shady Side, MD 20876

MIT Libraries
Serial Journal Room 14E-210
Cambridge, MA 02139

Director, Ralph M. Parsons Laboratory
Room 48-311
MIT
Cambridge, MA 02139

Marine Resources Information Center
Building E38-320
MIT
Cambridge, MA 02139

Library
Lamont-Doherty Geological
Observatory
Colombia University
Palisades, NY 10964

Library
Serials Department
Oregon State University
Corvallis, OR 97331

Pell Marine Science Library
University of Rhode Island
Narragansett Bay Campus
Narragansett, RI 02882

Working Collection
Texas A&M University
Dept. of Oceanography
College Station, TX 77843

Library
Virginia Institute of Marine Science
Gloucester Point, VA 23062

Fisheries-Oceanography Library
151 Oceanography Teaching Bldg.
University of Washington
Seattle, WA 98195

Library
R.S.M.A.S.
University of Miami
4600 Rickenbacker Causeway
Miami, FL 33149

Maury Oceanographic Library
Naval Oceanographic Office
Stennis Space Center
NSTL, MS 39522-5001

Marine Sciences Collection
Mayaguez Campus Library
University of Puerto Rico
Mayagues, Puerto Rico 00708

50272-101

REPORT DOCUMENTATION PAGE	**1. REPORT NO.** WHOI-89-28	**2.**	**3. Recipient's Accession No.**

4. Title and Subtitle

Acoustic Diffraction from a Semi-Infinite Elastic Plate under Arbitrary Fluid Loading with Application to Scattering from Arctic Ice Leads

5. Report Date
August 1989

6.

7. Author(s)
Peter Hans Dahl

8. Performing Organization Rept. No.
WHOI-89-28

9. Performing Organization Name and Address

The Woods Hole Oceanographic Institution
Woods Hole, Massachusetts 02543, and
The Massachusetts Institute of Technology
Cambridge, Massachusetts 02139

10. Project/Task/Work Unit No.

11. Contract(C) or Grant(G) No.
(C)
(G) N00014-87-K-0017

12. Sponsoring Organization Name and Address
The Office of Naval Research

13. Type of Report & Period Covered
Ph.D. Thesis

14.

15. Supplementary Notes

This thesis should be cited as: Peter Hans Dahl, 1989. Acoustic Diffraction from a Semi-Infinite Elastic Plate under Arbitrary Fluid Loading with Application to Scattering from Arctic Ice Leads. Ph.D. Thesis, MIT/WHOI, WHOI-89-28.

16. Abstract (Limit: 200 words)

The problem of a low-frequency acoustic plane wave incident upon a free surface coupled to a semi-infinite elastic plate surface, is solved using an analytic approach based on the Wiener-Hopf method. By low-frequency it is meant that the elastic properties of the plate are adequately described by the thin plate equation ($kH \lesssim 1$). The diffraction problem relates to issues in long range sound propagation through partially ice-covered Arctic waters. This work focusses on ice as the material for the elastic plate surface, and, though the solution methods presented here have applicability to general edge diffraction problems, the results and conclusions are directed toward the ice lead diffraction process. An approximation to the exact kernel of the Wiener-Hopf functional equation is used, which is valid in the fluid loading regime pertaining to sea ice and low-frequency acoustics. The far field diffracted pressure is found, and the functional dependence of Π_D (total diffracted power terms of k (wavenumber), H (ice thickness), α (grazing angle) and the combined elastic properties of the ice sheet and ambient medium is determined. A means to convert Π_D into an estimate of dB loss per bounce is developed using ray theoretical methods, in order to demonstrate a mechanism for acoustic propagation loss attributed directly to ice lead diffraction effects. Data from the 1984 MIZEX (Marginal Ice Zone Experiments) narrow-band acoustic transmission experiments are presented and discussed in this context.

17. Document Analysis a. Descriptors

1. acoustic diffraction
2. ice leads
3. Wiener-Hopf method

b. Identifiers/Open-Ended Terms

c. COSATI Field/Group

18. Availability Statement Approved for publication; distribution unlimited.	**19. Security Class (This Report)** UNCLASSIFIED	**21. No. of Pages** 156
	20. Security Class (This Page)	**22. Price**

(See ANSI-Z39.18) *See Instructions on Reverse* OPTIONAL FORM 272 (4-77)
(Formerly NTIS-35)
Department of Commerce